INVESTIGATING THE STRENGTH AND FAILURE MECHANISM OF HIGHLY INTERLOCKED JOINTED PILLARS USING 2D CONTINUUM MODELS

by

Yalin Li

Submitted in partial fulfilment of the requirements

for the degree of Master of Applied Science

at

Dalhousie University

Halifax, Nova Scotia

March 2021

TABLE OF CONTENTS

LIST OF TABLES

LIST OF FIGURES

ABSTRACT

Pillars are commonly used in underground mines to maintain the stability and integrity of the openings. An optimum design of mine pillars dictates that the pillars should be as small as possible and meet the load-bearing requirements. Therefore, a proper estimation of the rock mass strength is of paramount importance for a reliable design of mine pillars. It is known that the Hoek-Brown failure criterion, with its strength parameters obtained based on the Geological Strength Index, tends to underestimate the confined strength of well interlocked jointed hard rock masses. Therefore, pillar designs based on this approach could lead to oversized pillars due to underestimated strength of the pillar core. The central objective of this research is to better understand the strength and failure mechanisms of highly interlocked jointed pillars. For this purpose, a grain-based model is developed using the continuum numerical program RS2 to reproduce the laboratory behavior of intact and heat-treated Wombeyan marble. The heat-treated Wombeyan marble is considered to serve as an analogue for a highly interlocked jointed rock mass. An iterative calibration procedure is utilized to match the macro-properties of RS2-GBM to those of marble. It is found that the calibrated RS2-GBM captures some of the most important characteristics of brittle rocks, including the non-linear strength envelope and the change in the failure mode with increasing confinement. Next, the calibrated RS2-GBM of granulated marble is upscaled to simulate jointed pillars of various width-to-height ratios. The results of numerical simulations inferred that the slope of the pillar stability curve obtained from this approach is comparatively steeper than those of existing continuum and discontinuum models of jointed pillars. This is attributed to the high degree of block interlock leading to higher rock mass strength at the pillar core. It is demonstrated that this modeling approach provides more realistic results in terms of pillar failure processes compared to other continuum models, in which the rock mass is simulated as a homogeneous medium. The advantage of the continuum over the discontinuum GBM is its shorter computation time. Therefore, the proposed modeling approach can be used as a practical tool for stability analysis and design of mine pillars in jointed rock masses.

LIST OF ABBREVIATIONS AND SYMBOLS USED

1D	One-dimensional
2D	Two-dimensional
3D	Three-dimensional
BEM	Boundary Element Method
c_{bp}	Grain boundary peak cohesion
c_{br}	Grain boundary residual cohesion
CD	Crack Damage
c_{gp}	Grain peak cohesion
c_{gr}	Grain residual cohesion
CI	Crack Initiation
CWFS	Cohesion Weakening-Frictional Strengthening
D	Disturbance factor
DDM	Discontinuity Displacement Method
DEM	Discrete Element Method
DFN	Discrete Fracture Network
e	Extraction ratio
E	Young's modulus
E_g	Young's modulus of grain
FDEM	Hybrid Finite-Discrete Element Method
FDM	Finite Difference Method
FEM	Finite Element Method
FOS	Factor of Safety
GBM	Grain-Based Model
GSI	Geological Strength Index
GSI'	Modified Geological Strength Index
GSR	Geological Structure Rating
H	Pillar height
k	In-situ stress ratio
k_n	Grain boundary normal stiffness
k_s	Grain boundary shear stiffness

L	Pillar length
P_{21}	Fracture intensity
PSC	Pillar Stability Curve
PSR	Pillar Stress Rating
R_G	Model geometry scaling ratio
R_J	Joint stiffness ratio
SL	Spalling Limit
SRM	Synthetic Rock Mass
UCS	Unconfined Compressive Strength
v_g	Grain Poisson's ratio
W	Pillar width
W/H	Width-to-height ratio
ε	Axial strain
ε_p	Plastic strain
σ_1	Major principal stress/ intact or rock mass strength
σ_3	Minor principal stress/confining pressure
σ_a	Axial stress acting normal to the mid-height centerline of the pillar
σ_{ci}	Uniaxial compressive strength
σ_n	Normal stress
σ_{rm}	Unconfined rock mass strength
σ_{tbp}	Grain boundary peak tensile strength
σ_{tbr}	Grain boundary residual tensile strength
σ_{tgp}	Grain peak tensile strength
σ_{tgr}	Grain residual tensile strength
σ_{yy}	Vertical stress
τ	Shear strength
φ_{bp}	Grain boundary peak friction angle
φ_{br}	Grain boundary residual friction angle
φ_{gp}	Grain peak friction angle
φ_{gr}	Grain residual friction angle

ACKNOWLEDGEMENTS

I would like to express great appreciation to Prof. Navid Bahrani, my supervisor and mentor, who continuously provided guidance to improve my writing and modeling skills throughout the duration of my studies in the graduate program. I would have never travelled down the academic road without his encouragement. This thesis and the paper would not have been completed without his help.

I would also like to thank my internal committee member Prof. Steve Zou and my external examiner Prof. Ming Cai for reviewing my thesis and attending my defence.

I also want to address my love and thanks to my parents, Guoxiong Li and Chun Chang, and my fiancé, Hui Tu, who have always provided supports throughout the duration of my studies in Canada.

Thanks are extended to Brock Jeans, Farzaneh Hamedi Azad, and Soheil Sanipour, who helped me get through the global pandemic in 2020.

Finally, my thanks to the following organizations for their financial support which made this research possible: Natural Sciences and Engineering Research Council of Canada (NSERC) and Dalhousie University.

CHAPTER 1 INTRODUCTION

1.1. OVERVIEW

A pillar is a column of in situ rock left between two or more underground openings. Pillars are used in different underground mining methods as a natural support to maintain the local stability and integrity of the openings (Figure 1-1). The objective of underground mine design is to maximize ore extraction and concurrently maintain a safe working environment for the mining personnel and equipment. In some underground mining methods, pillars are left within the orebody (e.g., room-and-pillar). Hence, an optimum design of mine pillars dictates that the pillars should be as small as possible and meet the load-bearing requirements.

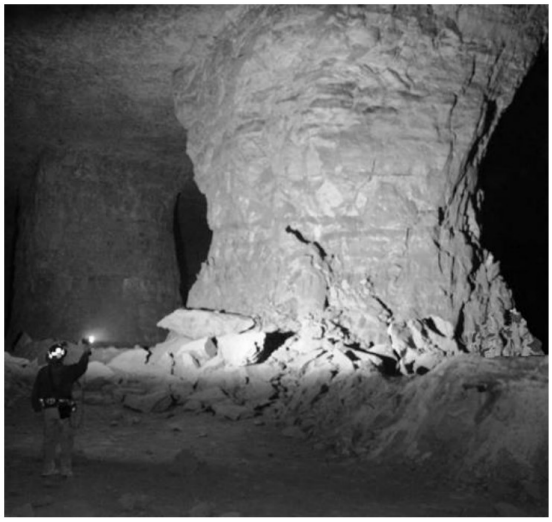

Figure 1-1: A pillar in a stone mine in Southern Appalachian area, USA (Esterhuizen et al., 2006).

The most common method for pillar design is premised on the observation of full-scale pillar performance. Several empirical pillar strength formulae have been developed for both coal (e.g., Salamon & Munro, 1967; Hustrulid, 1976) and hard rock pillars (e.g., Hedley & Grant, 1972; Von Kimmelmann et al., 1984; Krauland & Soder, 1987; Potvin et al., 1990; Lunder & Pakalnis, 1997). These formulae provide a relationship between the pillar stress to the intact rock strength ratio and the pillar width-to-height (W/H) ratio. The empirical approaches have been widely used over the past few decades to design pillars of various W/H ratios, typically ranging between 0.5 and 2.5.

In recent years, with an increase in computational power, numerical modeling has emerged as a powerful tool for conducting routine stability analysis and designing mine pillars. Estimating the rock mass strength is the first step in the numerical simulation of mine pillars. Different failure criteria, such as the linear Mohr-Coulomb and the non-linear Hoek-Brown, have been used in numerical programs based on continuum methods to investigate the effects of rock mass condition, in-situ stress magnitude, and pillar geometry on pillar strength and stability (e.g., Martin & Maybee, 2000; Mortazavi et al., 2009; Kaiser et al., 2011; Rafiei Renani & Martin, 2018; Sinha & Walton, 2018). Discontinuum numerical methods are mostly used to simulate the failure process of hard rock pillars, including fracture initiation and propagation leading to spalling and slabbing of the pillar walls, and shear failure at the pillar core (e.g., Elmo & Stead, 2010; Li et al., 2019).

It is notable that both continuum and discontinuum numerical methods require an estimate of the rock mass strength over a wide range of confinement. Underestimating the rock mass strength may lead to over-designed pillars, which could result in ore loss during the mining operation. Overestimating the rock mass strength may result in under-designed pillars creating an unsafe environment for mine personnel and equipment. Hence, it is crucial to properly estimate the rock mass strength in order to develop representative rock mass models for an optimum pillar design. This thesis focuses on the strength and failure mechanisms of pillars in jointed hard rock masses.

1.2. PROBLEM STATEMENT

The pillar strength is known to be a function of the pillar W/H ratio. Hoek (1983) discussed the influence of pillar W/H ratio on the confinement and pillar strength, as illustrated in Figure 1-2. This figure schematically depicts that there is little or no confining pressure (σ_3) in slender pillars (i.e., W/H < 0.7). Therefore, the pillar strength is close to the unconfined rock mass strength (σ_{cm}). For wider pillars, especially those with W/H ratios greater than 4, the confining pressure at the pillar core can be as high as 55% of the maximum principal stress (σ_1). Therefore, it is crucial to make a proper estimation of the confined strength of jointed rock masses in pillar design.

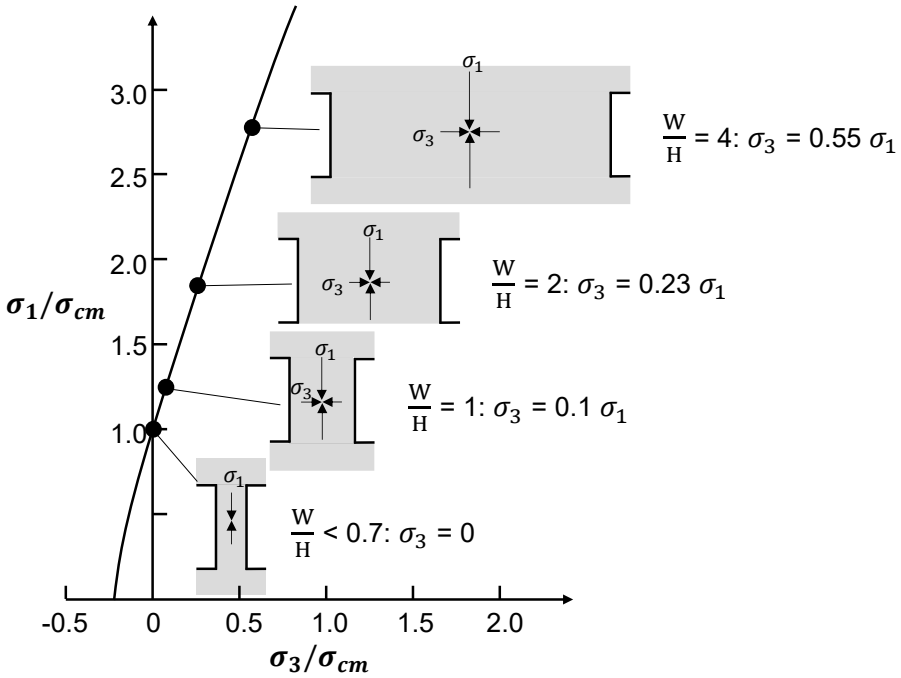

Figure 1-2: Influence of pillar W/H ratio on confining stress and strength of pillars (after Hoek, 1983).

The Hoek-Brown failure criterion (Hoek & Brown, 1980, 1997, 2019; Hoek et al., 2002) is widely used to estimate the strength and deformation properties of jointed rock masses. In the generalized form of the Hoek-Brown failure criterion, the rock mass strength (σ_1) is a function of confinement (σ_3) according to the following equation:

$$\sigma_1 = \sigma_3 + \sigma_{ci}\left(m_b\left(\frac{\sigma_3}{\sigma_{ci}}\right) + s\right)^a \qquad \textbf{Equation 1-1}$$

In this equation, the constant m_b denotes a reduced value of intact rock parameter m_i, while a and s are constants for the rock mass. The values of m_i and σ_{ci} are obtained from the statistical fit to the results of laboratory triaxial tests on intact rock specimens with confining pressures ranging from 0 to 50% of the Unconfined Compressive Strength (UCS; Hoek & Brown, 1997). In the original version of the Hoek-Brown failure criterion (Hoek & Brown, 1980), m_b/m_i and s are functions of the Rock Mass Rating (RMR; Bieniawski, 1973) and the Tunnelling Quality Index (Q; Barton et al., 1974). Subsequently, the Hoek-Brown failure criterion was updated by Hoek and Brown (1997) and Hoek et al. (2002). In both versions, the strength of a jointed rock mass is estimated by degrading the strength of

an intact rock to that of the rock mass using the Geological Strength Index (GSI) and the Disturbance factor (D).

The rock mass characterization system GSI was developed by Hoek (1994) and Hoek et al. (1995) in order to link the failure criterion to engineering geology observations in the field. Figure 1-3 presents the GSI chart by Hoek and Brown (2019). The GSI chart is used to define the quality of a jointed rock mass based on the degree of interlock and the surface condition of discontinuities. The degree of interlock is defined as the kinematic freedom of individual rock blocks to rotate and slide along the block forming joints (Hoek et al., 1995; Bahrani and Kaiser, 2020). D refers to the degree of the disturbance in the vicinity of the excavation walls caused by blasting (Hoek & Brown, 2019).

The Hoek-Brown strength parameters (m_b, s, and a) in Equation 1-1 are functions of GSI and D and can be determined using the following equations:

$$m_b = m_i \exp\left((GSI - 100)/(28 - 14D)\right) \quad \textbf{Equation 1-2}$$

$$s = \exp\left((GSI - 100)/(9 - 3D)\right) \quad \textbf{Equation 1-3}$$

$$a = (1/2) + (1/6)\left(\exp(-GSI/15) - \exp(-20/3)\right) \quad \textbf{Equation 1-4}$$

Recently, Hoek and Brown (2019) discussed the applicability of the Hoek-Brown failure criterion and the GSI system for estimating the strength of jointed rock masses:

"The GSI system assumes that, because the rock mass is made up of a sufficiently large number of joint sets and randomly oriented discontinuities, it can be treated as a homogeneous and isotropic mass of interlocking blocks. Failure of this rock mass is the result of sliding along discontinuities or rotation of blocks, with relatively little failure of the intact rock blocks."

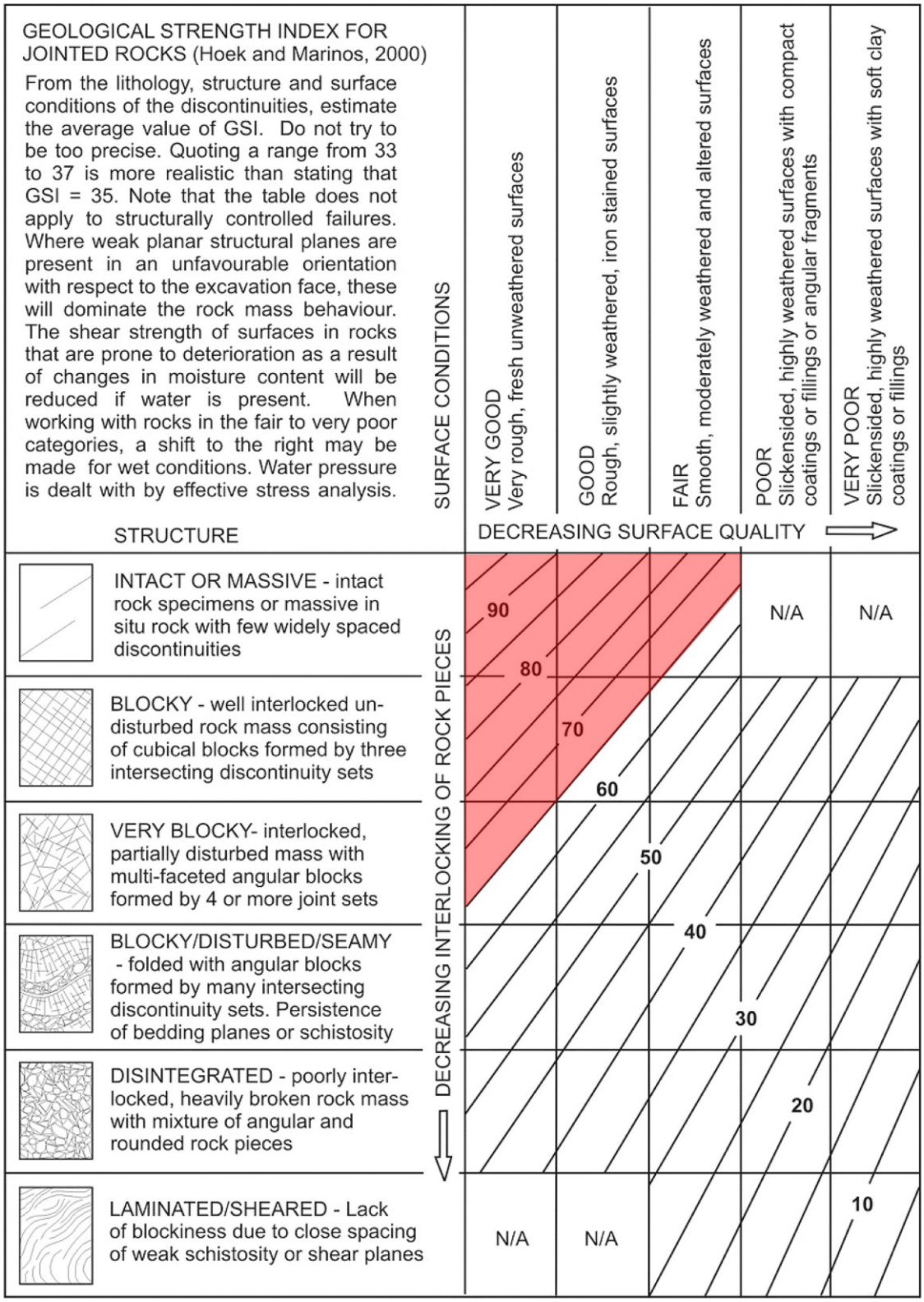

Figure 1-3: Geological Strength Index (GSI) chart (after Hoek & Brown, 2019). Rock masses with GSI values greater than 65 shaded in red.

Hoek and Brown (2019) further postulated that this approach underestimates the strength for massive to moderately jointed rock masses represented by GSI values greater than 65 (area highlighted in red in Figure 1-3); therefore, Equation 1-2 to Equation 1-4 need modifications for such rock masses. In the GSI system, such rock masses are generally described as massive (GSI = 85-100), well interlocked (GSI = 75 - 85), and interlocked (GSI = 65 - 75) rock masses. In the Canadian Shield, rock masses at great depths (i.e., > 1.5 km) are found to be massive to moderately jointed (i.e., GSI > 65), which is why it is recommended that the Hoek-Brown failure criterion should not be used to estimate their strengths, especially at high confinement (Kaiser et al., 2011).

Kaiser et al. (2011), Valley et al. (2011), Bahrani and Kaiser (2013), Bahrani et al. (2014), and Bewick et al. (2019) hypothesized that the Hoek-Brown failure criterion underestimates the confined strength of highly interlocked jointed rock masses (i.e., GSI > 65). In such rock masses, the rock blocks are hard and brittle, and the joints are rough and non-persistent. Due to difficulties in conducting laboratory tests on large scale rock masses, the behavior of highly interlocked jointed rock masses under confined conditions has been studied in the laboratory on physical models and analogues for such rock masses (Gerogiannopoulos, 1976; Gerogiannopoulos & Brown, 1978; Rosengren & Jaeger, 1968).

Gerogiannopoulos (1976), Gerogiannopoulos and Brown (1978) and Rosengren and Jaeger (1968) studied the laboratory behavior of intact and heat-treated Wombeyan marble under both unconfined and confined compressions. The term ‘granulated’ refers to heat-treated marble specimens. The strength of granulated marble was found to increase rapidly with an increase in confining pressure, gradually approaching its intact strength. This results in a highly non-linear strength envelope caused by the high degree of interlock between the calcite grains. Rosengren and Jaeger (1968) suggested that the granulated Wombeyan marble can be treated as a model for a randomly jointed rock mass, while Bahrani and Kaiser (2013) and Bahrani et al. (2014) discussed that it can be served as an analogue for a highly interlocked jointed rock mass. In this rock mass analogue, the calcite grains are analogues for intact rock blocks, and grain boundaries are analogues for joints.

Bahrani and Kaiser (2020) investigated the influence of the degree of interlock between rock blocks on the strength of jointed rock masses at different levels of confinement. According to them, the main factors contributing to the degree of block interlock in a jointed rock mass include block shape, block size, joint orientation, joint surface condition (i.e., roughness), joint persistence, and block strength. Figure 1-4 demonstrates how the level of non-linearity of the strength envelope decreases with a decline in the degree of interlock. In other words, the higher the degree of interlock, the higher the curvature of the strength envelope. Bahrani & Kaiser (2020) also concluded that: 1) the confined strength of non-persistently jointed and blocky hard rock masses (i.e., GSI > 65) is likely to be higher than that estimated by the GSI strength equations; and 2) the Hoek-Brown failure criterion may be used to estimate the confined strength of well interlocked, persistently jointed rock masses comprising hard rock blocks, only if the joints are smooth and non-dilatant.

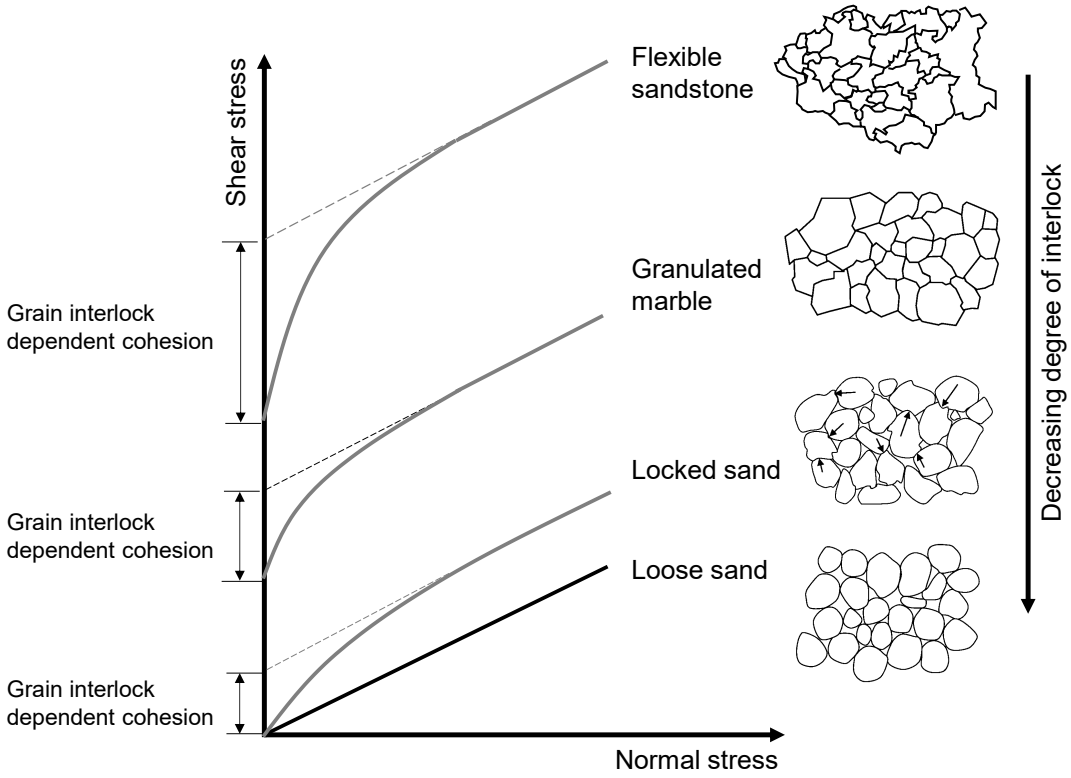

Figure 1-4: Schematic failure envelopes and fabric of granular assemblies for flexible sandstone, granulated marble, locked sand and loose sand (Bahrani & Kaiser, 2020).

In order to estimate the confined strength of highly interlocked jointed rock masses, Bahrani et al. (2014) simulated the laboratory behavior of granulated Wombeyan marble using *PFC* (by Itasca), which is a discontinuum program based on the Distinct Element Method (DEM). More recently, Bahrani and Kaiser (2020) used the calibrated *PFC* model of granulated marble to investigate the applicability of the Hoek-Brown failure criterion for estimating the confined strength of highly interlocked jointed rock masses. For this purpose, they back analyzed the strength of calcite grains (intact rock analogue) from their calibrated *PFC* model, and then used the Hoek-Brown failure criterion with a GSI value of 100 to determine its strength envelope. Thereafter, they reduced the GSI value to 67 to match the UCS of granulated marble (i.e., rock mass analogue), as shown in Figure 1-5. Through this exercise, they concluded that the GSI approach underestimates the confined strength of granulated marble (Figure 1-5), and in effect, the confined strength of highly interlocked jointed rock masses.

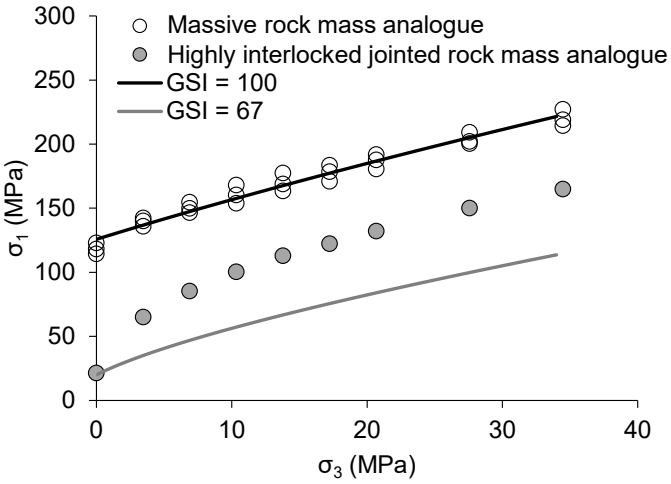

Figure 1-5: Comparison of strength data and Hoek-Brown envelopes of the model of calcite grain (intact rock analogue) and granulated Wombeyan marble (rock mass analogue) by Bahrani and Kaiser (2020).

Columnar basalt is an example of a highly interlocked jointed rock mass. Figure 1-6 demonstrates how the granular structure of Wombeyan marble (Figure 1-6a) is comparable to the structure of a columnar basaltic rock mass (Figure 1-6b). According to Bahrani and Kaiser (2020), the columnar basalt represents an extreme case of a jointed rock mass in terms of the degree of block interlock. As shown in Figure 1-6b, the medium in this rock mass is divided into several columns that are typically hexagonal with side lengths in the

order of a few tens of centimeters. The columns can slide along their long axis; however, in the direction perpendicular to their long axis, they cannot rotate or slide without disrupting the rock mass fabric or breaking through the intact rock blocks due to the high degree of interlock (Bahrani & Kaiser, 2020).

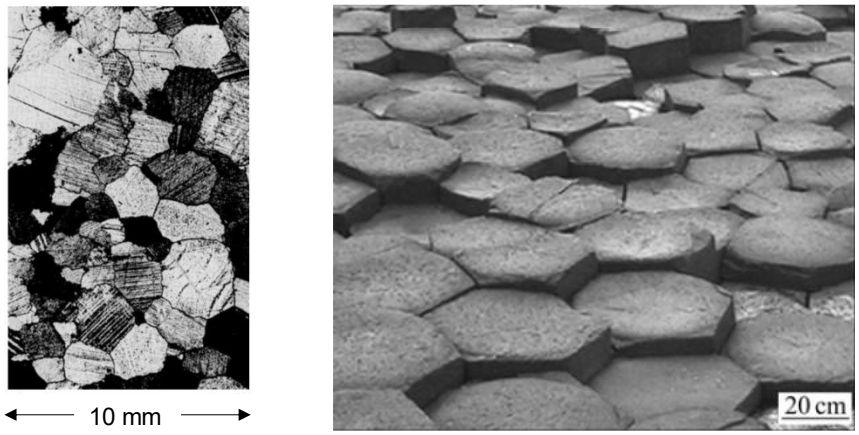

Figure 1-6: a) Grain geometry of Wombeyan marble under microscope (Rosengren & Jaeger, 1968) compared to: b) the structure of columnar basaltic rock mass (Di et al., 2011).

According to Bahrani et al. (2014) and Bahrani and Kaiser (2020), the dilation caused by the geometric incompatibility between the rock blocks in a highly interlocked jointed rock mass results in an initially steep strength envelope at low confinement, which is not captured by the conventional Hoek-Brown failure criterion. For this reason, the pillar design in highly interlocked jointed rock masses using the conventional Hoek-Brown criterion could lead to overdesigned pillars due to the underestimated rock mass strength. This, in turn, could potentially cause economic loss due to lower ore extraction. For this reason, Bahrani et al., (2014) and Bahrani and Kaiser (2020) emphasized on the need for a revised criterion for estimating the confined strength of highly interlocked, non-persistently jointed rock masses. In this context, the present thesis aims at estimating the strength of pillars in such rock masses and investigating their failure mechanisms as a function pillar W/H ratio using an advanced two-dimensional (2D) numerical modeling method.

1.3. OBJECTIVE AND APPROACH

The central objective of this research is to better understand the strength and failure mechanisms of highly interlocked jointed pillars. Toward that end, the laboratory behavior of Wombeyan marble is simulated using the continuum numerical method, based on the methodology proposed by Bahrani (2015). The calibrated models of granulated marble, which serves as an analogue for a highly interlocked jointed rock mass, are then used to simulate highly interlocked jointed pillars. The general approach for this research includes:

- Developing a continuum grain-based model to replicate the laboratory behavior of intact and heat-treated (granulated) Wombeyan marble using the numerical program *RS2* (Rocscience, 2019);

- Upscaling the calibrated grain-based model of granulated Wombeyan marble to simulate highly interlocked jointed pillars with different W/H ratios and to investigate their strength and failure mechanisms; and

- Comparing the numerically estimated pillar stability curves with those of jointed pillar strength formulas obtained from continuum and discontinuum models.

1.4. THESIS OUTLINE

The findings of this research are presented in five chapters:

Chapter 1 introduces the motivation, objectives, and the approach for conducting this research.

Chapter 2 provides a comprehensive review of different approaches used to design mine pillars. This chapter summarizes the failure mechanisms of hard rock pillars based on field observations. This is followed by a review of the empirical methods developed to estimate pillar stress and strength. Next, pillar stability databases developed for different mines are presented, which is followed by a comparison of the empirical formulas for estimating the pillar strength. Subsequently, numerical methods used to simulate pillar failure are

reviewed. Finally, a comparison between the pillar strength envelopes obtained from empirical and numerical modeling approaches is undertaken.

Chapter 3 presents the findings of numerical simulations of intact and heat-treated Wombeyan marble. In this chapter, the procedure for developing and calibrating a Grain-Based Model (GBM) in *RS2* is discussed in detail. The simulation results, including the failure modes and the strength envelopes, are compared with those of laboratory tests.

In Chapter 4, highly interlocked jointed pillars are simulated using the calibrated continuum GBM of heat-treated Wombeyan marble. The underlying assumption in this chapter is that the heat-treated Wombeyan marble is an analogue for a highly interlocked jointed rock mass. The GBM of heat-treated Wombeyan marble is first upscaled, and then used to simulate pillars of various W/H ratios. Next, the strength of jointed pillars derived from upscaled GBMs are obtained, and the results are compared to the jointed pillar stability curves obtained from other numerical models.

Chapter 5 provides a summary of this research, including the major findings, and presents recommendations for future work.

CHAPTER 2 LITERATURE REVIEW

2.1. INTRODUCTION

In this chapter, the failure mechanisms of hard rock mine pillars based on field observation, and different empirical and numerical approaches used for pillar design are reviewed. The specific topics covered in this chapter are:

- Failure mechanisms of mine pillars including structurally-controlled and stress-induced failure, and associated pillar classification/rating systems;
- Empirical pillar design approaches for determining the average pillar stress and estimating the pillar strength;
- Pillar stability databases developed for different mines;
- Simulation of progressive failure of hard rock pillars using different numerical methods; and
- Comparison between empirical and numerical pillar stability curves.

2.2. FAILURE MECHANISMS OF MINE PILLARS

The presence of geological structures and local stress conditions play important roles on the failure mechanisms of mine pillars. At shallow depths (i.e., < 1 km) and low in-situ stress conditions, geological structures control the failure mode of pillars. For example, rock wedges and blocks falling into openings from pillar walls and sliding pillar bodies along a single weak joint are typically observed at low stresses. The rock mass failure caused by the pre-existing geological structures is often referred to as structurally-controlled failure. An increase in the magnitude of in-situ stresses due to an increase in the mining depth results in the change in the mode of rock mass failure to spalling and slabbing near the pillar walls and shear failure through the pillar core (Martin and Maybee, 2000). This type of failure is referred to as stress-induced failure. In some cases, the stress-induced failure may be associated with a sudden release of energy (e.g., rock bursting; Kaiser and Tang, 1998). This section reviews both the structurally-controlled and stress-induced pillar failures observed in the field, and the associated pillar rating/classification systems developed for different mines.

2.2.1. Structurally-Controlled Failure

Esterhuizen et al. (2006) proposed a visual rating system to assess pillar stability conditions based on the data collected from 21 limestone mines in the Eastern United States. The surveyed limestone pillars have an average width of 14.5 m, and the W/H ratio varies from 0.53 to 3.52. This visual rating system was divided into two categories: The Geological Structure Rating (GSR) and the Pillar Stress Rating (PSR). Figure 2-1 illustrates the GSR used in these mines to evaluate the performance of pillars for structurally-controlled failure. Detailed descriptions of the GSR rating parameters are provided below:

- None – 1: Less than 0.3 m of jointed block falls during blasting (Figure 2-1a).
- Minor – 2: Pillar shape is affected by 0.3–1 m block fallout. Steps may be formed at the bedding planes. There is no or little further fallout after initial mining and scaling (Figure 2-1b).
- Moderate – 3: Pillar shape is affected by 1–3 m block fallout. There is continuous structurally-controlled fallout after initial mining and scaling.
- Severe – 4: Greater than 3 m block fallout. The pillar is re-shaped by large block extrusion and sliding along the steep plane. There is continuous structurally-controlled fallout after initial mining and scaling.
- Very severe – 5: Pillar is bisected with a throughgoing discontinuity dipping at more than 35º. The pillar strength depends on the strength of discontinuities.

The other category of this visual rating system, PSR, deals with pillars experiencing stress-induced failure, which is discussed in the next section.

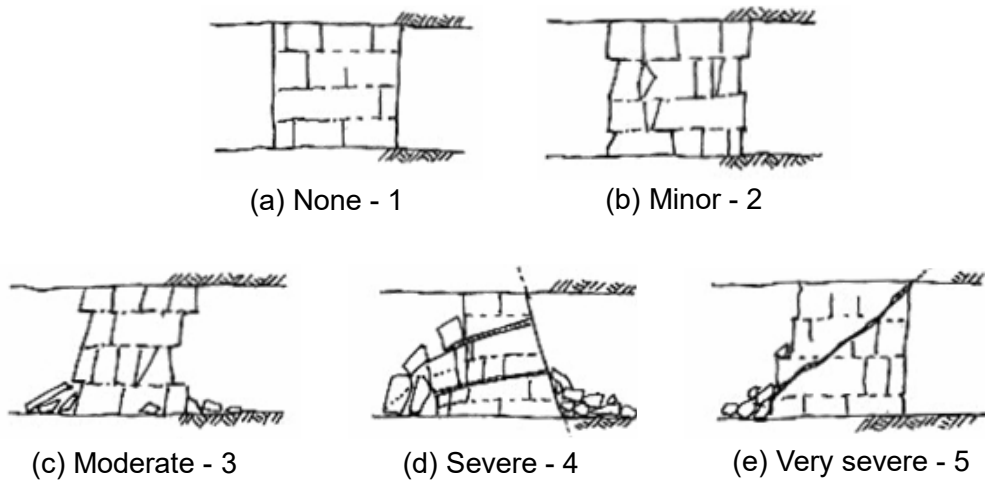

Figure 2-1: Geological Structure Rating (GSR) for pillars in limestone mines (Esterhuizen et al., 2006).

Brady and Brown (2006) provided a more comprehensive summary of structurally-controlled pillar failures under different geological conditions. As can be seen in Figure 2-2, typical structurally-controlled failures at low in-situ stress conditions are: 1) shear failure through the core of the pillars along an inclined joint (Figure 2-2a); 2) internal splitting within pillars with highly deformable (soft) planes (Figure 2-2b); 3) transgressive sliding for pillars with an inclined joint set (Figure 2-2c); and 4) buckling failure of the pillars with thinly bedded rock blocks (Figure 2-2d).

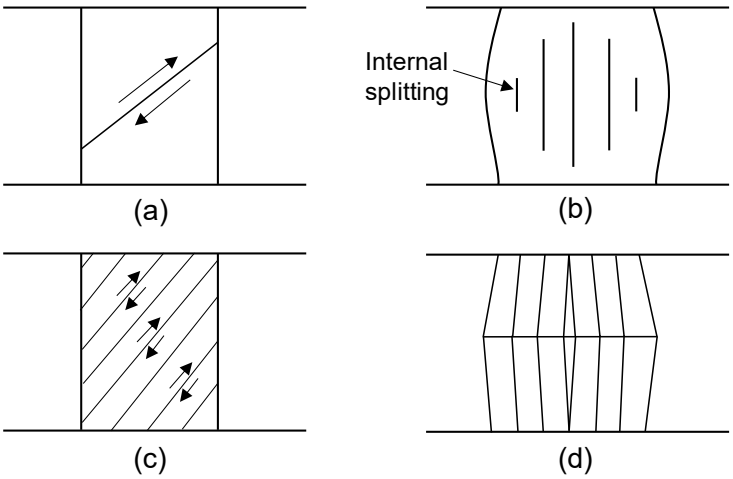

Figure 2-2: Structurally-controlled failures of pillars: a) single shear failure; b) internal splitting; c) transgressive sliding; and d) buckling failure (Brady & Brown, 2006).

2.2.2. Stress-Induced Failure

Pritchard and Hedley (1993) developed a pillar deterioration classification system and divided the progressive failure process of tilted (inclined) hard rock pillars in the Denison mine, ON, into six stages, as illustrated in Figure 2-3.

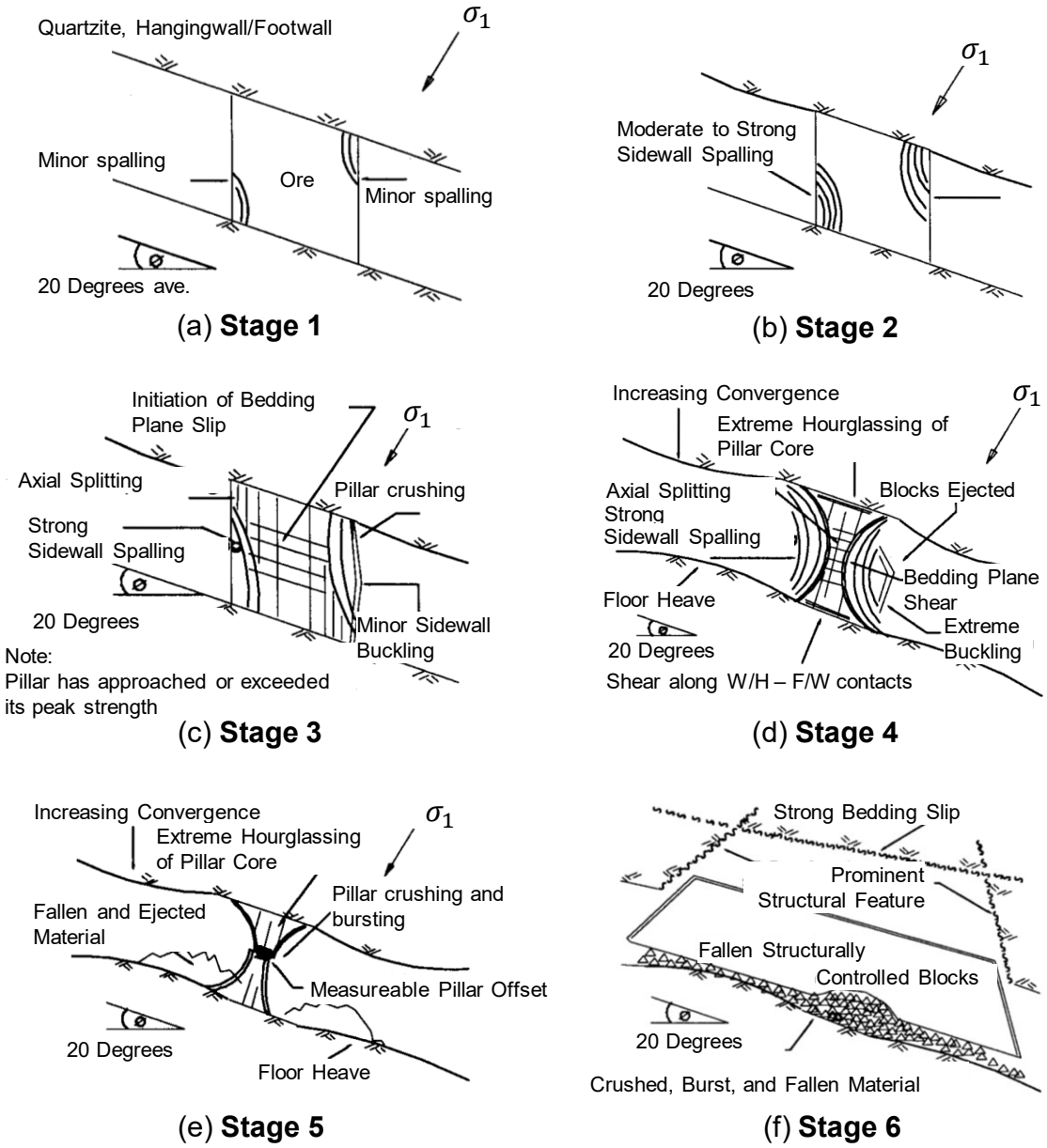

Figure 2-3: Failure process of tilted pillars observed in Denison mine, ON (after Pritchard and Hedley, 1993).

The description of each stage in this classification is provided below:

- Stage 1: Minor spalling is observed near the pillar walls (Figure 2-3a).
- Stage 2: Major spalling and slabbing are observed near the pillar walls (Figure 2-3b).
- Stage 3: Axial splitting within the pillar is observed and the fractures propagate towards the pillar core; (Figure 2-3c).
- Stage 4: The pillar exhibits an extreme spalling process at the walls, and rock slabs slide along the prominent bedding planes over time (Figure 2-3d).
- Stage 5: Fractures propagate and coalesce at the pillar core leading to the crushing of the pillar and severe rock bursting (Figure 2-3e). The pillar is at the final stage of its load-carrying capacity.
- Stage 6: Large roof failure occurs when the pillar support is diminished and the unsupported hanging wall is free to converge and fail (Figure 2-3f).

Lunder and Pakalnis (1997) introduced a pillar classification system that was used in the H-W mine of Westmin Resource Ltd. This system classifies the fracturing processes of massive hard rock pillars into five categories:

- Class 1: No signs of stress-induced fracturing (Figure 2-4a).
- Class 2: Pillar corners break up (Figure 2-4b).
- Class 3: Fracturing can be observed on the pillar walls (Figure 2-4c). The length of the fracture is less than half of the pillar height, and the aperture is less than 5 mm.
- Class 4: The length of the fracture is greater than half of the pillar height, and the aperture is between 5 mm and 10 mm (Figure 2-4d).
- Class 5: The pillar fails, and rock blocks fall out (Figure 2-4e). The fractures coalesce and propagate toward the center and eventually cut through the pillar core. The fracture aperture is greater than 10 mm.

The final mode of failure for the pillar is described as an “hour-glass” shape (Lunder & Pakalnis, 1997), as the pillar geometry is re-shaped by the spalling process resulting in a smaller width at the mid-height of the pillar compared to its initial width. Figure 2-4 illustrates the five stages of fracturing processes of hard rock pillars based on “the common pillar classification system” proposed by Lunder and Pakalnis (1997).

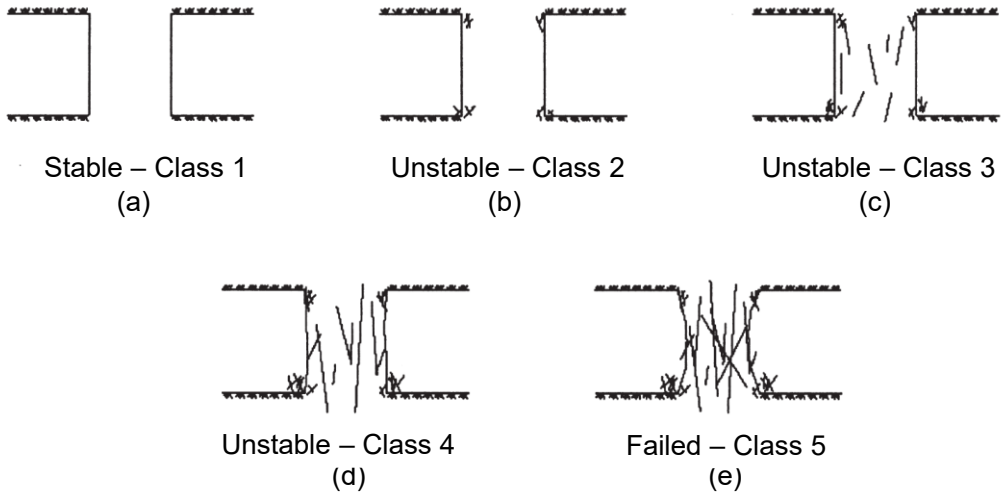

Figure 2-4: Schematic illustration of pillar stability classification used at Westmin Resource Ltd. (Lunder & Pakalnis, 1997).

Esterhuizen et al. (2006) proposed the Pillar Stress Rating (PSR) as a category of the visual rating system (described in Section 2.2.1) to assess stress-induced failure in hard rock pillars (Figure 2-5). A detailed description of the PSR is provided below:

- None – 1: No stress-related fracturing or spalling is observed within the pillar (Figure 2-5a).
- Minor – 2: Minor spalling and slabbing are observed near the pillar walls (Figure 2-5b).
- Moderate – 3: Spalling and slabbing are observed near the pillar walls. The length of the fractures is more than 1 m (Figure 2-5c).
- Severe – 4: The length of the open crack is more than 1 m and the square shape is no longer visible (Figure 2-5d).
- Very severe – 5: The formation of large open cracks leads to an extreme hour-glass shape. At this stage, the pillar has likely lost most of its residual strength (Figure 2-5e).

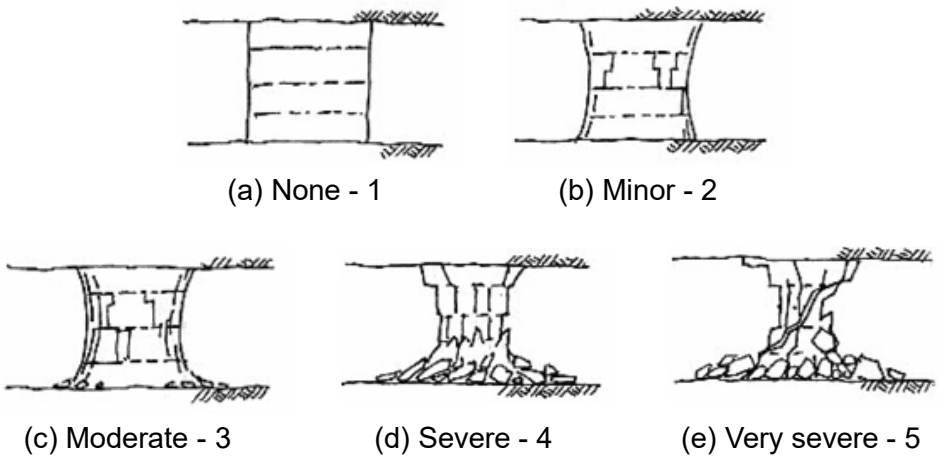

Figure 2-5: Pillar Stress Rating (PSR) in limestone mines (Esterhuizen et al., 2006).

Roberts et al. (2007) proposed a pillar rating system based on field observations in six underground lead mines in the US. Figure 2-6 presents the six classes of pillar conditions in this pillar rating system.

- Class 1: The pillar remains intact and there is no indication of stress-induced fractures (Figure 2-6a).
- Class 2: Minor spalling is observed at the pillar corners and pillar walls (Figure 2-6b). The length of the fractures is short relative to the pillar height (i.e., less than half of the pillar height).
- Class 3: Substantial spalling is observed at the pillar corners and walls (Figure 2-6c). The length of the fractures is up to half of the pillar height.
- Class 4: Continuous fractures propagate toward the pillar core (Figure 2-6d). Substantial spalling is observed at the pillar corner and walls. The length of the fracture is greater than half of the pillar height.
- Class 5: Large continuous open fractures cut through the pillar core (Figure 2-6e). The "hour-glass" shape is well-developed. Massive spalling and slabbing can be observed on the pillar walls.
- Class 6: The pillar completely fails, and an extreme "hour-glass" shape develops (Figure 2-6f left). Large rock blocks may fall out from the pillar walls (Figure 2-6f right). At this stage, the pillar only contains minimum residual load-carrying capacity.

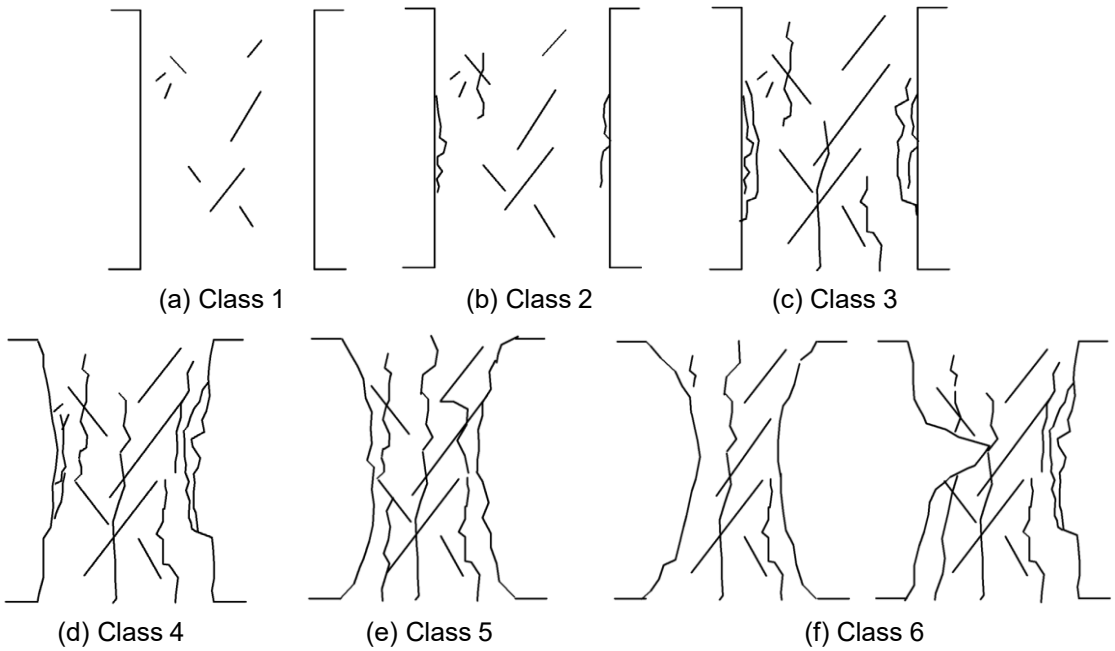

Figure 2-6: Pillar rating system proposed by Roberts et al. (2007).

The pillar rating/classification systems reviewed above have some commonalities in terms of fracturing processes in hard rock pillars under high in-situ stress conditions:

- First, fracturing starts at the corners of the pillar and propagates parallel to the pillar walls, leading to spalling and slabbing.
- Then, the fractures caused by spalling and slabbing propagate towards the pillar core, resulting in an "hour-glass" shape of the pillar (i.e., the width at the mid-height of the pillar is less than its original width).
- Finally, the fractures coalesce at the pillar core leading to a "crushed" pillar condition. The residual strength of the pillar tends to diminish and the crown/roof of the opening or the hanging wall is free to converge over time.

The pillar failure modes and mechanisms described above are solely from field observation of pillar performances. In the following section, empirical approaches for estimating average pillar stress and strength are presented, and the results are related to the field observations reviewed above.

2.3. EMPIRICAL PILLAR DESIGN APPROACHES

In empirical pillar design approaches, the Factor of Safety (FOS) is usually used to assess pillar stability. The FOS is calculated using the following equation:

$$FOS = \frac{Pillar\ strength}{Induced\ pillar\ stress} \qquad \textbf{Equation 2-1}$$

Where the pillar strength refers to the local strength of the pillar, and the induced pillar stress refers to the stress acting normal to the mid-height plane of the pillar. An FOS less than 1, in which the induced pillar stress is greater than the pillar strength, should be avoided unless the yielding of the pillar is needed. In order to determine the FOS of a pillar, accurate estimates of pillar stress and strength are necessary. This section reviews different methods used to estimate these two parameters.

2.3.1. Traditional Pillar Stress Estimation Methods

2.3.1.1. Tributary Area Theory

The tributary area theory is used to determine the average axial stress of pillars (i.e., average pillar stress), where the stress state or mining geometries are not complex (e.g., a vertical pillar under uniaxial loading in the room-and-pillar mining method). The theory was first developed by Bunting (1911) and later used by Salamon and Munro (1967), Hedley and Grant (1972), Pariseau (1982), Szwilski (1982) and Lunder and Pakalnis (1997) to estimate the average axial stress in a pillar. The theory implies that pillars "share" the load from adjacent openings. The assumption in this theory is that the vertical stress acting normal to the mid-height of the pillar is constant (i.e., confinement at the pillar core is not considered).

Figure 2-7 illustrates the plan view of typical squat pillars in the room-and-pillar mining method. The average stress of the pillar can be expressed as a function of the extraction ratio (e) according to the following equation:

$$\sigma_p = \frac{\gamma z}{1 - e}$$ **Equation 2-2**

In this equation, γ refers to the unit weight of the overburden, and z is the depth of the mid-height of the pillar from the ground surface. Therefore, the term γz represents the vertical stress acting normal to the mid-height of the pillar. Furthermore, e can be expressed as:

$$e = [(a + c)(b + c) - ab]/(a + c)(b + c)$$ **Equation 2-3**

where a and b are the side lengths of the pillar, and c represents the span of the opening, as shown in Figure 2-7.

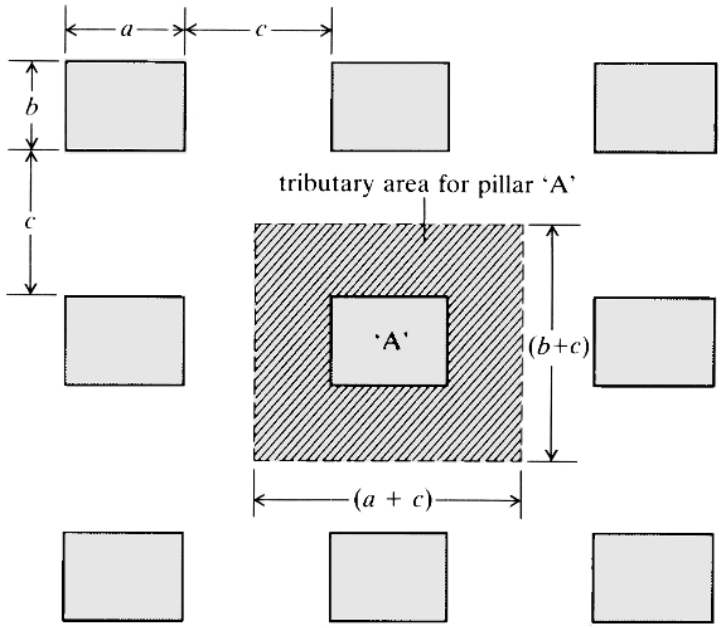

Figure 2-7: Plan view of squat pillars and the parameters for the tributary area analysis (Brady and Brown, 2006).

According to Hoek and Brown (1980), the tributary area theory is also applicable to irregular and long pillars (e.g., rib and barrier pillars). Note that for special cases, such as sill pillars, the stress acting normal to the mid-height centerline is the horizontal stress instead of the vertical stress. In this case, the term γz in Equation 2-2 might need to be modified to $k\gamma z$, where k refers to the in-situ stress ratio.

2.3.1.2. Numerical Modeling

Numerical modeling is a tool that can be used to simulate complex mine geometries, analyze induced stresses, and assess the stability of underground excavations. These are the distinct advantages of numerical modeling over the tributary area theory. In the last century and early 21st century, elastic continuum models have been used in different numerical programs to determine the average pillar stress. The numerical programs used for this purpose were based on the Boundary Element Method (BEM; e.g., *BITEM, MINTAB, BEAP, NFOLD, Examine2D/3D, and MAP3D*) and the Finite Element Method (FEM; e.g., *Phase2*). Due to the low computational power and associated long model runtimes, the numerical models used to determine the average pillar stress only considered the induced elastic stresses caused by mining activities. In other words, the stress redistribution due to rock mass yielding was not considered in these models. According to Hoek and Brown (1980) and Hudyma (1988), the average pillar stresses in the numerical models were calculated by averaging the vertical stresses (σ_{YY}) acting normal to the mid-height plane of the pillars.

2.3.2. Traditional Pillar Strength Estimation Methods

The estimation of pillar strength has been the subject of several investigations in the past few decades. Several researchers have created pillar stability databases for different mines by evaluating in-situ pillar performances, as described in Section 2.2. In this regard, several pillar stability graphs have been developed to present the rock mechanics data (i.e., stress and strength) for classified pillar conditions (i.e., stable, unstable, and failed pillar case histories). Each data point in the pillar stability graphs represents the ratio of average pillar stress to the UCS of intact rock specimen versus the W/H ratio of a particular pillar case. The empirical formulae (or curves) were then developed by fitting the data points in the pillar stability graphs to estimate the pillar strength. In this document, these empirical curves are referred to as the Pillar Stability Curves (PSC). A review of pillar stability databases and associated PSCs developed for different mines are provided in this section. Note that the pillar conditions indicated in these databases (i.e., stable, unstable, and failed)

are based on “the common pillar stability classification” proposed by Lunder and Pakalnis (1997).

Hedley and Grant (1972) analyzed the stability of pillar cases in the uranium mines in the Elliot Lake district of Ontario, Canada. In these mines, the main rock type is quartzite with UCS values ranging from 210 MPa to 275 MPa (Hedley & Grant, 1972). The database includes both squat and rib pillars. Figure 2-8 presents the case histories in the database with a total of 28 pillar cases, of which 23 cases are classified as stable, 2 are classified as unstable (or partially failed), and 3 are classified as failed (completely crushed). Hedley and Grant (1972) also developed a PSC to estimate the pillar strength as a function of pillar W/H ratio, as shown in Figure 2-8.

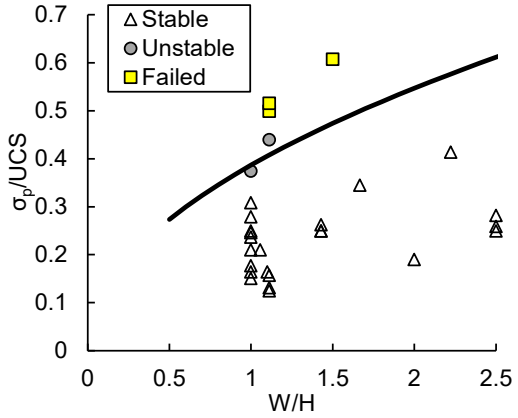

Figure 2-8: Pillar stability graph and the empirical PSC developed for Elliot Lake Uranium mines (after Hedley and Grant, 1972).

Von Kimmelmann et al. (1984) investigated the stability of pillars at the Selebi and Phikwe mines of BCL Ltd. in South Africa. The mechanical properties of the intact rock specimens are summarized in Table 2-1. Figure 2-9 presents the data for squat and long pillars collected from both mines. This database consists of a total of 57 pillar cases, including 15 stable pillars, 13 unstable pillars, and 29 failed pillars. The PSC developed by Von Kimmelmann et al. (1984) based on this database is also illustrated in Figure 2-9.

Table 2-1: Mechanical properties of intact rock specimens at Selbi-Phikwe mine (after Von Kimmelmann et al., 1984).

Pillar position	UCS (MPa)	Young's modulus (GPa)	Poisson's ratio
Hangingwall	89.0	88.8	0.25
Orebody	94.1	81.1	0.24
Footwall	189.1	90.7	0.26

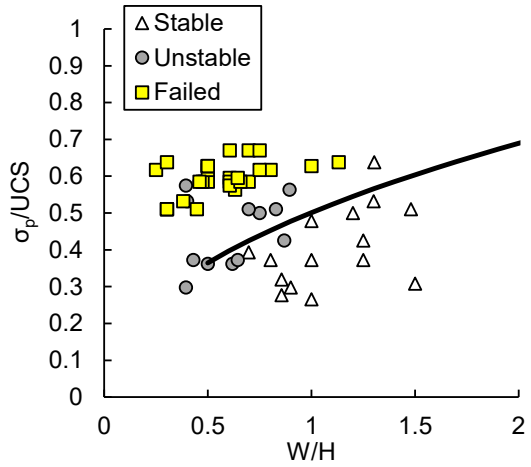

Figure 2-9: Pillar stability graph for Selbi-Phikwe mines and the empirical PSC proposed by Von Kimmelmann et al. (1984).

Hudyma (1988) and Potvin et al. (1990) analyzed the stability of rib pillars in open stope mines in the Canadian Shield. The UCS of the intact rock specimens ranges from 70 MPa to 316 MPa. The rib pillar stability data and the proposed PSC are presented in Figure 2-10. In total, the database consists of 47 pillar case histories, of which 26 cases are classified as stable, 9 are classified as unstable (sloughing), and 12 are classified as failed.

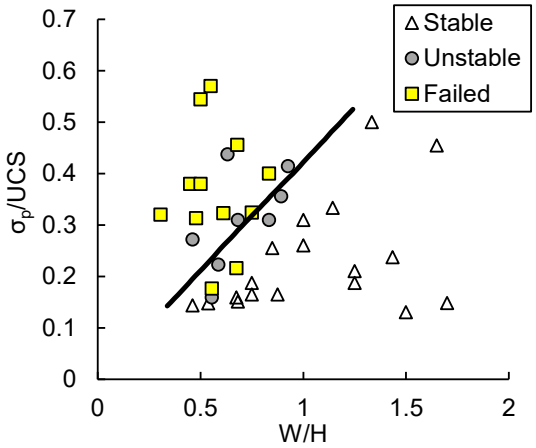

Figure 2-10: Pillar stability graph for rib pillars in Canadian open stope mines and the corresponding PSC proposed by Hudyma (1988) and Potvin et al. (1990).

Brady (1977), Krauland and Soder (1987), and Sjöberg (1992) collected limited pillar data from Mount Isa mines in Australia, the Black Angel mine in Greenland, and the Zinkgruvan mine in Sweden, respectively. Brady (1977) presented two stable and one failed rib pillar cases from Mount Isa mines in Australia. The ore bodies consist of bands of sphalerite, galena, and pyrrhotite in the bedded dolomitic, pyritic, and tuffaceous shale (Brady, 1977). The orebody rock has a UCS of 170 MPa and Young's modulus of 80 GPa (Brady, 1977). Krauland and Soder (1987) presented 14 unstable squat pillar cases in the Black Angle mine in Greenland. The main rock type in this mine is limestone, which has a UCS of 100 MPa. Sjöberg (1992) presented 4 unstable and 5 failed sill pillar cases in the Zinkgruvan mine in Sweden. The types of host rock are mainly limestone and skarn with UCS values ranging from 215 MPa to 265 MPa (Sjöberg & Tillman, 1990). Krauland and Soder (1987) and Sjöberg (1992) developed PSCs based on their databases. The combined pillar database for these mines and the PSCs are summarized and plotted together in Figure 2-11.

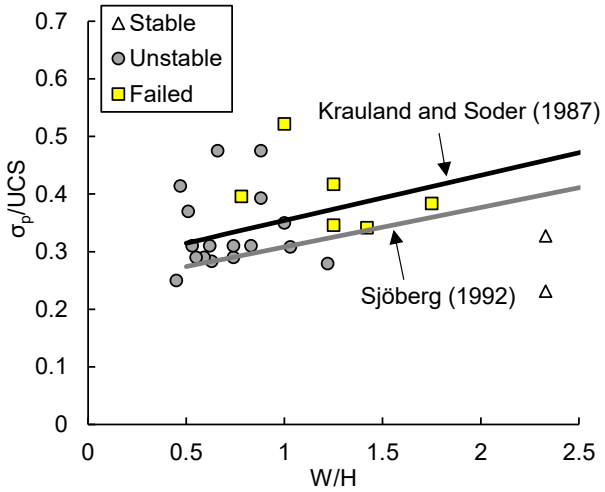

Figure 2-11: Pillar stability graph from Brady (1977), Krauland and Soder (1987), and Sjöberg (1992) and the proposed empirical PSCs.

Lunder and Pakalnis (1997) analyzed the stability of pillars at the H-W mine of Westmin Resources Ltd. in Canada. In this mine, the rock mass consists of massive sulphide with an average intact rock UCS of 172 MPa. The pillar stability database from this mine includes pillar case histories for discrete pillars (i.e., square or circular pillars), rib pillars, and nose pillars (1 or more side confined). A total of 31 pillar case histories were collected, of which 2 cases were stable, 11 were unstable, and 18 were failed (Figure 2-12).

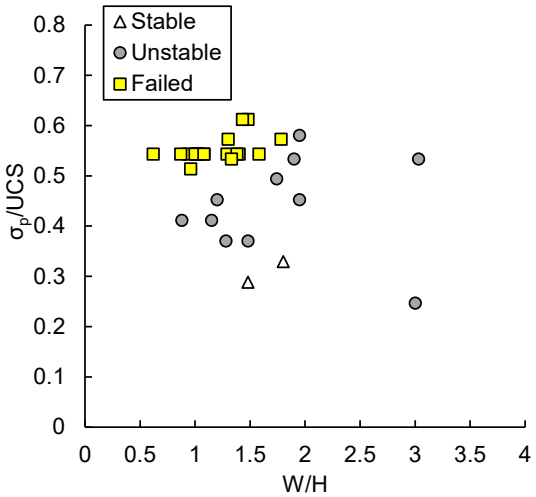

Figure 2-12: Pillar stability graph for H-W mine of Westmin Resource Ltd (Lunder and Pakalnis, 1997).

Lunder and Pakalnis (1997) combined the pillar stability databases created by Hedley and Grant (1972), Brady (1977), Von Kimmelmann et al. (1984), Krauland and Soder (1987), Potvin et al. (1990), and Sjöberg (1992), and that of the H-W mine. Since the pillar

classification systems in different mines used different criteria to assess the pillar conditions, Lunder and Pakalnis (1997) developed a "common pillar stability classification" (reviewed in Section 2.2.2) and applied it to all the databases. This combined database consists of a total of 68 failed pillars, 52 unstable pillars, and 58 stable pillars. Lunder and Pakalnis (1997) proposed a PSC based on this combined pillar stability database, as shown in Figure 2-13.

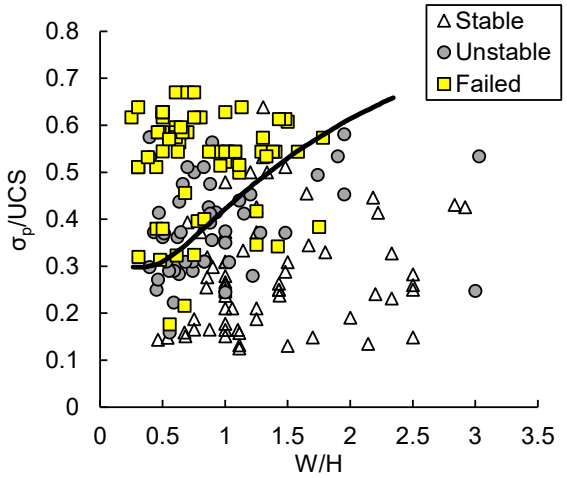

Figure 2-13: Pillar stability graph and the PSC proposed by Lunder and Pakalnis (1997) based on the combined stability database (after Brady, 1977; Hedley & Grant, 1972; Hudyma, 1988; Krauland & Soder, 1987; Lunder & Pakalnis, 1997; Sjöberg, 1992; Von Kimmelmann et al., 1984).

The pillar stability formulas developed from the databases reviewed above are summarized in Table 2-2 and their corresponding curves are plotted in Figure 2-14. Note that in the PSC proposed by Lunder and Pakalnis (1997), the term κ, called the 'mine pillar friction term', is a function of the average pillar confinement, and therefore, the pillar W/H ratio. As can be seen in Figure 2-14, the empirical PSCs follow a similar trend in terms of the slope and non-linearity of the curves, except for that proposed by Potvin et al. (1990), which is linear and has a much higher slope than the rest.

In general, different empirical PSCs suggest different ratios of the pillar stress to the intact rock strength (σ_p/UCS) for a given pillar W/H ratio. This could be due to the following reasons: 1) in different mines, different classifications and criteria were used to assess pillar conditions; 2) the databases and their corresponding PSCs were developed based on in-situ performances of different types of pillars (e.g., sill pillars, squat pillars, and rib pillars); and 3) the actual failure modes (i.e., structurally-controlled and stress-induced failures)

were not reported in the references, although it is expected that most of them are stress-induced failures.

Table 2-2: Empirical strength formulas for hard rock pillar summarized by Renani and Martin (2018).

Pillar strength, σ_p (MPa)	σ_c (MPa)	Rock mass type	No. of pillars	References
$133(W^{0.5}/H^{0.75})$	230	Quartzite	28	Hedley and Grant (1972)
$65(W^{0.46}/H^{0.66})$	94	Metasediments	57	Von Kimmelmann et al. (1984)
$35.4[0.778 + 0.222(W/H)]$	100	Limestone	14	Krauland and Soder (1987)
$0.42\sigma_c(W/H)$	70-316	Canadian Shield	23	Potvin et al. (1990)
$74[0.778 + 0.222(W/H)]$	240	Limestone/Skarn	9	Sjöberg (1992)
$0.44\sigma_c(0.68 + 0.52\kappa)$	172	Massive sulphide	31	Lunder and Pakalnis (1997)

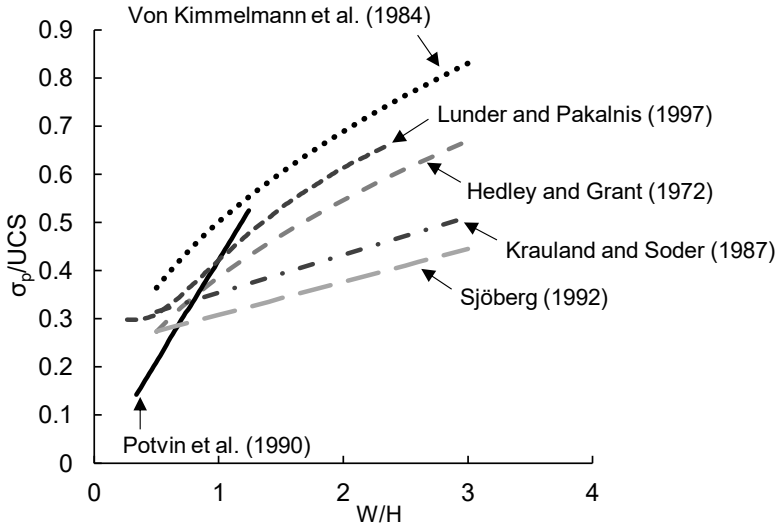

Figure 2-14: Comparison between empirical PSCs for hard rock pillars.

2.4. NUMERICAL SIMULATION OF HARD ROCK PILLARS

Numerical methods typically used to study the mechanical behavior of brittle rocks include: 1) continuum (e.g., FEM); 2) discontinuum (e.g., Discrete Element Method, DEM); and 3) hybrid continuum-discontinuum (e.g., hybrid Finite-Discrete Element Method, FDEM) methods. The progressive failure of massive to moderately jointed hard rock pillars can be

simulated in continuum numerical programs by assigning different failure criteria (e.g., Hoek-Brown and Mohr-Coulomb) and constitutive laws (e.g., elastic-brittle and strain softening). In elastic models, the FOS or strength factor is usually used to assess the pillar stability. In inelastic models, yielded elements/zones can be used as an indication of rock mass failure. Furthermore, the progressive failure of jointed hard rock pillars can be simulated in discontinuum and hybrid continuum-discontinuum methods as long as the rock joints, which simulated as frictional or cohesive contacts, are integrated into the numerical models.

In this section, numerical approaches based on the continuum and discontinuum methods used to simulate the failure of hard rock pillars are reviewed. The PSCs developed based on the results of the numerical simulations of hard rock pillars are also presented and compared with various pillar stability charts.

2.4.1. Continuum Methods

Martin and Maybee (2000) used *Phase2* (former version of *RS2* by Rocscience) to investigate the influence of rock mass quality on the strength of jointed pillars. The numerical program *Phase2* is based on the implicit FEM. In their study, the rock mass was simulated as a homogeneous material and the Hoek-Brown parameters for GSI values of 40, 60, and 80 were used to determine the PSCs, as shown in Figure 2-15. However, they discussed that the simulation results using the Hoek-Brown failure criterion for GSI 40, 60 and 80 do not follow the trends of the stability lines proposed by Hedley and Grant (1972) or Lunder and Pakalnis (1997).

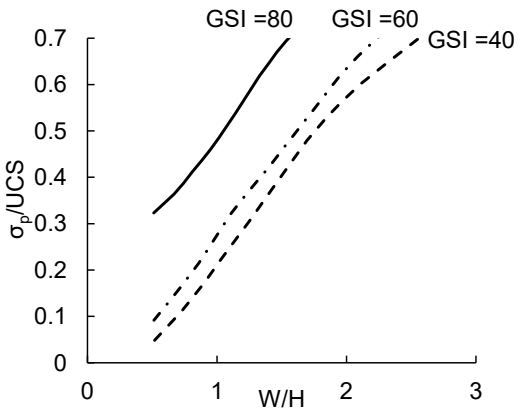

Figure 2-15: The PSCs obtained from the continuum numerical models of jointed rock pillars by Martin and Maybee (2000).

Martin and Maybee (2000) also used elastic models with the Hoek-Brown brittle parameters (s = 0.11, and m_b = 0) in *Phase2* to estimate the strength of massive to moderately jointed hard rock pillars in the Canadian Shield. The Hoek-Brown brittle parameters were initially proposed by Martin et al. (1999) to predict the depth of brittle failure around tunnels. The assumption in this approach is that the failure process of massive brittle rocks at low confinement is dominated by cohesion loss. Therefore, the frictional strength component in the Hoek-Brown criterion (i.e., m_b) can be assigned a low or zero value in elastic models (Martin et al., 1999; Martin & Maybee, 2000). Martin and Maybee (2000) and Maybee (2000) used the strength factor of 1 at the pillar core as an indication of pillar failure in their continuum elastic models. In Figure 2-16, it can be seen that the PSCs obtained from their numerical simulations for FOS of 1 and 1.4 agree well with the combined pillar stability database presented by Lunder and Pakalnis (1997).

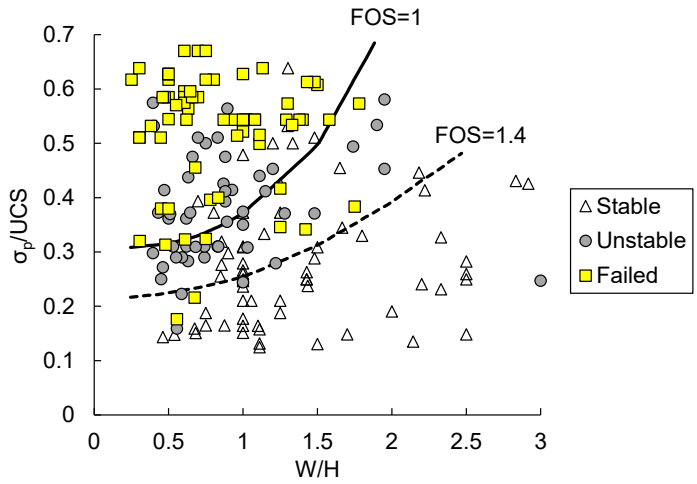

Figure 2-16: Comparison of the pillar stability data and PSCs from *Phase2* elastic models with Hoek-Brown brittle parameters (Martin & Maybee, 2000).

Mortazavi et al. (2009) used the two-dimensional continuum program, *FLAC*, to investigate the non-linear behavior of pillars as a function of the pillar W/H ratio. *FLAC* is a numerical program based on the Finite Difference Method (FDM). In their simulations, the host rock was assumed to be elastic, and the pillar was simulated as a strain-softening material using the Mohr-Coulomb parameters. In their models, the stopes were gradually excavated from the two sides of the pillar, which allowed the stresses to be redistributed within the pillar. They found that the pillars exhibited a softening behavior at small W/H ratios (i.e., 0.5 to 1.5), and became strain-hardening when the W/H ratio was greater than 2, as shown in Figure 2-17.

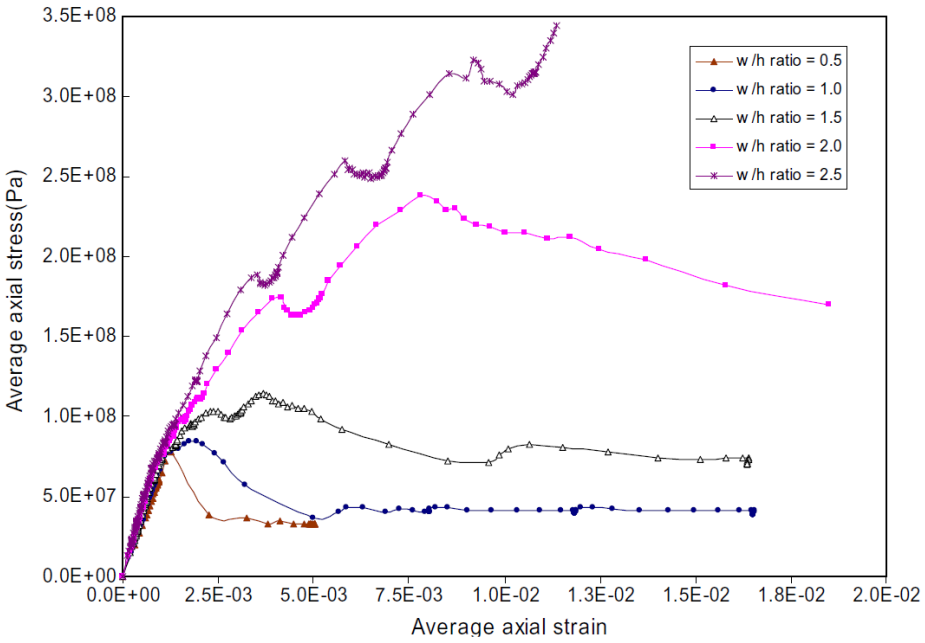

Figure 2-17: Average pillar stress versus axial strain curves obtained from numerical simulation of hard rock pillars with strain softening material behavior by Mortazavi et al. (2009).

Figure 2-18 shows the PSCs obtained from the simulation results for FOS of 1 and 1.5, and their comparison with the pillar stability data compiled by Lunder and Pakalnis (1997). As can be seen in this figure, the PSCs increase non-linearly with an increase in the W/H ratio. It is concluded that the curve for FOS = 1 generally agrees with the combined pillar stability data (Figure 2-18) up to a W/H ratio of 1.5. The numerically estimated PSCs suggest that pillars with W/H ratios greater than 1.8 seem to be indestructible.

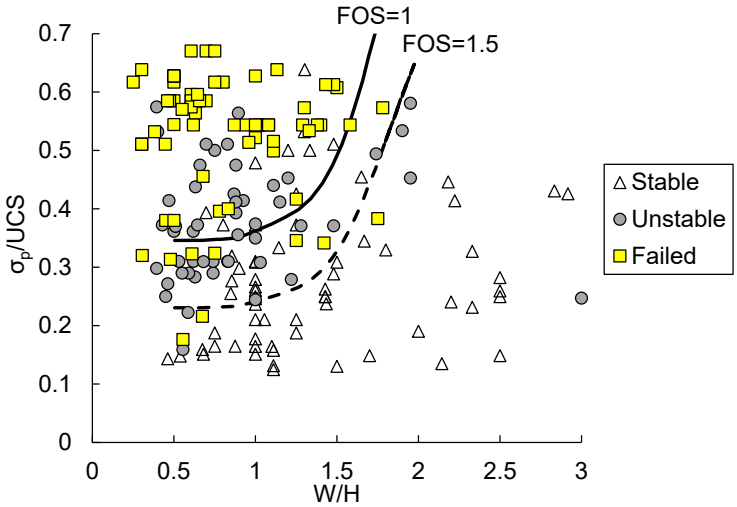

Figure 2-18: Comparison of pillar stability data and *FLAC* modeling results using the strain softening material behavior with Mohr-Coulomb strength parameters (Mortazavi et al., 2009).

Kaiser et al. (2011) proposed a modified Hoek-Brown failure criterion for massive to moderately jointed rock mass. They introduced a modified GSI parameter (i.e., GSI′), which is a function of the confining pressure and the GSI. They replaced the original GSI in the generalized Hoek-Brown failure criterion with GSI′, which can be obtained using the following equation:

$$GSI' = \frac{M - \left(\frac{M}{100}\right) GSI}{1 + e^{-\sigma_3 + \frac{\sigma_{ci}}{10}}} + GSI \qquad \textbf{Equation 2-4}$$

In the above equation, σ_{ci} is the uniaxial compressive strength for the intact rock obtained from laboratory tests, σ_3 is the confining pressure at failure, and M is a constant that controls the strength degradation at elevated confinement (i.e., $\sigma_3 > \sigma_{ci}/10$).

The strength envelopes obtained from the original and modified Hoek-Brown failure criteria for different values of GSI are compared in Figure 2-19. As can be seen in Figure 2-19b, the modified Hoek-Brown strength envelope is an S-shaped curve with different strength degradations at low and high confinement. Kaiser et al. (2011) discussed that since the tensile failure is inhibited at high confinement, the rock mass strength degradation from the intact strength should be lower at high confinement (i.e., $\sigma_3 > \sigma_{ci}/10$) than that at low confinement (i.e., $\sigma_3 < \sigma_{ci}/10$). Therefore, this conceptual approach estimates a higher strength at high confinement compared to the original Hoek-Brown criterion, as demonstrated in Figure 2-19.

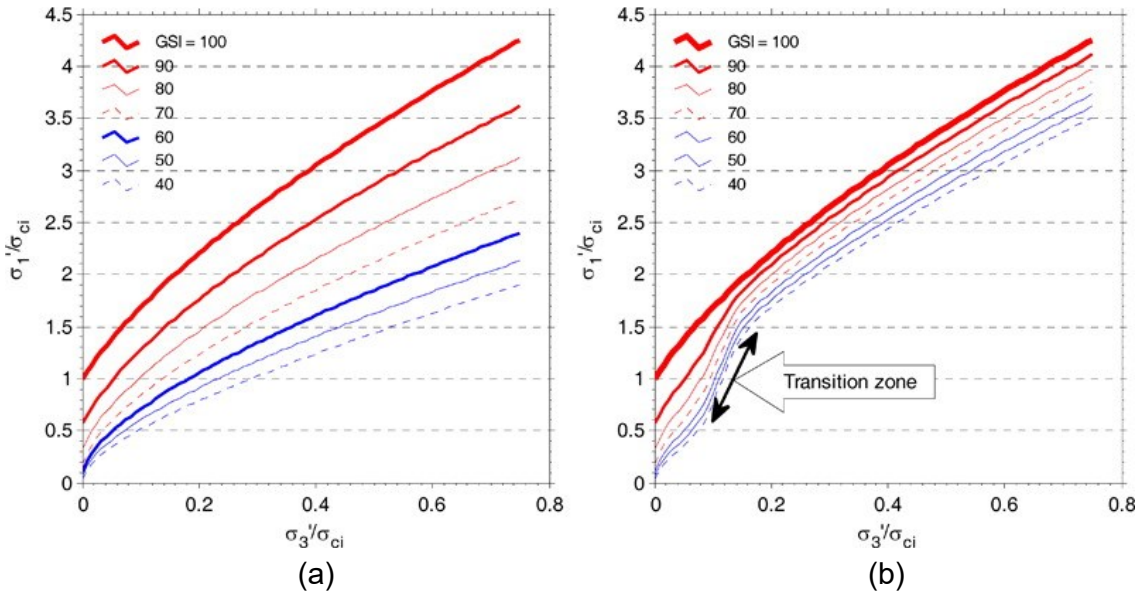

Figure 2-19: Comparison between: a) original Hoek-Brown failure criterion; and b) modified Hoek-Brown failure criterion for various GSI values (after Kaiser et al., 2011).

The modified Hoek-Brown criterion (i.e., S-shaped criterion) was then used to simulate hard rock pillars in *Phase2*. Figure 2-20 compares the pillar stress-strain curves obtained from both the modified and original Hoek-Brown criteria. The modeling results indicate that the model based on the original Hoek-Brown criterion with the GSI strength equations systematically underestimate the pillar strength for W/H ratios greater than 1.5.

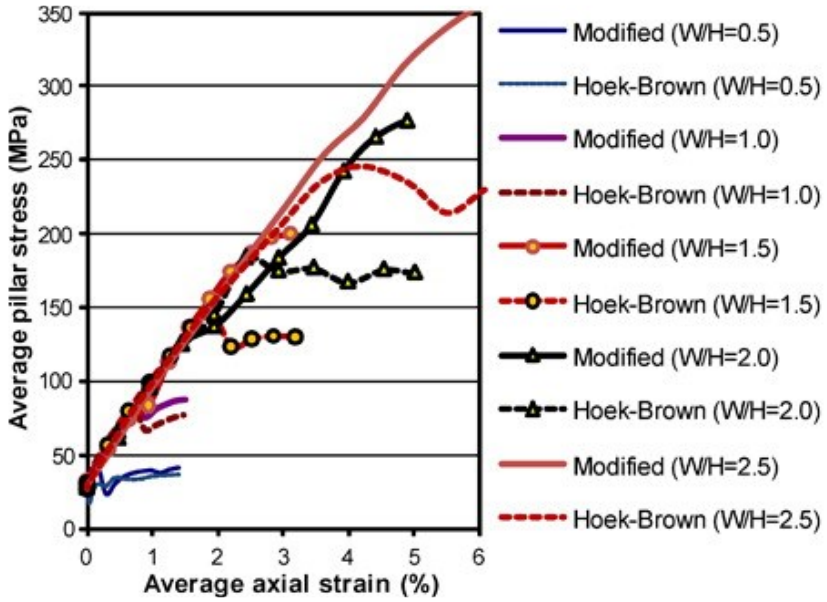

Figure 2-20: Comparison between pillar stress-strain curves obtained from continuum models with original and modified Hoek-Brown failure criteria (Kaiser et al., 2011).

Sinha and Walton (2018) developed a progressive S-shaped yield criterion in the three-dimensional (3D) FDM program, *FLAC3D*, to investigate the pillar strength as a function of the pillar W/H ratio. Three components of this complex criterion (i.e., yield, peak, and residual envelopes) are shown in Figure 2-21. The blue dashed line in this figure is used to divide the left and right portions of the three envelopes (Figure 2-21). In the yield envelope, the left portion corresponds to the Crack Initiation (CI) threshold, and the right portion follows the modified Mogi's line. In the peak envelope, the left portion is coincident with the Spalling Limit (SL), while the right portion is defined by the Crack Damage (CD) threshold. The residual envelope is obtained through simultaneous degradation of both the portions of the peak envelope (Sinha and Walton, 2018).

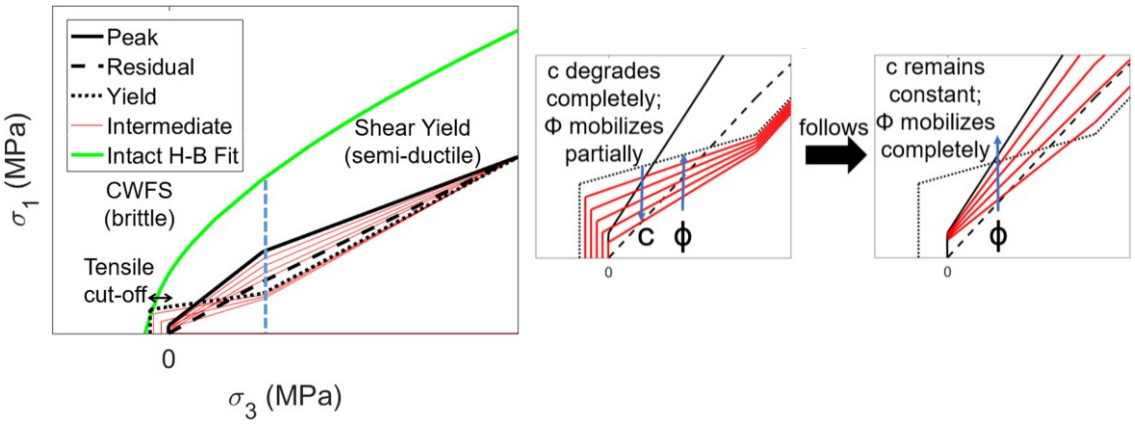

Figure 2-21: Schematic representation of progressive S-shaped yield criterion proposed by Sinha and Walton (2018).

Sinha and Walton (2018) used their progressive S-shaped yield criterion to simulate hard rock pillars with varying W/H ratios. The stress-strain curves along with the progressive failures of pillars with W/H ratios of 1, 2, and 3 are illustrated in Figure 2-22. As can be seen in the figure, pillars with W/H ratios greater than 2 exhibit a strain-hardening behavior. The numerically estimated PSC along with the pillar stability data collected by Lunder and Pakalnis (1997) are shown in Figure 2-23. In this figure, the PSC clearly differentiates between the stable and failed pillar cases in the combined pillar stability database (Sinha and Walton, 2018), although 2 failed cases small W/H ratios are still below the proposed PSC.

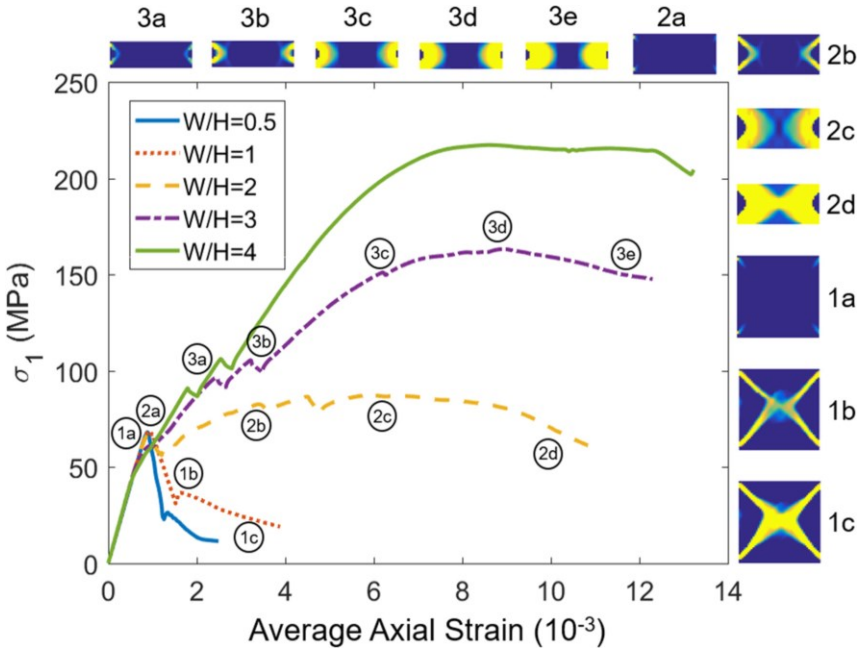

Figure 2-22: Stress-strain curves for pillars with width-to-height ratios of 0.5, 1, 2, 3 and 4 obtained from *FLAC3D* models with progressive S-shaped yield criterion (Sinha and Walton, 2018).

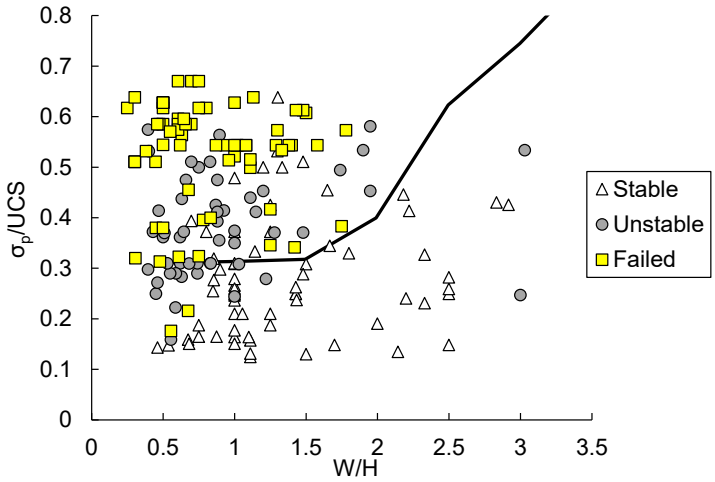

Figure 2-23: PSC from *FLAC3D* models with progressive S-shaped yield criterion (Sinha & Walton, 2018) compared to the pillar stability data compiled by Lunder and Pakalnis (1997).

Renani and Martin (2018) simulated hard rock pillars in the Elliot Lake uranium and Selebi-Phikwe mines using the 3D FDM program, *FLAC3D*, by implementing a strain-dependent non-linear Cohesion Weakening-Frictional Strengthening (CWFS) model. A linear CWFS approach was first implemented in *FLAC* by Hajiabdolmajid et al. (2000) to simulate brittle rock failure near underground openings. In the non-linear CWFS model,

both the cohesion and friction angle are functions of the plastic shear strain ε^p (Figure 2-24). As can be seen in this figure, cohesion is weakened before the frictional strength is fully mobilized as the plastic shear strain increases.

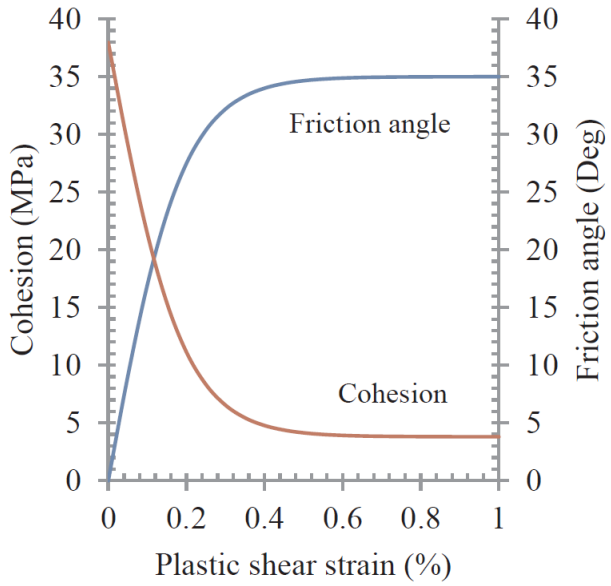

Figure 2-24: Non-linear CWFS model proposed by Renani & Martin (2018).

The pillar axial stress versus axial strain curves obtained by *FLAC3D* with the non-linear CWFS model are shown in Figure 2-25. The stress-strain curves exhibit brittle response for slender pillars (i.e., W/H = 0.5 and 1), strain-softening behavior for wider pillars (i.e., W/H = 1.5 and 2), and strain-hardening behavior for pillars with W/H ratios greater than 2.5. The results agree well with those obtained by Mortazavi et al. (2009) and Sinha and Walton (2018).

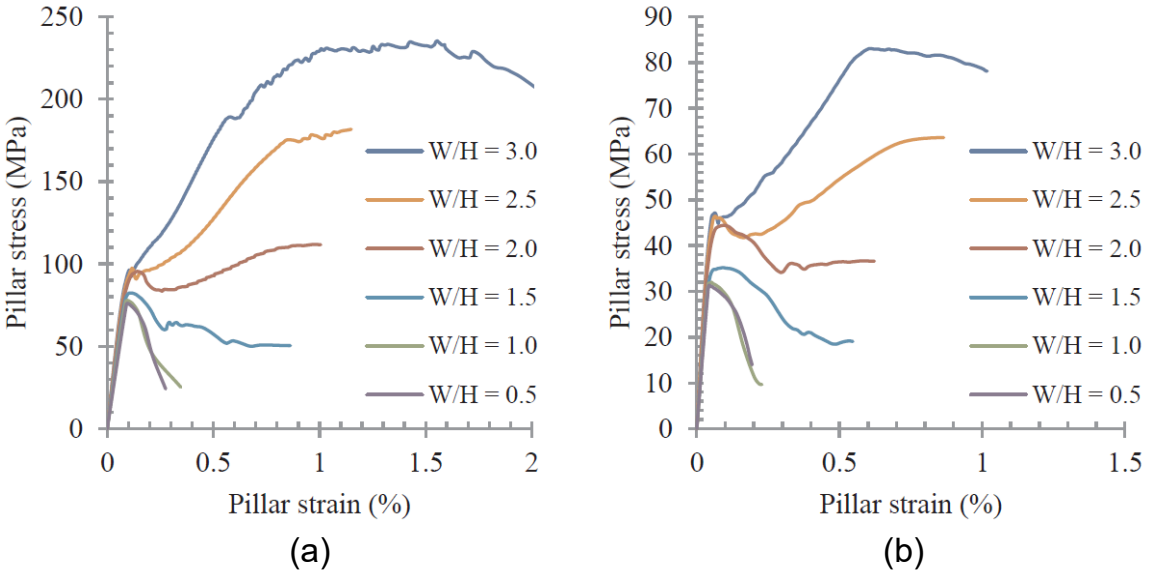

Figure 2-25: Average stress versus axial strain curves using non-linear CWFS model in *FLAC3D* (Renani & Martin, 2018) for pillars at: a) Elliot Lake mine; and b) Selebi-Phikwe mine.

As illustrated in Figure 2-26, the PSCs obtained from the simulation of pillars at Elliot Lake and Selebi-Phikwe mines show good agreements with the field data. As discussed by Renani and Martin (2018), the non-linear CWFS model shows more conservative estimations of the pillar strength at W/H ratios between 0.5 and 2, and predicts a higher strength than empirical approaches at W/H ratios greater than 2 (Elliot Lake) and 2.5 (Selebi-Phikwe).

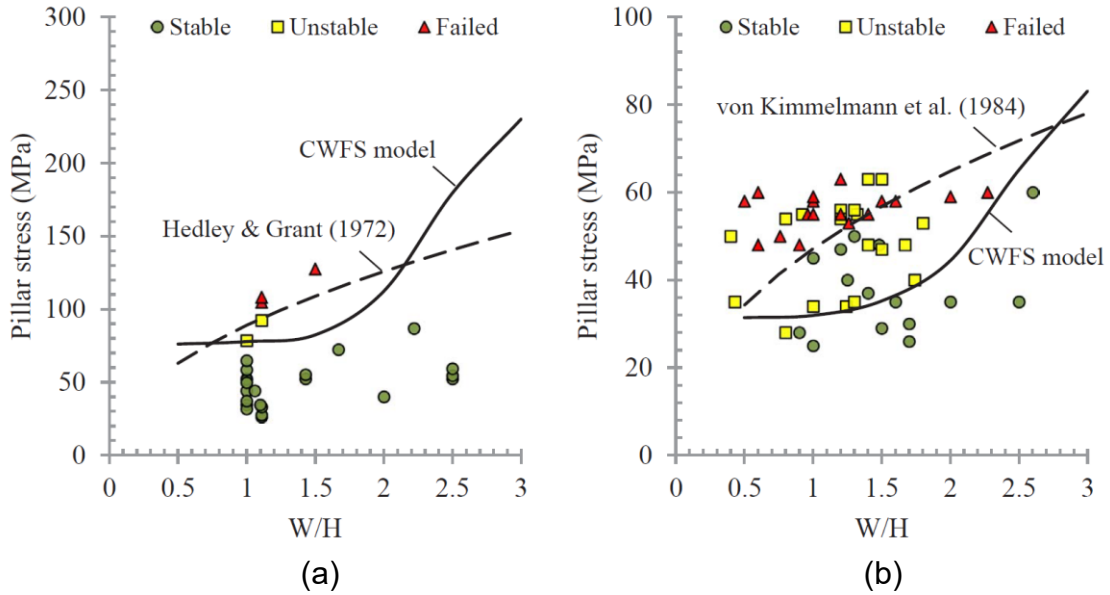

Figure 2-26: PSCs obtained from *FLAC3D* models with non-linear CWFS material behavior for: a) Elliot Lake uranium mines; and b) Selebi-Phikwe mines (Rafiei Renani & Martin, 2018).

2.4.2. Discontinuum Methods

The advantage of discontinuum methods over continuum methods is that progressive fracturing of hard brittle rocks under various loading conditions can be explicitly simulated. In continuum methods, the intact rock failure is only represented by yielded elements/zones, when the stress within the element/zone exceeds the assigned strength. However, in discontinuum methods, fracture initiation at pre-peak loading stages and their propagation, which may result in the detachment of rock pieces, can be explicitly simulated. In this section, some of the most important numerical simulations of hard rock pillars conducted using discontinuum programs are briefly reviewed.

One of the first numerical simulations of pillar fracturing processes using the discontinuum method (i.e., *PFC* by Itasca) was conducted by Diederichs (2000). Figure 2-27a shows the *PFC* model of a pillar consisting of nearly 9,000 circular particles (disks) bonded together at their contact points. Diederichs (2000) simulated pillar loading by increasing the axial stress using a wall at the top boundary of the *PFC* model. The pillar was loaded until the core was yielded. Figure 2-27b shows the compressive forces within the pillar model before it reaches the peak stress. As can be seen in this figure, the pillar core is highly confined, and spalling occurs on the pillar walls.

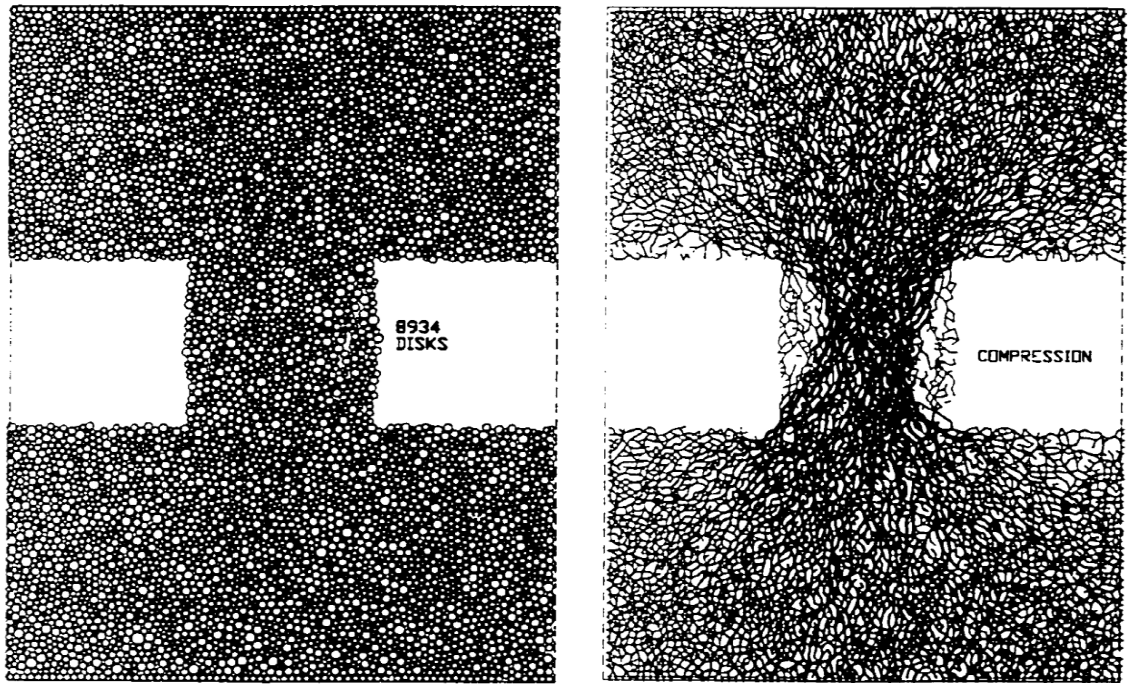

Figure 2-27: a) A pillar model developed in *PFC* by Diederichs (2000); b) distribution of compressive forces immediately prior to core yielding.

Elmo and Stead (2010) integrated a Discrete Fracture Network (DFN) model into the numerical program, *ELFEN* (by Rockfield), to simulate the jointed pillars in the Middleton mine, UK. *ELFEN* is a program based on the hybrid Finite-Discrete Element Method (FDEM). By integrating the DFN into the numerical models, the discontinuities at the rock mass scale can be explicitly simulated. This rock mass model is called the Synthetic Rock Mass (SRM). Figure 2-28 shows the fracturing processes of jointed pillars with different W/H ratios. They also investigated the influence of fracture intensity (i.e., P_{21}) on the pillar strength. The PSCs for P_{21} values of 1.8 and 2.6 are also shown in Figure 2-29. As evident from this figure, the strength of slender pillars (i.e., W/H = 0.5) estimated by the P_{21} value of 2.6 is below 10% of the intact rock UCS. Based on this result, Elmo and Stead (2010) concluded that the failure of slender pillars is predominantly controlled by naturally occurring discontinuities, and the impact of discontinuities diminishes as the pillar width increases. Furthermore, the spalling process on the pillar walls is captured in wider pillar models (Figure 2-28), which is consistent with field observations described in Section 2.2.2.

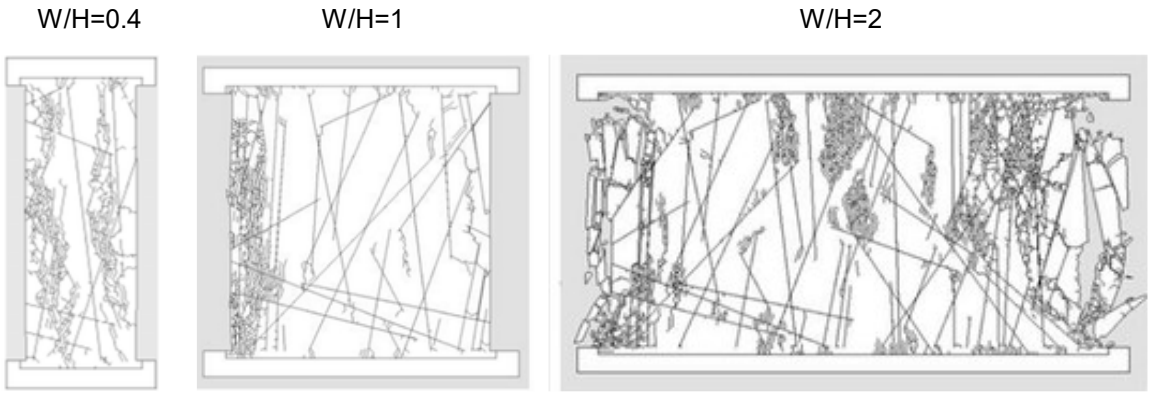

Figure 2-28: Fracturing evolution and failure modes of jointed pillars captured by *ELFEN* (Elmo & Stead, 2010).

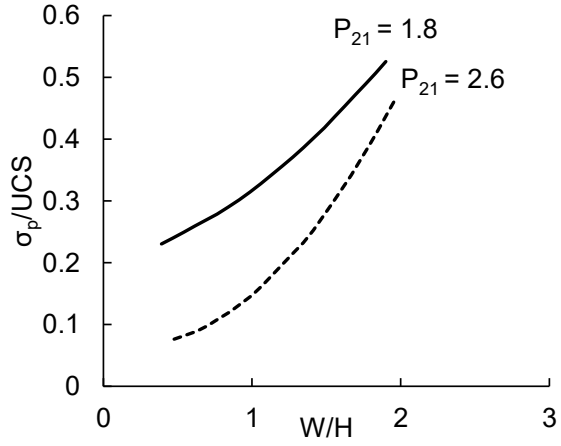

Figure 2-29: The PSC obtained from the discontinuum numerical models of jointed rock pillars by Elmo and Stead (2010).

Esterhuizen et al. (2011) used the two-dimensional discontinuum program, UDEC, to investigate the effect of a single discontinuity on the pillar strength. Figure 2-30a shows the PSC of a pillar with no discontinuity compared to that affected by a discontinuity dipping at 60°. In their study, Esterhuizen et al. (2011) concluded that the discontinuity caused a much greater reduction in pillar strength in slender pillars (i.e., W/H < 1.0).

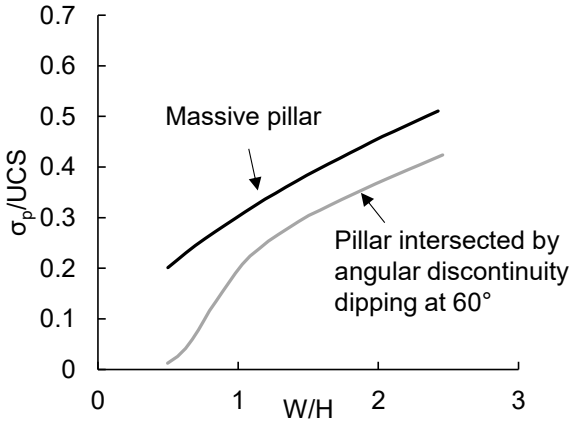

Figure 2-30: The PSCs obtained from the discontinuum numerical models of massive and jointed pillars by Esterhuizen et al. (2011).

Li et al. (2019) simulated the progressive failure of massive granitic pillars at the Creighton mine in Canada using a combined continuum-discontinuum program, *IRAZU* (by Geomechanica). The simulation results for the pillars of different W/H ratios are shown in Figure 2-31. The stress-strain curves obtained from these models show a brittle behavior in a slender pillar, which then become hardening as the pillar W/H ratio increases. These results are consistent with those of continuum models (e.g., Mortazavi et al., 2009; Rafiei Renani & Martin, 2018; Sinha & Walton, 2018). Furthermore, the brittle damage leading to spalling, the detachment of rock blocks from the pillar walls, and the inclined shear fractures through the pillar cores are well captured by the *Irazu* models.

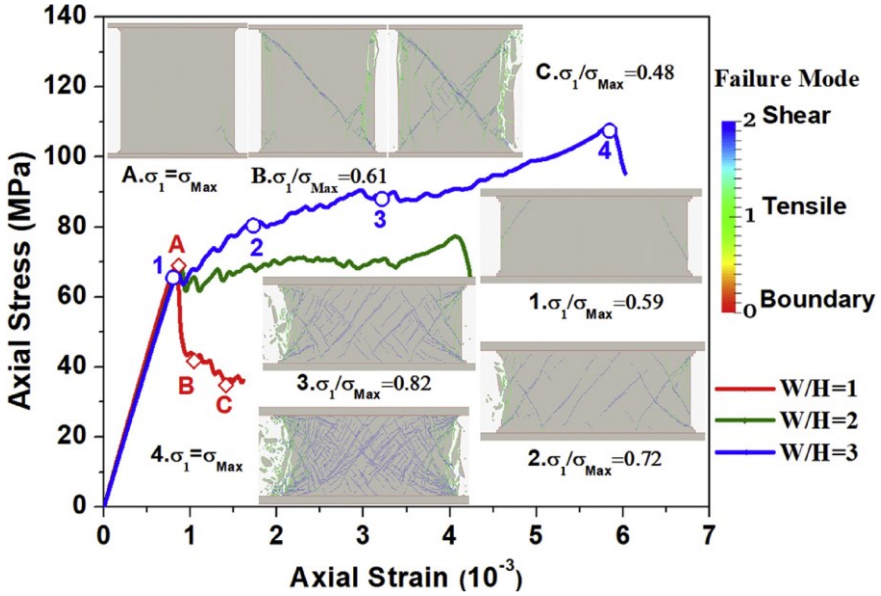

Figure 2-31: Stress-strain response and failure process of massive granitic pillars simulated using a hybrid continuum-discontinuum model by Li et al. (2019).

2.5. SUMMARY

This chapter first summarized structurally-controlled and stress-induced failures of hard rock pillars from field observations. The failure of pillars at shallow depths (i.e., low in-situ stress conditions) is controlled by the presence of discontinuities. As the mining depth, and therefore, in-situ stress magnitude increases, the spalling of the pillar walls leading to an hour-glass shape becomes the dominant mode of failure for hard rock pillars.

The empirical and numerical pillar design approaches were also reviewed in this chapter. The numerical approaches have shown a distinct advantage over the empirical approaches with regards to the estimation of average pillar stress and strength. By considering different failure criteria and constitutive models, the progressive failure of hard rock pillars under an overall compressive loading condition can be captured using both the continuum and discontinuum numerical methods.

Figure 2-32 shows a comparison between the PSCs of massive to moderately jointed hard rick pillars obtained from the empirical and numerical approaches. The numerical PSCs generally agree with most of the empirical PSCs for W/H ratios less than 1.5. However, the numerical PSCs suggest that the pillar strength increases more rapidly when the W/H ratio is greater than 1.5, which results in steeper curves than those of the empirical PSCs. This is because the combined pillar stability database (Figure 2-13) includes limited failed case histories for pillars with W/H ratios greater than 1.5, resulting in flatter curves as compared to those of numerical PSCs. For this reason, Martin and Maybee (2000) suggested that the applicability of the empirical PSCs should be limited to pillars with W/H ratios less than 2. The empirical PSCs suggest a more conservative design for wider pillars, which may lead to overdesigned pillars, and therefore, loss of ore and profit for the mining companies.

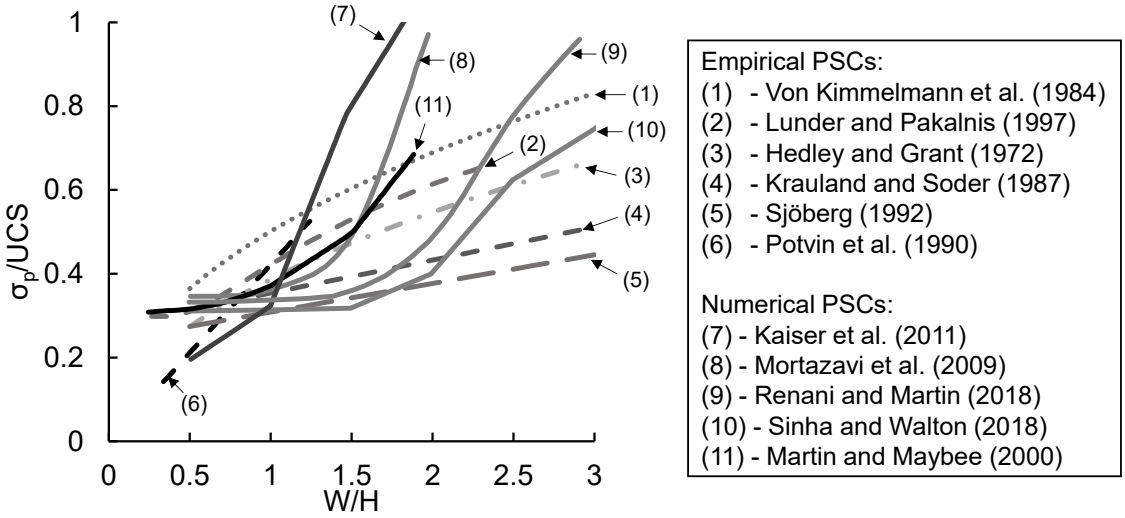

Figure 2-32: Summary of PSCs obtained from empirical methods (dashed/dotted lines) and numerical modeling (solid lines) for massive to moderately jointed pillars.

Figure 2-33 shows a comparison between PSCs of jointed pillars obtained from the continuum and discontinuum numerical approaches. In all these cases, the pillar strength increases rapidly with the increase in the W/H ratio. The slopes of PSCs from these studies as well as those of massive pillars obtained from continuum modeling are steeper than the empirical PSCs (Figure 2-32), indicating the effect of increasing confinement on the pillar strength with increasing the W/H ratio. Unfortunately, there is no stability database for jointed pillars for comparison with numerical modeling results presented in Figure 2-33.

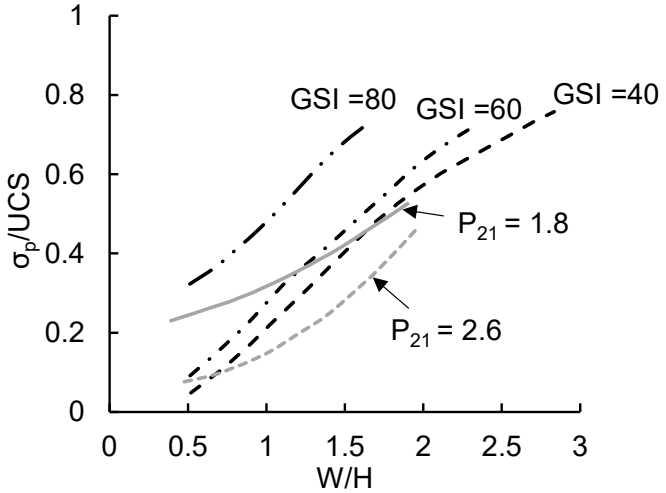

Figure 2-33: Summary of PSCs obtained from continuum and discontinuum numerical models of jointed rock mass by Martin and Maybee (2000) and Elmo and Stead (2010)

In the following chapters, a Grain-Based Model (GBM) is developed using a continuum numerical program, and calibrated to the properties of Wombeyan marble. The GBM of heat-treated Wombeyan marble is upscaled and then used to investigate the strength of highly interlocked jointed rib pillar as a function of the pillar W/H ratio. The PSC obtained from this study will then be compared to those of jointed pillars reviewed in this chapter (i.e., Figure 2-33).

CHAPTER 3 A CONTINUUM GRAIN-BASED MODEL FOR INTACT AND GRANULATED WOMBEYAN MARBLE[1]

3.1. INTRODUCTION

The design of surface and underground excavations in jointed rock masses requires the knowledge of the mechanical properties of the rock at different scales (i.e., laboratory specimen, rock block, and rock mass), which are influenced by the presence of heterogeneities (Laubscher & Jakubec, 2001). Hence, it is important to understand how and to what extent heterogeneities affect rock behavior and its properties at different scales. At the laboratory specimen scale, heterogeneity is represented by the complex microstructure, pre-existing micro-cracks, various mineral grains, and small veins and fractures. At the rock block scale, heterogeneity can be found in the form of veins and cemented joints. At the rock mass scale, heterogeneity is in the form of discontinuities of various lengths, orientations, and levels of persistence, as well as rock blocks of various geometries.

It is known that micro-cracking and fracturing processes leading to the failure of brittle rocks are controlled by the presence of heterogeneity. Heterogeneity results in the concentration of tensile stresses inside a rock medium even under an overall compressive loading condition. Local tensile stresses may lead to the development of tensile cracks when the magnitude of tensile stress exceeds the local tensile strength of the rock. According to Lan et al. (2010), grain-scale heterogeneities can be divided into three main types: 1) grain geometric heterogeneity, which results from different shapes (i.e., angularities and sphericities) and sizes of mineral grains; 2) grain property heterogeneity, which arises from the variation in strength and deformation properties of different mineral grains; and 3) grain contact heterogeneity due to the anisotropy of grain boundary distributions (i.e., length, orientation, and properties).

[1] A version of this chapter was published in *Computers and Geotechnics*: Li, Y and Bahrani, N. 2021. A continuum Grain-Based Model for Intact and Granulated Wombeyan marble. *Computers and Geotechnics*, 129, 103872.

Numerical modeling is a powerful tool that has been used to investigate the influence of heterogeneity on the failure process and strength of brittle rocks. Three numerical methods typically used to study the mechanical behavior of rock-like materials are continuum, discontinuum, and hybrid continuum-discontinuum methods (Hoek et al., 1991; Jing & Hudson, 2002; Lisjak & Grasselli, 2014). With recent advances in computational power and software programs, it is now possible to incorporate grain-scale heterogeneities into numerical analyses. As an example, the Discrete Fracture Network (DFN) models (Elmo & Stead, 2010; Ivars et al., 2011) implemented in different numerical modeling programs can be used to generate polygonal cells based on the Voronoi tessellation technique (Dershowitz, 1985), and simulate the microstructure of brittle rocks. This approach, called the grain-based model (GBM), allows for simulating pre- and post-peak fracturing processes of brittle rocks under various loading conditions (Lan et al., 2010). The GBM has been implemented in commercial discontinuum and combined continuum-discontinuum programs to reproduce the laboratory behavior of brittle rocks (e.g., Kazerani & Zhao, 2010; Lan et al., 2010; Bahrani et al., 2014; Ghazvinian et al., 2014; Gao et al., 2016; Abdelaziz et al., 2018; Liu et al., 2018; Wang & Cai, 2018; Sinha & Walton, 2020). However, to the author's knowledge, no attempt has been made to use continuum numerical programs (e.g., finite element method) to systematically calibrate a GBM to the laboratory properties of a brittle rock.

Various types of heterogeneities have been simulated using commercial continuum numerical programs. Valley et al. (2010) and Bewick et al. (2012) investigated the influences of grain stiffness and grain geometric heterogeneities on the grain-scale stress path and the formation of tensile stresses in a laboratory-scale specimen using the finite element program *Phase2* (former version of RS2; Rocscience, 2019). Valley et al. (2010) developed a heterogeneous model by assigning different stiffness values to the mesh elements (i.e., stiffness heterogeneity). They found that stiffness heterogeneity alone is sufficient to generate tensile cracks before the peak stress. However, the strength envelope of this model was found to be linear. Furthermore, the known transition in the failure mode (i.e., axial splitting at low confinement and shear failure at high confinement) could not be captured by this heterogeneous continuum model. Bewick et al. (2012) developed a continuum Voronoi tessellated model in *Phase2* and investigated the influence of grain

geometric heterogeneity on the tensile stresses generated within a specimen under compression. From the results of elastic models, they concluded that grain boundary orientation and grain system arrangement control the generation of tensile stresses inside a brittle rock specimen (Bewick et al., 2012).

The continuum Voronoi tessellated model has also been used to simulate heterogeneities at the rock mass scale (Kaiser et al., 2016; Day et al., 2019). Kaiser et al. (2016) simulated a jointed rock mass using a Voronoi tessellated model in *Phase2* to investigate the influence of large-scale heterogeneities on the variation of in-situ stress magnitudes with depth. They concluded that the observed stress variability in the Canadian shield can be attributed to rock mass geometric and property heterogeneities. Day et al. (2019) combined the Voronoi tessellated blocks and parallel joint sets to explicitly simulate the veins and block forming joints, respectively, near mine drifts. They demonstrated how inter- and intra-block structures control the rock mass behavior (i.e., both displacement and failure mode) around underground openings.

The numerical simulations reviewed above demonstrate the influence of heterogeneities on rock behavior at different scales. However, the applicability of the continuum-based Voronoi tessellated model (or continuum GBM) for simulating brittle rock failure should be first investigated by calibrating the model to the results of controlled laboratory tests, and then extended to rock mass scale problems. In this chapter, the laboratory behavior of Wombeyan marble is simulated using a continuum GBM developed in *RS2* (Rocscience, 2019) (called RS2-GBM). The laboratory triaxial test results of intact and heat-treated Wombeyan marble are used for numerical simulation and model calibration. The central objective of this chapter is to evaluate whether RS2-GBM can be used to capture some of the most important characteristics of brittle rocks, including the non-linear strength envelope and the observed post-peak response and failure mode at various levels of confinement.

3.2. BACKGROUND

The laboratory behavior of intact coarse-grained Wombeyan marble, from a quarry near Wombeyan in New South Wales, Australia, was studied by Paterson (1958), Rosengren

and Jaeger (1968), Gerogiannopoulos (1976), and Gerogiannopoulos and Brown (1978) under unconfined and confined compressive loading conditions. Gerogiannopoulos (1976) and Paterson (1958) observed a typical post-peak response of brittle rocks in the stress-strain curves of intact marble, changing from brittle behavior at low confinement (i.e., σ_3 = 0 - 3.5 MPa), to strain-softening with increasing confinement (i.e., σ_3 = 10 - 21 MPa), to perfectly plastic at high confinement (i.e., σ_3 = 28 - 46 MPa), and to strain-hardening at extremely high confinement (i.e., σ_3 = 70 - 100 MPa), as shown in Figure 3-1a and b. Note that the stress-strain curves in Figure 3-1a show some variations in the values of Young's modulus for intact marble at different levels of confinement; the Young's modulus tends to increase with increasing confinement. This is interpreted to be due to the presence of pre-existing micro-cracks in the specimens.

Rosengren and Jaeger (1968) and Gerogiannopoulos (1976) also conducted unconfined and confined compression tests on heat-treated Wombeyan marble. In this case, the intact marble specimens were heated up to 600℃. This resulted in the separation of mineral grains (mostly calcite) at the grain boundaries due to the anisotropy of the thermal expansion of calcite grains. The tensile strength of granulated marble was determined to be nearly zero (i.e., 0.03 MPa) from the direct tensile tests (Rosengren and Jaeger, 1968). Rosengren and Jaeger (1968) used the term 'granulated' to refer to the heat-treated marble. According to Rosengren and Jaeger (1968), the granulated marble can be regarded as a model of a randomly jointed rock mass, while Bahrani and Kaiser (2013) suggested that it can be served as an analogue for a highly interlocked jointed rock mass.

Figure 3-1c and d present the stress-strain curves of granulated Wombeyan marble reported by Gerogiannopoulos (1976) and Rosengren and Jaeger (1968), respectively. As can be seen in these figures, the elastic modulus systematically increases as confinement increases. The stress-strain curves of granulated marble are highly non-linear in their initial loading stages, and the degree of non-linearity decreases as the confining pressure increases. Note that the stress-strain curves from the tests by Rosengren and Jaeger (1968) in Figure 3-1d show a higher degree of non-linearity than those by Gerogiannopoulos (1976) in Figure 3-1c. According to Hoek and Martin (2014) and Peng et al. (2015), the non-linearity of the stress-strain curves in brittle rocks is due to the closure of pre-existing micro-cracks. In the

granulated marble specimens, the grains are separated and open at their boundaries due to heating. Therefore, the non-linearity of the stress-strain curves is the result of the closure of open grain boundaries. The granulated marble exhibits a strain-softening behavior for a wide range of confinement (i.e., σ_3 = 0 - 20 MPa) and only becomes perfectly plastic at high confining pressures (i.e., σ_3 > 20 MPa).

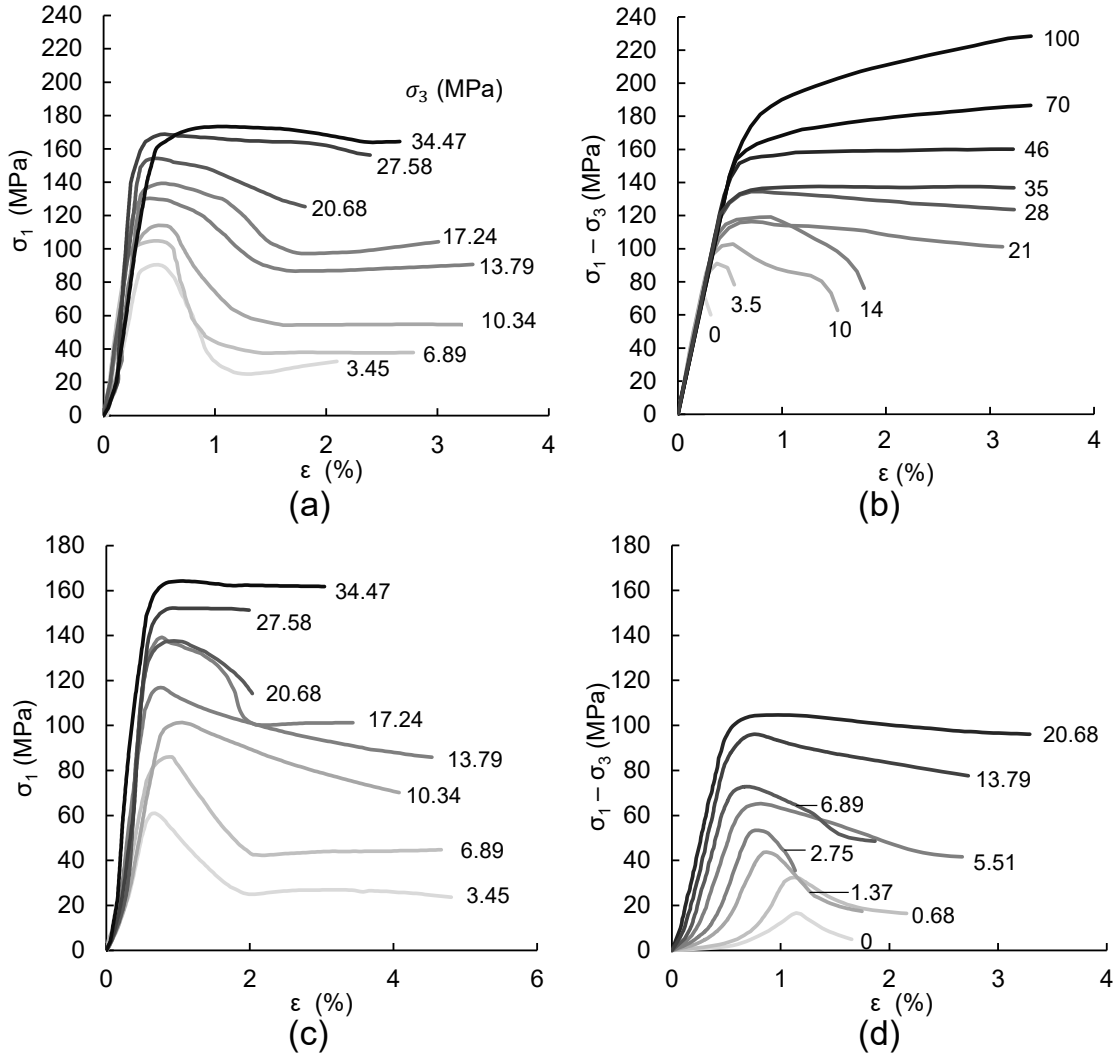

Figure 3-1: Stress-strain curves obtained from laboratory triaxial tests on Wombeyan marble: a) intact marble by Gerogiannopoulos (1976); b) intact marble by Paterson (1958); c) granulated marble by Gerogiannopoulos (1976); and d) granulated marble by Rosengren and Jaeger 1968).

The unconfined and confined peak strengths of both intact and granulated Wombeyan marble are presented in Figure 3-2. It can be seen from this figure that the Unconfined Compressive Strength (UCS) of granulated marble is less than a third of its intact UCS. However, the strength of granulated marble increases more rapidly than the intact strength

as the confining pressure increases until it approaches about 80% of the intact strength at a confining pressure of about 10 MPa.

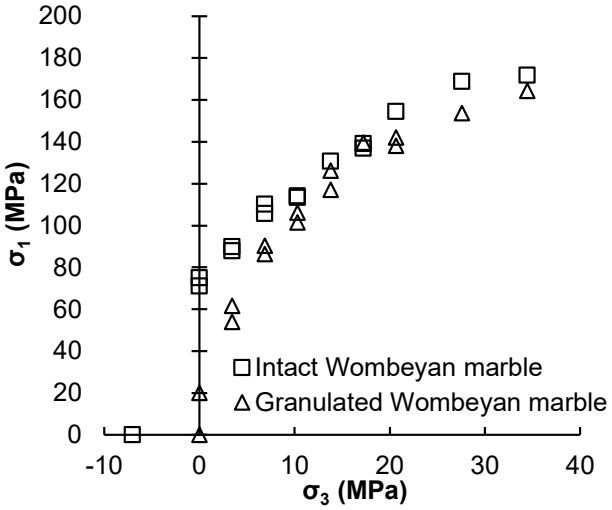

Figure 3-2: Laboratory triaxial test results of intact and granulated Wombeyan marble (after Gerogiannopoulos, 1976).

The laboratory behavior of intact and granulated Wombeyan marble was simulated by Bahrani et al. (2011, 2014) using a GBM in *PFC* (Itasca Consulting Group, 2008), which is a numerical program based on the Distinct Element Method (DEM). As shown in Figure 3-3a, in PFC-GBM, each grain consists of a number of circular particles bonded together at their contact points using the parallel bond logic (Potyondy & Cundall, 2004). The grain boundaries are represented by smooth-joint contacts (Potyondy, 2010). A comparison between the strengths of the calibrated PFC-GBMs and those of intact and granulated Wombeyan marble is shown in Figure 3-3b.

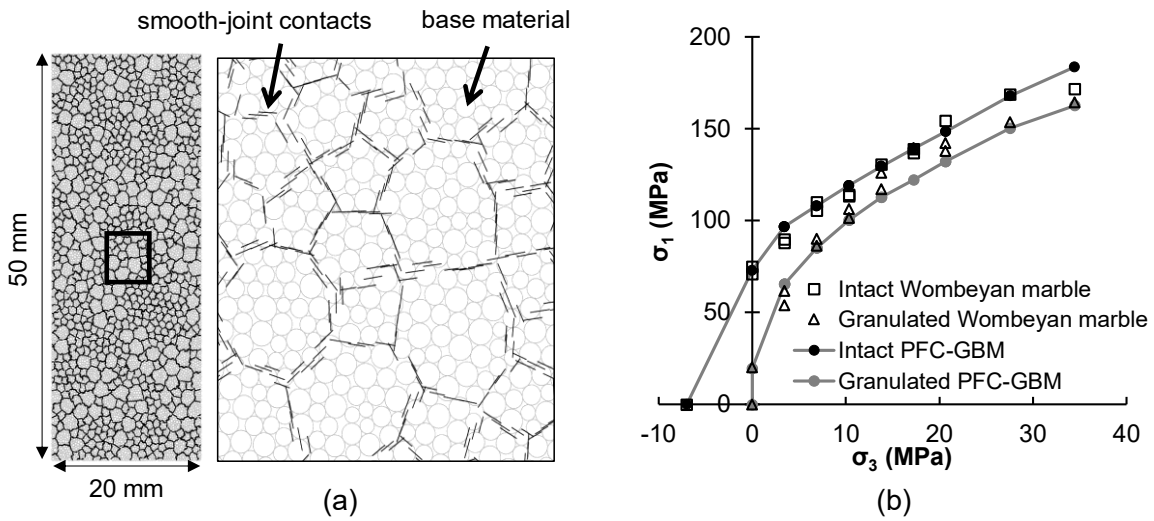

Figure 3-3: a) Grain structure of PFC-GBM; b) comparison between unconfined and confined strengths obtained from laboratory tests and calibrated PFC-GBMs of intact and granulated marble (after Bahrani et al., 2014).

In the following sections, the finite element program *RS2* (Rocscience, 2019) is used to reproduce the laboratory behavior of intact and granulated Wombeyan marble, following the methodology proposed by Bahrani et al. (2014). First, the procedure to construct a GBM in *RS2* and its calibration to the strength of Wombeyan marble are presented. Then, elastic analyses are conducted to better understand the influence of grain-scale heterogeneities on the evolution of stresses inside the specimen during compressive loading. Next, the results of triaxial tests simulated on inelastic RS2-GBMs including the stress-strain curves and failure modes are presented and compared with those of PFC-GBMs reported by Bahrani et al. (2014).

3.3. GRAIN-BASED MODEL OF WOMBEYAN MARBLE

3.3.1. Discrete Fracture Network in RS2

The built-in DFN generator in *RS2* can be used to construct different types of joint network, including the parallel joint set, cross joint set (i.e., bedding planes with short cross joints), Baecher (Baecher et al., 1977), Veneziano (Dershowitz, 1985), and Voronoi (Dershowitz, 1985; Dershowitz & Einstein, 1988). In *RS2*, the Voronoi joint network can be employed to subdivide a homogeneous finite element model into non-overlapping convex polygons (i.e., Voronoi cells) to generate a GBM simulating the microstructure of crystalline rocks,

as shown in Figure 3-4. The Voronoi joint network can be categorized into different polygonal shapes based on their regularities, including irregular polygons (Figure 3-4a), medium regular polygons (Figure 3-4b), almost regular polygons (Figure 3-4c), and regular hexagons (Figure 3-4d and e). The cell density can be assigned either by the number of cells per area or the average length of the cell boundary. Different constitutive models can be assigned to the cells or finite elements (e.g., Mohr-Coulomb, Hoek-Brown, etc.).

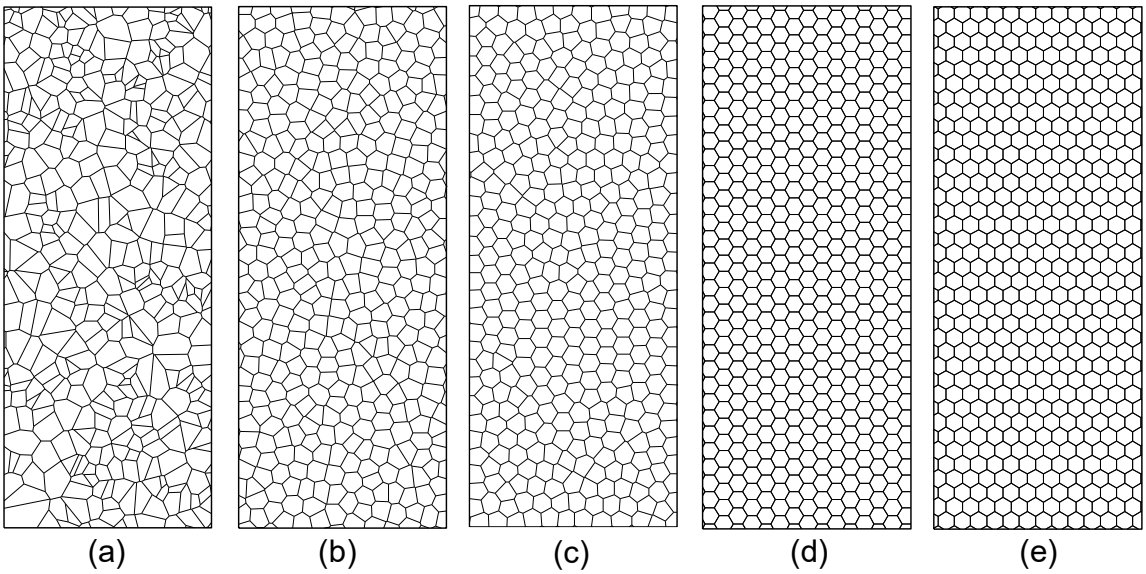

Figure 3-4: Voronoi joint networks in RS2: a) irregular polygon; b) medium regular polygon; c) almost regular polygon; d) regular hexagon in horizontal orientation; and e) regular hexagon in vertical orientation.

In the Voronoi tessellated model (or GBM), the contact between two grains representing the grain boundary is an open-ended joint element (also called finite element interface; Ghabaussi et al., 1973; Goodman et al., 1968). The joint element is a one-dimensional four-noded quadrilateral element with a negligible thickness (Riahi et al., 2010). It is an edge-to-edge contact in which interconnectivity does not change with time. Figure 3-5 presents the configurations of a joint element before and after deformation. As can be seen in this figure, the two sides of the joint element have equal lengths. Before deformation occurs (Figure 3-5a), nodes 1 and 4 of the joint element share the same position, while nodes 2 and 3 share another position. When the blocks start to deform (Figure 3-5b), the nodes can move normally and tangentially from each other. According to Riahi et al. (2010), large displacement, rotation, or strains of discrete objects can be accommodated by the joint element so long as these mechanisms do not change contacting node couples.

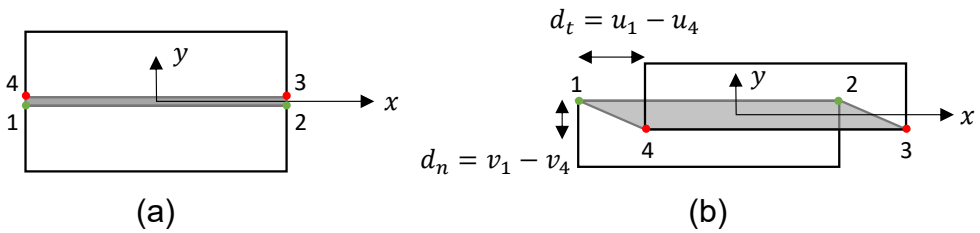

Figure 3-5: Interpretation of Goodman finite element interface (joint element) in RS2 (after Riahi et al., 2010): a) undeformed joint element; and b) deformed joint element.

The joint elements in *RS2* are assigned strength and stiffness properties. Relative movement of the two sides of a joint may be elastic or inelastic. Inelastic joints with perfectly plastic or brittle post-peak response can be simulated by assigning a failure criterion (e.g., Mohr-Coulomb, Barton-Bandis, etc.) and appropriate residual strength properties, to allow for shear (slip) or tensile yielding between the two discrete bodies. The residual strength parameters will be in effect if joint slip or tensile yielding occurs (i.e., peak strength envelope is exceeded). For example, in the case of the Mohr-Coulomb failure criterion, if the shear stress on a joint element exceeds the joint peak shear strength, slip (or shear yielding) occurs, and the cohesion and friction angle of the joint element are reduced to their residual values. Similarly, if the normal stress on a joint element exceeds the joint peak tensile strength, tensile yielding occurs, and the tensile strength of the joint element is reduced to its residual value.

3.3.2. RS2-GBM of Wombeyan Marble

A 20 mm × 50 mm GBM was constructed in *RS2* (v.10.08) to represent a Wombeyan marble specimen (Figure 3-6). The chemical analyses conducted by Paterson (1958) showed that the mineralogical composition of Wombeyan marble is mainly calcite (i.e., 96% of $CaCO_3$). Therefore, only one mineral type representing calcite grains was considered in this simulation.

Bewick et al. (2012) pointed out that the distribution of grain boundary orientation in the GBM with regular hexagon grain structures (i.e., Figure 3-4d and e) is not uniform, and this results in a non-uniform tensile stress distribution along the grain boundaries. Their analyses showed that the distributions of grain boundary orientation for other polygon

shapes (i.e., irregular, medium, and almost irregular) are uniform. Hence, these models (Figure 3-4a, b and c) have similar tensile stress distributions along the grain boundaries during uniaxial loading (Bewick et al., 2012). A series of sensitivity analyses were conducted to investigate the influence of grain geometry on the UCS of the GBM. It was found that as long as the numbers of mesh elements in the GBMs with irregular, medium regular, and almost regular cells are close, the difference between the strength of these models is negligible (i.e., within ± 3 MPa of the UCS of intact marble). Such difference is not significant compared to the average UCS of intact marble specimens, which is 74.5 MPa. Therefore, in this study, the Voronoi tessellated model with medium regular cells (Figure 3-6a) was selected to generate the RS2-GBM and represent the grain structure of Wombeyan marble (compare Figure 3-6b and Figure 3-6c).

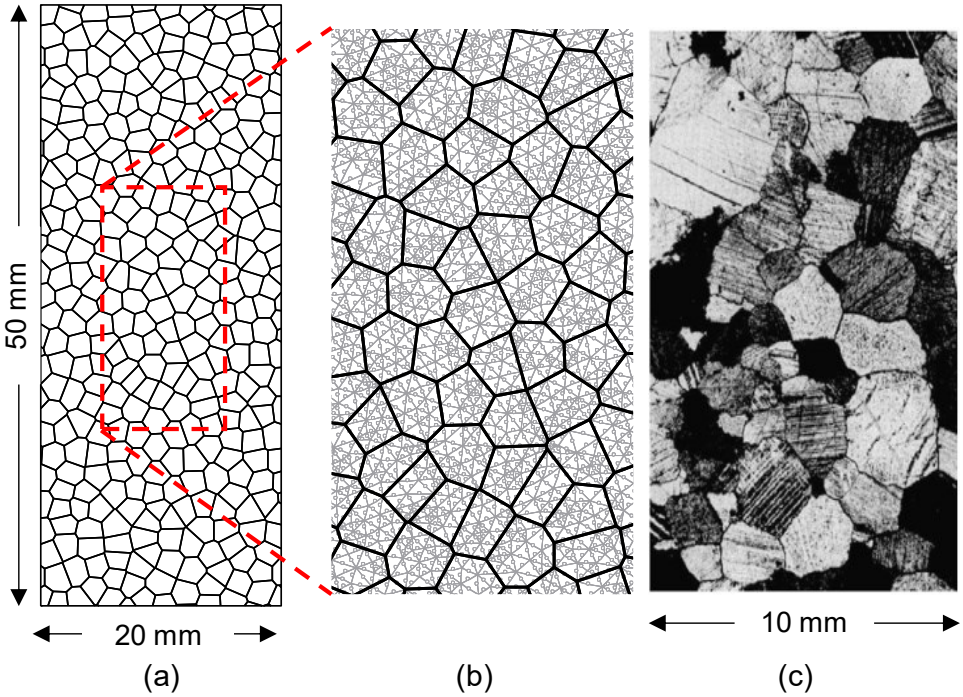

Figure 3-6: a) Geometry of RS2-GBM of Wombeyan marble and its boundary conditions for UCS test simulation; b) closer view of GBM showing grain structure and mesh elements, and comparison with: c) grain structure of Wombeyan marble (Rosengren & Jaeger, 1968).

According to Rosengren and Jaeger (1968) and Gerogiannopoulos (1976), the average grain size of Wombeyan marble is between 1 and 2 mm. In the RS2-GBM of Wombeyan marble, the average length of the contact between two grains (i.e., grain boundary) is 0.9 mm. This setting resulted in at least 10 grains across the specimen's width, which is

consistent with the suggestion by the ISRM (Bieniawski & Bernede, 1979; see Figure 3-6a). This means that the average grain size of the RS2-GBM is about 2 mm, which is consistent with that of PFC-GBM by Bahrani et al. (2014).

Six-noded uniform triangular elements were used to mesh the grains (Figure 3-6b). The results of sensitivity analyses conducted on mesh density indicated that the strength of RS2-GBM decreased with increasing the mesh density and became constant when the total number of mesh elements was greater than 11,000. Therefore, to minimize the influence of mesh size on modeling results, the total number of mesh elements in the five realizations of RS2-GBM was selected to be more than 11,000 (i.e., between 12,000 and 13,000 which resulted in a density of 25 to 27 finite elements per grain).

In the simulations of unconfined and confined compression tests, the lower boundary of the model was fixed in vertical direction except for its midpoint, which was fixed in both vertical and horizontal directions (Figure 3-7). A displacement boundary was directly applied to the top boundary of the numerical specimen to simulate the UCS test (Figure 3-7a). In the simulation of confined tests, a distributed load was applied to three boundaries of the numerical specimen at the first loading stage, as shown in Figure 3-7b (left). Starting from the second loading stage, a displacement boundary was applied to the top boundary of the numerical specimen, while the distributed load at the two sides was kept constant, simulating a constant confining pressure, as shown in Figure 3-7b (right). The GBM was loaded with a strain rate of 0.0001 per stage (i.e., displacement rate of 0.005 mm/stage). The selected strain rate was reduced near the peak stage to be able to accurately capture the peak strength.

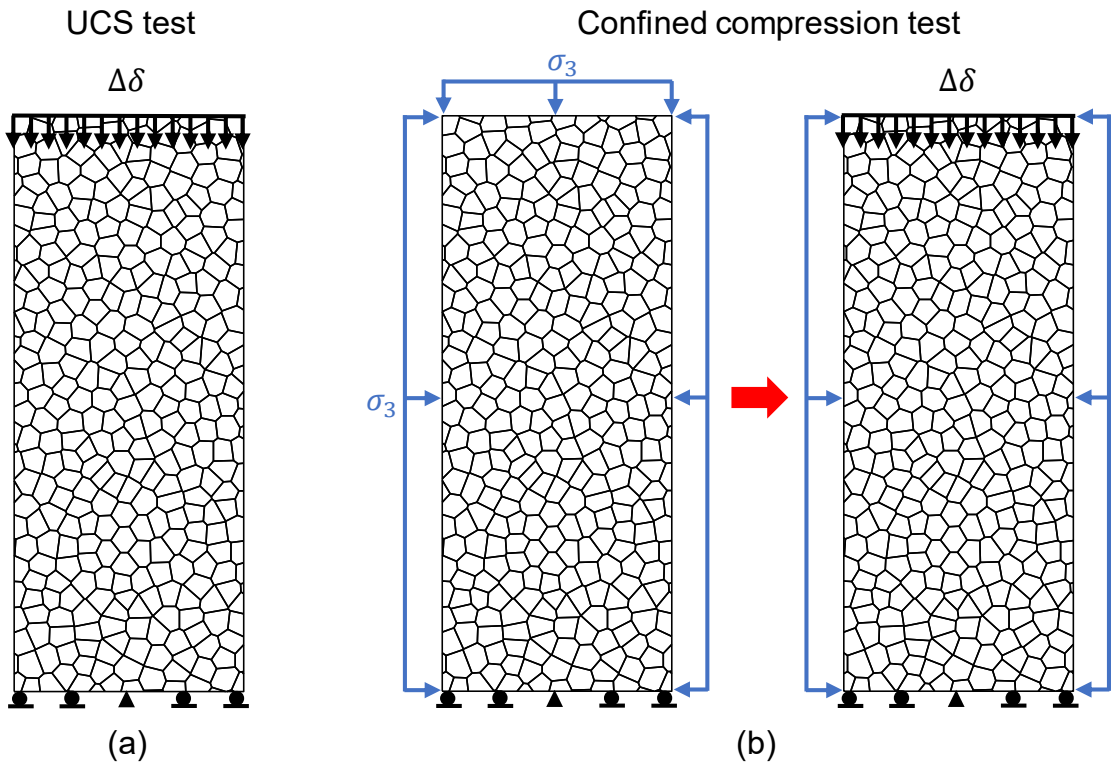

Figure 3-7: RS2-GBM boundary conditions in: a) unconfined compression test; and b) confined compression test, showing the boundary conditions at the first loading stage (left) and the rest of stages (right).

3.3.3. Calibration Assumptions

The goal of the RS2-GBM calibration was to match its macro-properties to the laboratory properties of intact and granulated Wombeyan marble, including the unconfined and confined compressive strengths and the elastic modulus. The simulation results, such as the stress-strain curves and failure modes, are compared to those of laboratory tests (Gerogiannopoulos, 1976; Paterson, 1958) and PFC-GBM (Bahrani et al., 2014) in Section 3.5. The calibration of RS2-GBM to the laboratory properties of Wombeyan marble required adjusting the following micro-properties, including those of grains and grain boundaries:

- Properties of grains:
  (a) Peak and residual tensile strength (σ_{tgp} and σ_{tgr});
  (b) Peak and residual cohesion (c_{gp} and c_{gr});
  (c) Peak and residual friction angle (φ_{gp} and φ_{gr});

(d) Young's modulus (E_g);

(e) Poisson's ratio (v_g).

- Properties of grain boundaries (i.e., joints):

(a) Peak and residual tensile strength (σ_{tbp} and σ_{tbr});

(b) Peak and residual cohesion (c_{bp} and c_{br});

(c) Peak and residual friction angle (φ_{bp} and φ_{br});

(d) Shear stiffness and normal stiffness (k_s and k_n).

Therefore, thirty-two unknown individual input parameters were required for the calibration RS2-GBM (i.e., 16 for intact and 16 for granulated marble). In order to reduce the complexity of the calibration process, some assumptions were made to decrease the number of unknown micro-parameters. The calibration assumptions are consistent with those used by Bahrani et al. (2014) for the calibration of PFC-GBM, as described below:

Assumption 1: The heating process reduced the grain boundary cohesion (c_{bp}) and tensile strength (σ_{tbp}) to nearly zero. Therefore, grain boundary cohesion and tensile strength of 0.1 MPa (as opposed to 0 MPa) were used in the RS2-GBM of granulated marble to avoid convergence error (see Figure 3-8a).

Assumption 2: The heating process did not affect the frictional strength of the grain boundaries. In other words, the heating process only destroyed the cohesive bond between the grains but did not affect the basic friction angle and the roughness of the grain boundaries. Therefore, the peak friction angles of the grain boundaries (φ_{bp}) in the GBMs of intact and granulated marble were assumed to be equal (Figure 3-8a).

Assumption 3: The heating process did not affect the grain properties. Hence, the grain strength and deformation properties in the GBMs of intact and granulated marble were assumed to be the same (Figure 3-8b).

Assumption 4: Grain tensile failure was assumed to reduce the grain shear strength to residual in the GBMs of intact and granulated marble (Figure 3-8b). This means that if an element within a grain yielded in tension, the shear strength (and the tensile strength) of this element was dropped to its residual value (i.e., c_{gr} = 15 MPa and φ_{gr} = 37°).

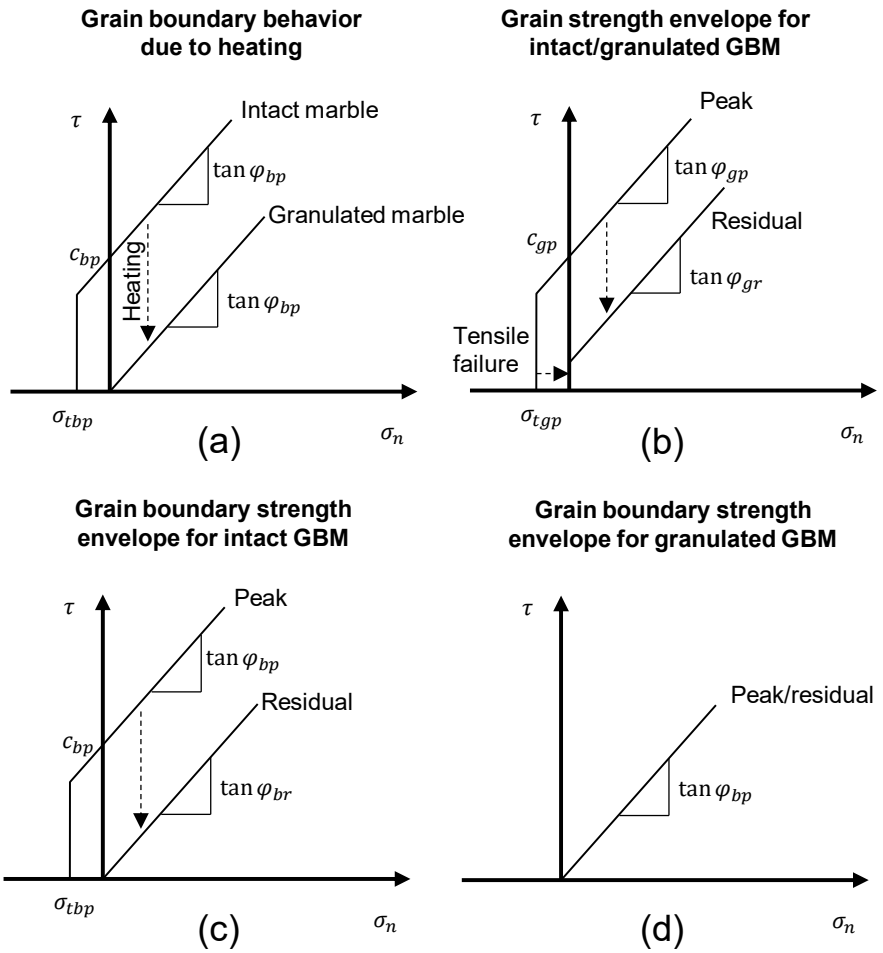

Figure 3-8: Assumptions in RS2-GBM calibration: a) Reduction of grain boundary strength after heating; b) grain peak and residual strength envelopes for GBMs of intact and granulated marble; c) grain boundary peak and residual strength envelopes for GBM of intact marble; and d) grain boundary peak and residual strength envelopes for GBM of granulated marble.

Assumption 5: Grain boundary failure was assumed to reduce the grain boundary shear and tensile strengths to residual in the GBM of intact marble (Figure 3-8c). The residual grain boundary tensile strength (σ_{tbr}) and cohesion (c_{br}) were assumed to be 0.1 MPa.

Assumption 6: The peak and residual friction angles of the grain boundaries (φ_{bp} and φ_{br}) were assumed to be the same in the GBMs of intact and granulated marble (Figure 3-8c and d).

Assumption 7: The ratio of grain boundary normal to shear stiffness (k_n/k_s) was assumed to be 10.

Assumption 8: The Young's modulus of the grains was summed to be 80 GPa to be consistent with the results of laboratory tests conducted on calcite grains (Belikov, 1967; Broz et al., 2006).

The assumptions summarized above significantly simplified the model calibration process by reducing the number of unknown input parameters from 32 to 9. The details of the calibration process are discussed next.

3.3.4. Model Calibration

An iterative calibration process similar to that proposed by Bahrani et al. (2014) was used to match the macro-properties of RS2-GBM to those of intact and granulated Wombeyan marble. As shown in Figure 3-9, the simulations started by calibrating the GBM to the properties of granulated marble, and then continued by calibrating the GBM to the properties of intact marble.

Model calibration to granulated marble: First, the GBM was calibrated to the Young's modulus of granulated marble by adjusting the stiffness parameters of the grain boundaries, assuming that the Young's modulus of the calcite grain is 80 GPa based on *Assumption 8*. Then, the unconfined and confined strengths were matched by adjusting the grain strength properties and the grain boundary friction angle. During the calibration, it was found that the grain shear strength parameters control the strength of the GBM at high confinement (i.e., σ_3 = 10.34 – 34.47 MPa), and the grain boundary friction angle controls the strength of the GBM at low confinement (i.e., σ_3 = 0 – 10.34 MPa).

Model calibration to intact marble: Once the GBM of granulated marble was calibrated, its grain strength and stiffness properties and grain boundary friction angle were directly used in the GBM of intact marble, following *Assumption 3*. At this stage, the Young's modulus of the GBM was matched by adjusting the grain boundary stiffness parameters. Then, the strengths of the GBM were matched to the laboratory test results by adjusting the grain boundary tensile strength and cohesion.

The calibration process explained above was iterated until the macro-properties of both GBMs matched the laboratory properties of intact and granulated Wombeyan marble. Note that no attempt was made to match the Poisson's ratio of the GBM to that of Wombeyan marble due to the lack of laboratory test data. It is concluded that the grain and grain boundary tensile strengths control the UCS and the grain and grain boundary shear strengths control the confined strength of the GBM.

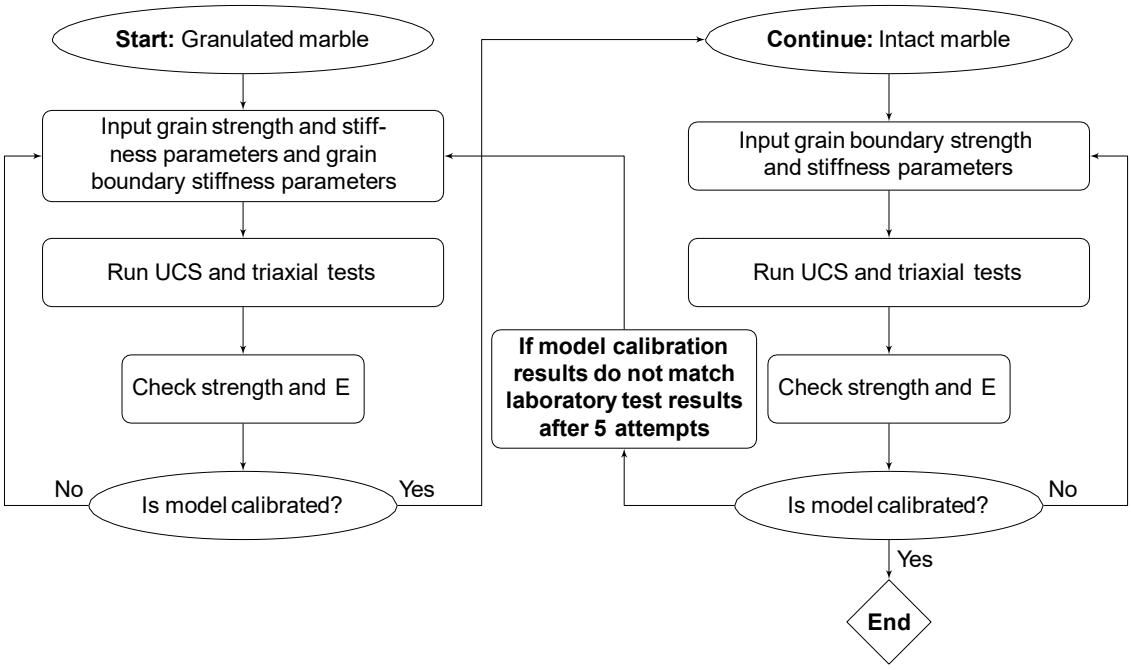

Figure 3-9: Procedure for calibrating the RS2-GBMs to laboratory properties of intact and granulated Wombeyan marble.

In this study, five realizations for the grain structure (i.e., five Voronoi joint networks) were generated with a single combination of micro-properties to obtain a range for the macro-properties. The average values of the macro-properties were then used for comparison with the laboratory test results and calibration of the GBM.

3.3.5. Calibration Results

The grain and grain boundary properties for the calibrated GBMs of intact and granulated marble are provided in Table 3-1 and Table 3-2, respectively. Note that the grain properties in the GBMs of intact and granulated marble are the same (see Table 3-1). In Table 3-2, the stiffness values of the grain boundaries (i.e., k_n and k_s) for granulated marble are four

times lower than those for intact marble. According to Rosengren and Jaeger (1968) and Gerogiannopoulos (1976), the heating process resulted in an increase in the volume of granulated marble specimens due to opening of the grain boundary cracks. Therefore, the stiffness parameters of the grain boundaries in the GBM of granulated marble were assumed to be lower than those of the GBM of intact marble. Note that no initial assumption was made for the stiffness values of the grain boundaries in the GBMs of intact and granulated marble, and they were obtained through the calibration process described in the previous section.

Table 3-1: Grain properties of calibrated RS2-GBM.

GBM	Grain properties (peak / residual)			
	c_{gp}/c_{gr} (MPa)	φ_{gp} / φ_{gr} (°)	σ_{tgp} / σ_{tgr} (MPa)	E_g (GPa)
Intact	45 / 15	37 / 37	14 / 0.1	80
Granulated	45 / 15	37 / 37	14 / 0.1	80

Table 3-2: Grain boundary properties of calibrated RS2-GBM.

GBM	Grain boundary properties (peak / residual)				
	c_{bp} / c_{br} (MPa)	φ_{bp} / φ_{br} (°)	σ_{tbp} / σ_{tbr} (MPa)	k_n (GPa/m)	k_s (GPa/m)
Intact	40 / 0.1	50	3 / 0.1	240,000	24,000
Granulated	0.1 / 0.1	50	0.1 / 0.1	60,000	6,000

The unconfined and confined strengths for five model realizations of intact and granulated marble are provided in Table 3-3 and Table 3-4, respectively. The percentage errors in these tables were calculated based on the average strength of all model realizations and the average laboratory test results reported by Gerogiannopoulos (1976). It can be seen in these tables that the calculated errors are less than 10% for most confining pressures, except for σ_3 = 3.45 MPa in the GBM of intact marble, and σ_3 = 3.45 and 17.24 MPa in the GBM of granulated marble.

Table 3-3: Unconfined and confined strengths of RS2-GBMs of intact marble and calculated percentage errors.

σ_3 (MPa)	Realizations					Average	% Error
	No. 1	No. 2	No. 3	No. 4	No. 5		
0	74.2	77.1	73.1	77.7	70.4	74.5	2.1
3.45	101.2	100.3	97.4	99.6	100.6	99.8	12.4
6.89	111.0	111.0	109.8	110.6	113.1	111.1	3.1
10.34	117.7	119.9	117.6	117.5	118.7	118.3	4.0
13.79	127.6	127.3	125.1	127.5	126.9	126.9	2.8
17.24	136.1	134.6	132.8	136.6	135.4	135.1	2.0
20.68	145.0	141.8	142.0	143.8	144.1	143.4	7.1
27.58	161.8	161.1	160.6	162.8	160.7	161.4	4.3
34.47	181.1	181.1	180.1	182.7	180.1	181.0	5.4

Table 3-4: Unconfined and confined strengths of RS2-GBMs of granulated marble and calculated percentage errors.

σ_3 (MPa)	Realizations					Average	% Error
	No. 1	No. 2	No. 3	No. 4	No. 5		
0	19.3	22.8	22.1	26.0	18.8	21.8	9.0
3.45	67.3	71.4	66.0	68.1	67.0	68.0	17.6
6.89	88.6	92.2	88.5	92.0	89.9	90.2	2.2
10.34	104.9	104.7	101.2	105.2	102.5	103.7	0.1
13.79	114.1	114.2	113.1	115.0	114.6	114.2	6.1
17.24	123.9	123.7	122.8	124.7	125.2	124.1	11.1
20.68	132.2	133.0	132.2	135.5	133.2	133.2	4.8
27.58	152.7	151.7	151.6	153.7	154.7	152.9	0.5
34.47	173.0	171.8	170.9	174.1	173.1	172.6	5.0

As discussed by Bahrani et al. (2014), Tatone and Grasselli (2015), Abdelaziz et al. (2018), and Sinha and Walton (2020), and demonstrated by Bahrani and Hadjigeorgiou (2018), when the number of unknown parameters (i.e., micro-properties) in a discontinuum model is more than the number of known parameters (i.e., target macro-properties), the solution (i.e., micro-properties of the calibrated model) is indeterminate. This means that multiple combinations of input parameters can lead to equivalently well-calibrated models. Therefore, the micro-properties listed in Table 3-1 and Table 3-2 represent one solution (i.e., a combination of micro-properties) that is qualitatively equivalent to other possible

solutions. An example of how two calibrated models with different sets of input parameters could lead to comparable results in terms of failure mode and rock deformation are provided by Bahrani and Hadjigeorgiou (2018). Further research on how the choice of input parameters (i.e., micro-properties) on modeling results (i.e., stress redistribution and failure mode) at both micro- and macro-scales is suggested.

Figure 3-10 presents the unconfined and confined strengths for calibrated GBMs of intact and granulated marble. In general, the strengths of both intact and granulated Wombeyan marble are well-captured by the RS2-GBMs for the full range of confinement, as the results are consistent with those of laboratory tests by Gerogiannopoulos (1976) (Figure 3-10a) and PFC-GBMs by Bahrani et al. (2014) (Figure 3-10b). It can be seen in these figures that the non-linearity of the strength envelopes for both intact and granulated marble is well captured by the calibrated RS2-GBMs, although a linear Mohr-Coulomb criterion was used for both grains and grain boundaries.

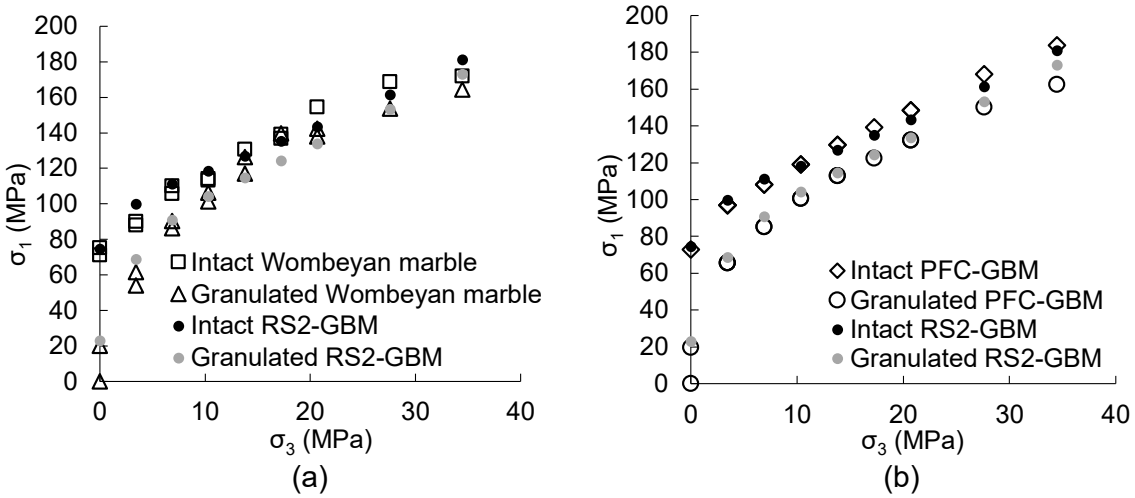

Figure 3-10: Comparison between the peak strengths of calibrated RS2-GBMs and: a) laboratory tests by Gerogiannopoulos (1976); b) PFC-GBMs by Bahrani et al. (2014).

Figure 3-11 shows how the Young's modulus of granulated Wombeyan marble increases with increasing confinement. The RS2-GBM overestimates the Young's modulus of granulated marble at low confinement (i.e., σ_3 = 0 – 13.79 MPa). This is due to fact that the opening of the grains at their boundaries caused by heating was not explicitly simulated, and therefore their closures during compressive loading were not captured by the RS2-GBM. This was also the case in the PFC-GBMs by Bahrani et al. (2014). Figure 3-11

confirms that the elastic modulus of the RS2-GBM of granulated marble matches both the laboratory test (Gerogiannopoulos, 1976) and PFC simulation results (Bahrani et al., 2014) at high confinement (i.e., σ_3 > 17 MPa). Note that pre-existing cracks were not simulated in the GBM of intact marble. For this reason, the Young's modulus of the calibrated RS2-GBM of intact marble was found to be independent of the confining pressure (i.e., about 61 GPa at all confining pressures).

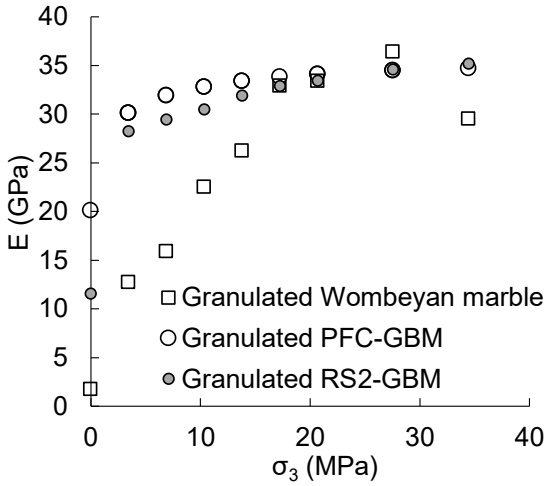

Figure 3-11: Confined elastic modulus of RS2-GBM of granulated marble compared to the results of PFC-GBM by Bahrani et al. (2014) and laboratory tests by Gerogiannopoulos (1976).

As demonstrated in this section, the RS2-GBM is capable of reproducing the laboratory behavior of intact and granulated Wombeyan marble, in terms of the peak strength for the full range of confinement and the Young's modulus at high confinement (i.e., σ_3 > 17 MPa). In the next section, elastic RS2-GBMs are used to investigate the evolution of grain-scale stresses and the development of tensile stresses inside the grains and along the grain boundaries during compressive loading.

3.4. GRAIN-SCALE STRESS PATH

Elastic RS2-GBMs of intact marble were used to investigate the influence of grain-scale heterogeneity on the evolution of grain and grain boundary stresses at different levels of confinement. For this purpose, the grain node stresses (i.e., major and minor principal stresses on each node inside the grains) and the grain boundary normal stresses were

analyzed to better understand the tensile stresses generated within the grains and along the grain boundaries, respectively, during compressive loading.

3.4.1. Unconfined Compression

Figure 3-12 illustrates the grain node stresses and grain boundary normal stresses at 35%, 75%, and 100% of the peak stress (i.e., UCS) for the elastic GBM of intact marble. In Figure 3-12a, c, and e, the grain node stresses are plotted in σ_1-σ_3 space, and the average stress is indicated by the black cross. In these figures, the black dashed line divides the compression ($\sigma_3 > 0$ MPa) and tension ($\sigma_3 < 0$ MPa) zones, and the grain strength envelope is shown with the black solid line.

Figure 3-12a, c, and e show the scatter of grain node stresses around the $\sigma_3 = 0$ MPa axis in the unconfined compression test due to grain-scale heterogeneities. At 35% of the peak stress (Figure 3-12a), about 50.3% of the nodes are under tension (i.e., $\sigma_3 < 0$ MPa). At this stress level, the tensile stress of only a few nodes within the numerical specimen (about 0.7%) exceeds the tensile strength of the grains, which is 14 MPa (see Table 3-1). As the axial load increases (Figure 3-12c and e), the scatter in the stress magnitudes (both σ_1 and σ_3) increases. The percentage of node tensile stress magnitudes greater than the grain tensile strength also increases with increasing the axial load; 5.1% and 9.3% of the nodes at 75% and 100% of UCS, respectively. However, the percentage of node stresses experiencing tension remains constant as the axial load increases (i.e., 50.3%). Note that the average percentage of node stresses under tension for five model realizations is 50.2% and the standard deviation is 0.64%. In general, the results of elastic RS2-GBMs are consistent with those of *PFC* models by Diederichs (2000), who showed that almost half of the specimen is under tension in the UCS test. This is attributed to the grain geometric heterogeneity arising from different ball sizes and arrangements in the *PFC* model.

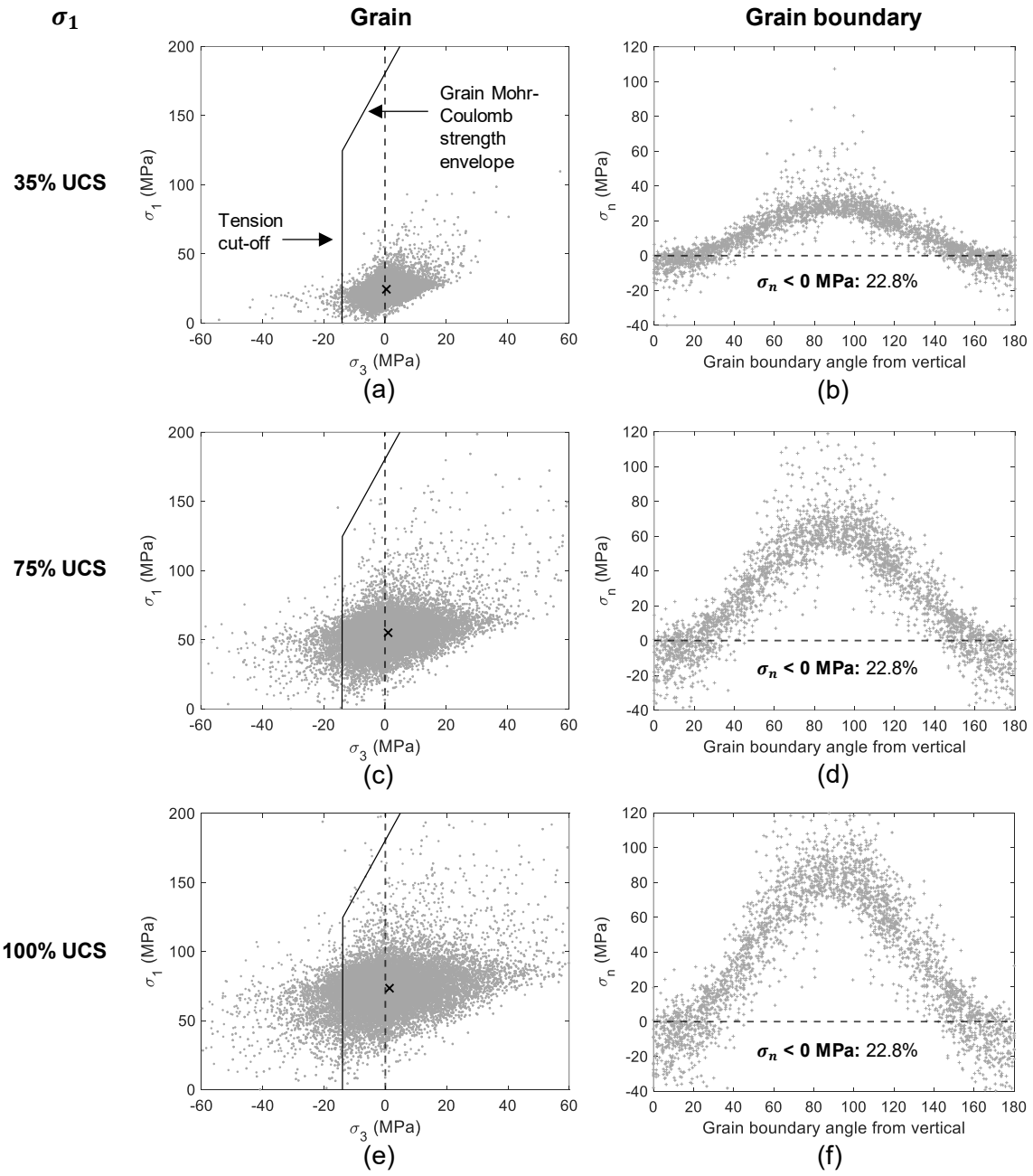

Figure 3-12: Grain-scale stresses in elastic RS2-GBM: a), c), and e) grain node stresses at 35%, 75%, and 100% of UCS; b), d), and f) grain boundary normal stress distributions at 35%, 75%, and 100% of UCS. Black dashed line represents the border between tension ($\sigma_3 < 0$) and compression ($\sigma_3 > 0$) zones. Black crosses indicate the average values of σ_1 and σ_3.

In Figure 3-12b, d, and f, the grain boundary normal stresses (σ_n) are plotted against the grain boundary angle from vertical. The black dashed line divides the compression ($\sigma_n >$ 0 MPa) and tension ($\sigma_n <$ 0 MPa) zones. In Figure 3-12b, about 22.8% of the grain

boundary segments are under tension during uniaxial loading. These grain boundaries are orientated between 0° and 40°, and between 140° and 180° from the vertical loading direction, although the majority of them are sub-parallel to the loading direction (i.e., between 0° and 10° and between 170° and 180° from vertical). The percentage of grain boundaries in the tension zone is constant and independent of the magnitude of the applied axial stress, i.e., 22.8 % (Figure 3-12d and f). However, the magnitudes of tensile stress along these grain boundaries increase as the axial load increases. This is consistent with the results of numerical simulations by Bewick et al. (2012).

Figure 3-13 illustrates the spatial distribution of elastic tensile stresses (i.e., $\sigma_3 < 0$) within the RS2-GBM at the peak stress. This figure shows that the tensile stresses are concentrated near the grain boundaries that are sub-parallel to the loading direction. The magnitudes of tensile stresses at the centre of the grains are lower than those near the subvertical grain boundaries. This suggests that grain-scale heterogeneities result in the formation of tensile stresses within the model, which could lead to the generation of tensile cracks from the grain boundaries and their propagation towards the centre of the grains as axial stress increases.

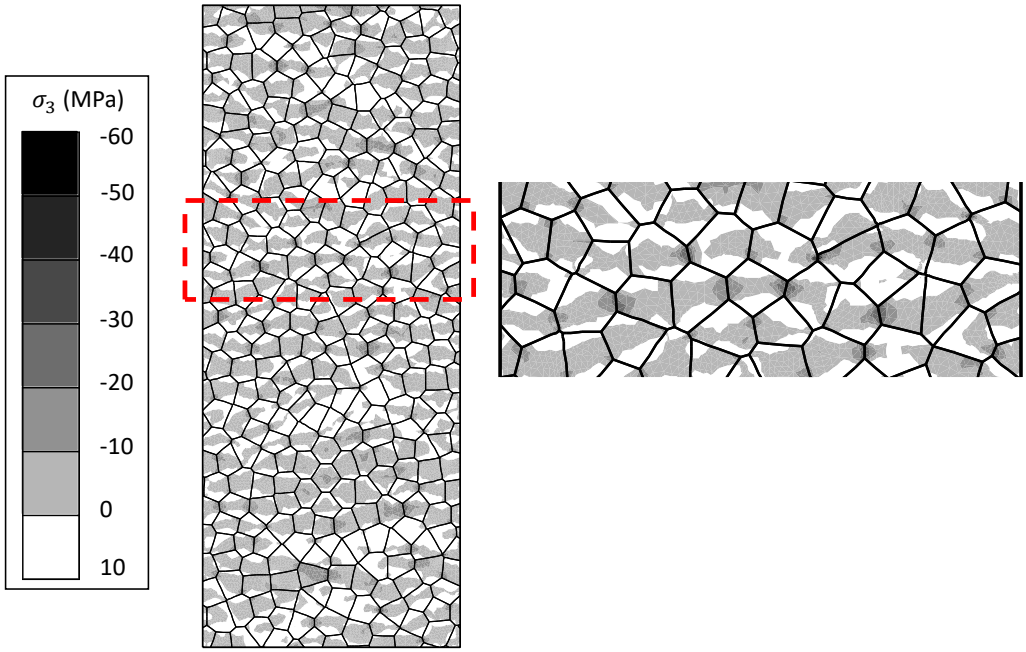

Figure 3-13: Minor principal stress contours at peak stress from elastic RS2-GBM of intact marble.

3.4.2. Confined Compression

Figure 3-14 shows the evolution of grain node stresses and grain boundary normal stresses at the peak stress for three confining pressures (i.e., 0 MPa, 3.45 MPa and 34.47 MPa). Figure 3-14a, c, and e illustrate that the scatter in the node stresses (i.e., magnitudes of σ_1 and σ_3) increases with increasing confinement, as the average value (black cross) shifts to the right in the compression zone. This results in a decrease in the percentage of grain node stresses under tension due to an increase in the confinement. Note that the percentage of node stresses under tension is reduced from 50.3% under an unconfined condition to 6.1% at a confining pressure of 34.47 MPa (Figure 3-14e).

Figure 3-14b, d, and f demonstrate how the normal stress acting on the grain boundary segments is a function of grain boundary orientation in both unconfined and confined compression tests. It can be seen from these figures that tensile stresses (σ_n < 0 MPa) are generated along the grain boundaries that are oriented between 0° and 40° and between 140° and 180° from the loading direction, although the majority of the nodes under tensile stress are sub-parallel to the loading direction (i.e., between 0° and 10° and between 170° and 180° from vertical). Furthermore, the percentage of grain boundary segments under tension decreases with increasing confinement. Note that the percentage of grain boundary segments under tension is reduced from 22.8% under an unconfined condition to 7.5% at a confining pressure of 34.47 MPa (Figure 3-14f).

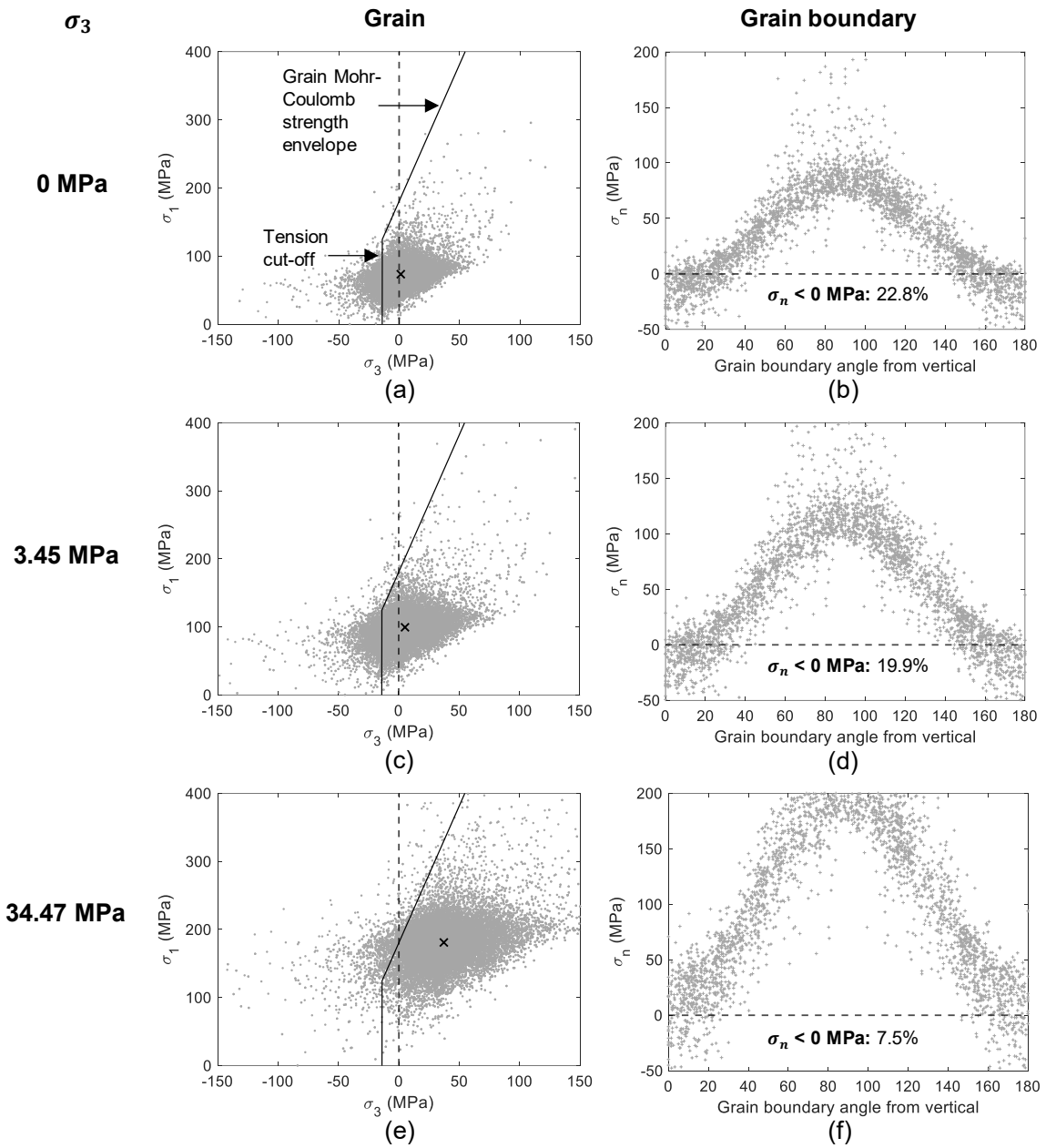

Figure 3-14: Grain-scale stresses in elastic RS2-GBM: a), c), and e) grain node stresses at 0 MPa, 3.45 MPa, and 34.47 MPa confining pressures; b), d), and f) grain boundary normal stress distributions at 0 MPa, 3.45 MPa, and 34.47 MPa confining pressures. Black dashed line represents the border between tension ($\sigma_3 < 0$) and compression ($\sigma_3 > 0$) zones. Black crosses indicate the average values of σ_1 and σ_3.

Figure 3-15 summarizes the percentages of node stresses (Figure 3-15a) and grain boundary segments (Figure 3-15b) experiencing tension over the full range of confinement. Both Figure 3-15a and b show that the percentages of grain node stresses and grain boundary segments under tension decrease with increasing confinement.

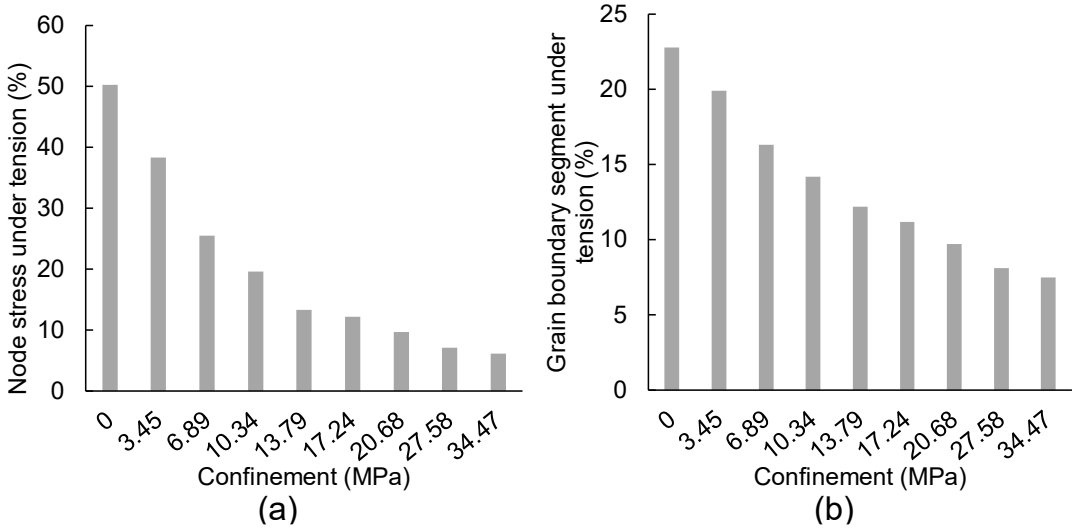

Figure 3-15: Percentages of: a) node stresses; and b) grain boundary segments under tension in elastic RS2-GBM.

The results of elastic RS2-GBMs presented in this section demonstrated how grain-scale heterogeneity results in the generation of tensile stresses within a rock specimen under an overall compressive loading condition. Furthermore, it was illustrated how the confining pressure reduces the tensile stresses generated within the grains and along the grain boundaries, although some tensile stresses are still formed even at high confining pressures. This is consistent with the results of numerical analyses by Sinha and Walton (2020), who used the Bonded Block Model (BBM) in UDEC to simulate laboratory triaxial tests on Creighton granite. They found that the number of tensile cracks decreased, and the number of shear cracks increased with increasing confinement, although some tensile cracks still occurred at high confinement (e.g., 60 MPa; Sinha & Walton, 2020). Note that no attempt was made to quantify the level of heterogeneity of the GBM in the present study. Further information on how to measure heterogeneity in a GBM can be found in Liu et al. (2018).

3.5. Stress-Strain Response and Failure Mode

The results of the calibrated RS2-GBMs of intact and granulated marble, including the stress-strain curves and failure modes under unconfined and confined compression are presented in this section. In these models, the stresses were continuously calculated at all loading stages by averaging the stresses of all the nodes within the GBM. The strain was

measured from the displacement of the upper model boundary. Note that the lower model boundary was fixed in vertical direction.

3.5.1. Unconfined Compression

Figure 3-16 presents the stress-strain curves for the RS2-GBMs of intact and granulated marble under unconfined compression. In this figure, the GBM of intact marble exhibits a brittle response with a sudden stress drop following the peak stress (Figure 3-16a). In contrast, the GBM of granulated marble shows ductile behavior (Figure 3-16b).

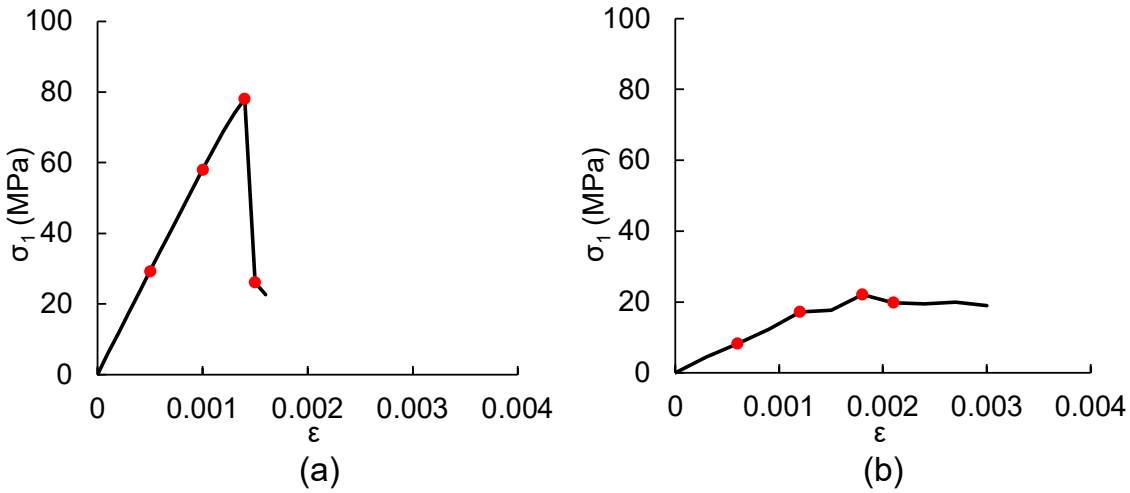

Figure 3-16: Stress-strain curves of RS2-GBMs for: a) intact; and b) granulated marble under unconfined compression. The red circles on each curve represent loading stages at 35%, 75%, 100% of the UCS and the first loading stage in the post-peak region.

Figure 3-17 illustrates the progressive damage (i.e., grain and grain boundary yielding) at 35%, 75%, and 100% of the UCS, and the first loading stage in the post-peak region of the GBMs of intact (Figure 3-17a) and granulated (Figure 3-17b) marble. These stages are highlighted with red circles on the stress-strain curves in Figure 3-16. The upper images in Figure 3-17a show that the grain boundary yielding initiates before 35% of the UCS in the GBM of intact marble. As can be seen in these figures, grain boundary cracks (i.e., yielded joints) are subparallel to the loading direction. The crack initiation stress level for the calibrated GBM of intact marble is lower than that of a typical crystalline rock. This is considered to be a limitation of the adopted calibration procedure. It is possible to increase the grain boundary tensile strength to obtain a more realistic crack initiation stress level.

However, this would affect the peak strength of the GBM of intact marble at low confinement. Therefore, the crack initiation stress level was not considered as a calibration target in this study.

The lower images of Figure 3-17a show that the grains start to yield at about 75% of the UCS. The yielded grains are randomly located within the specimen. At the post-peak stage, the yielded grains propagate to form a through-going yielded zone representing a macro-fracture. The pattern of yielded grains suggests combined axial splitting and shear failure as the primary mode of failure for the GBM of intact marble under unconfined compression. In this model, only 5.5% of the elements yielded up to the peak stage, while 36.4% of the elements yielded in the first post-peak stage. The significant amount of yielded grains at the post-peak stage is attributed to the influence of heterogeneity on the generation of tensile stresses (shown in Figure 3-12). Note that the residual tensile strength of the finite elements is nearly zero (0.1 MPa). This means that when an element yields in tension, its tensile strength drops to 0.1 MPa. This results in further redistribution of the stresses in adjacent elements and yielding of more elements in tension. Therefore, more yielded grains occur in the post-peak stage than pre-peak stages, especially at low confinement, where the type of most yielded elements is tension.

The upper images in Figure 3-17b illustrate that most of the grain boundaries in the model of granulated marble yield during the early stages of uniaxial loading (i.e., $\sigma_1 < 35\%$ UCS). This is due to the low tensile strength of 0.1 MPa assigned to the grain boundaries simulating thermal-induced grain boundary damage. The lower images in Figure 3-17b show that only a few grains randomly located within the GBM yielded during uniaxial loading. In general, the results of simulations using the RS2-GBM in terms of the failure modes for both intact and granulated marble are consistent with those of PFC-GBMs reported by Bahrani et al. (2014).

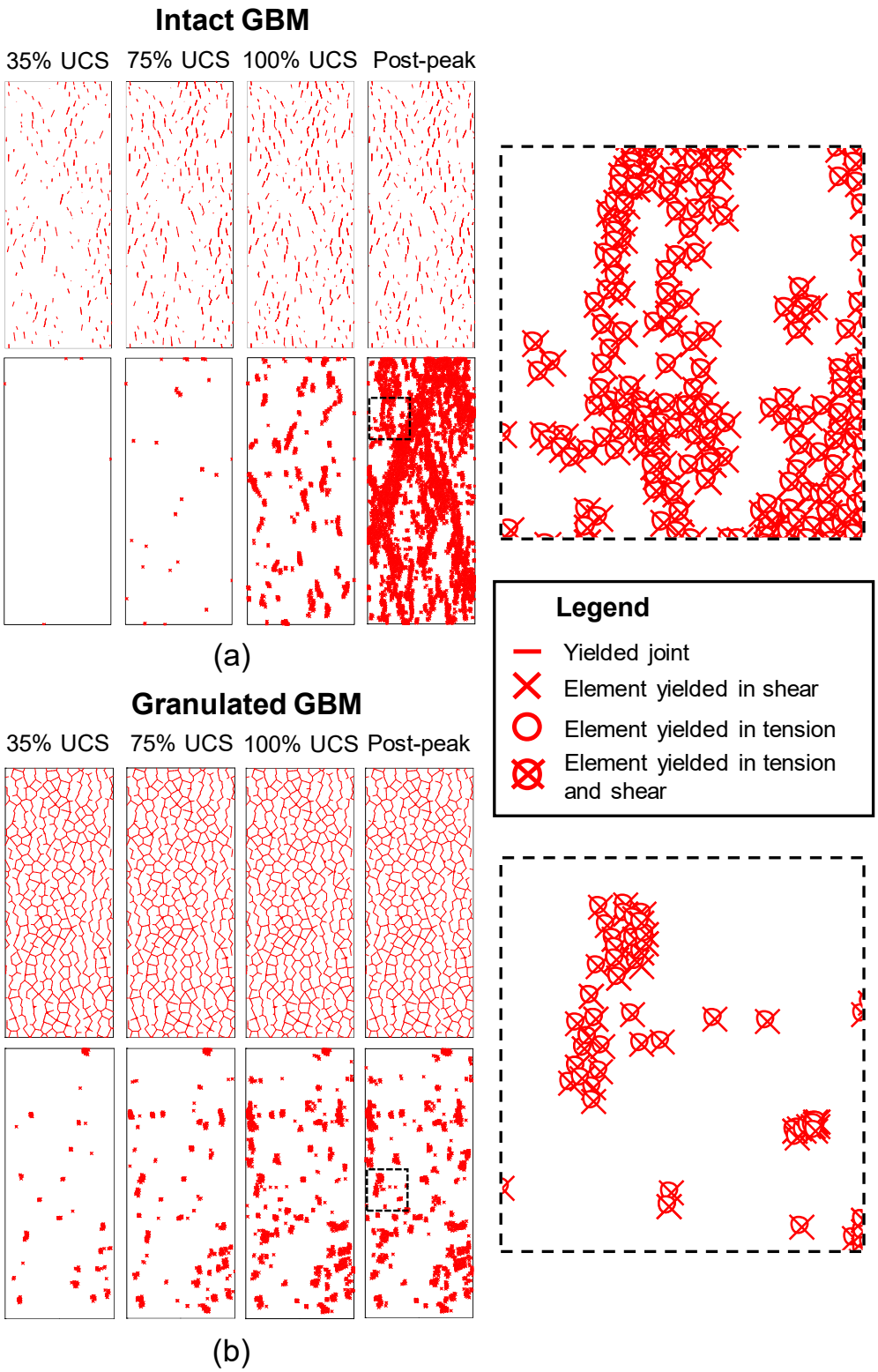

Figure 3-17: Progressive failure of RS2-GBMs of: a) intact; and b) granulated marble under unconfined compression. Yielded grain boundaries (upper images) and yielded grains (lower images) are presented at four loading stages indicated by red circles in Figure 3-16.

3.5.2. Confined Compression

Figure 3-18 shows the stress-strain curves of the calibrated RS2-GBMs of intact and granulated marble at different confining pressures (i.e., 0 - 34.47 MPa). As can be seen in Figure 3-18a, the known transition in the post-peak response from brittle to ductile with increasing confinement is well captured by the GBM of intact marble. This is consistent with the laboratory test results by Gerogiannopoulos (1976) and Paterson (1958), as shown in Figure 3-1a and b. The stress-strain curves for the GBM of granulated marble shows a perfectly plastic response up to about 10 MPa confinement and becomes strain hardening at higher confining pressures (Figure 3-18b). This is not consistent with the laboratory test results reported by Gerogiannopoulos (1976) (Figure 3-1c) and Rosengren and Jaeger (1968) (Figure 3-1d), who show that the post-peak response of granulated marble is strain softening under unconfined compression and gradually changes to perfectly plastic as the confining pressure increases to 34.47 MPa.

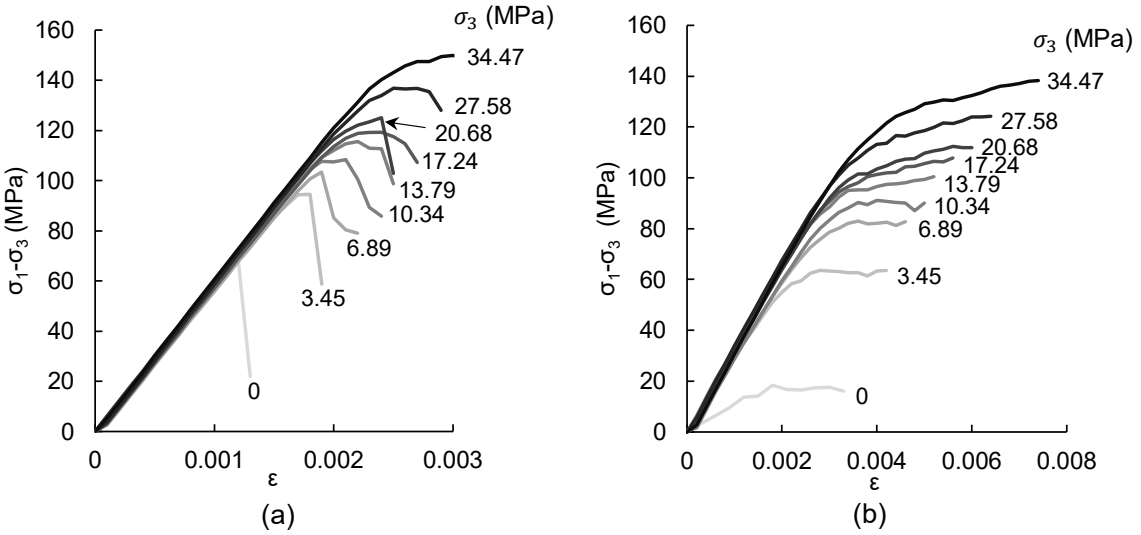

Figure 3-18: Stress-strain curves for RS2-GBMs of: a) intact marble; and b) granulated marble.

Figure 3-19 presents the failure modes of intact marble at various levels of confinement (i.e., 0 MPa, 3.45 MPa and 34.47 MPa) obtained from laboratory tests and numerical simulations conducted using RS2-GBM (this study) and PFC-GBM (by Bahrani et al., 2014). Figure 3-19a, e, and i show the yielded grains (right) and grain boundaries (left) in RS2-GBM. The images on the left show that the yielded grain boundaries are oriented subparallel to the loading direction. Although the number of yielded grain boundaries

decreases as the confining pressure increases, some yielded grain boundaries still occur at high confinement (i.e., Figure 3-19i). This is consistent with the results of elastic analyses discussed in the previous section (i.e., Figure 3-14 and Figure 3-15), showing that some of the grain boundaries are under tension even at high confinement.

The patterns of yielded grains shown in Figure 3-19a, e and i are used to identify the mode of failure for the RS2-GBM at different confining pressures. The failure modes of RS2-GBMs of intact marble are consistent with those obtained from laboratory tests by Paterson (1958): axial splitting under unconfined compression (Figure 3-19b); shear failure at low confinement (Figure 3-19f); and conjugate shear bands at high confinement (Figure 3-19j). The failure modes captured by RS2-GBMs are also comparable to those of PFC-GBMs, as shown in Figure 3-19c, g, and k. The images on the left and right illustrate inter- and intra-grain cracks in the PFC-GBM, respectively. The results of PFC-GBMs indicate that: 1) in the unconfined compression test, macro-fractures are mainly formed by the accumulation of inter-grain tension cracks that are sub-parallel to the loading direction (Figure 3-19c); and 2) in the confined compression tests, the macroscopic shear bands are formed due to the interaction of inter- and intra-grain tensile cracks, although the number of shear cracks increases with increasing confinement (Figure 3-19g and k; Bahrani et al., 2014).

The failure modes of PFC-GBMs are generally consistent with those of RS2-GBMs, although the PFC-GBMs show a different mode of grain failure. The results of PFC-GBM show that the number of inter-grain shear cracks increases with increasing confinement. However, in the RS2-GBM, the number of yielded grain boundaries decreases as confinement increases. It is found that the contribution of yielded grain boundaries in the RS2-GBM at the post-peak stages (Figure 3-19i) is less than that in the PFC-GBM (Figure 3-19k) at high confinement. Furthermore, the upper images of Figure 3-19d, h, and l illustrate that the grains in the RS2-GBM yield in both tension and shear at zero and 3.45 MPa confinements, and in pure shear at 34.47 MPa confinement (upper image in Figure 3-19l). However, the lower images in Figure 3-19d and h illustrate that most of the intra-grain cracks at zero and 3.45 MPa confinements in the PFC-GBM are tensile cracks. At high confinement, the failed grains in the PFC-GBM consist of tensile and shear cracks (lower image in Figure 3-19l).

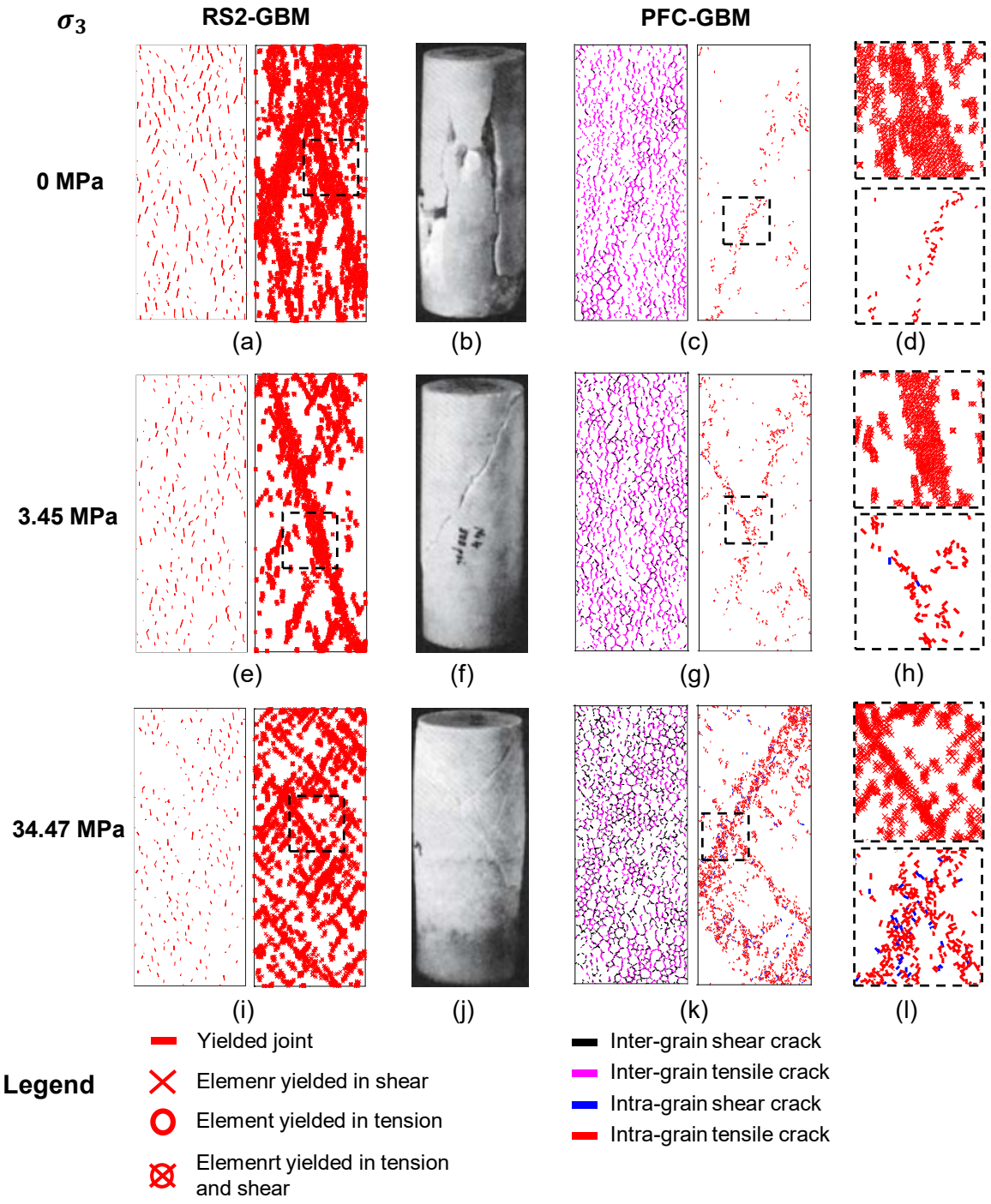

Figure 3-19: Failure modes of intact marble at various levels of confinement: a), e), and i) RS2-GBM in this study; b), f), and j) laboratory triaxial tests by Paterson (1958); c), g), and k) PFC-GBM by Bahrani et al. (2014). d), h) and l) closer views of grain failure in RS2-GBM (upper images) and PFC-GBM (lower images).

A comparison between the failure modes of RS2-GBM (Figure 3-20a, d and g) and PFC-GBM (Figure 3-20b, e and h) of granulated marble is provided in Figure 3-20. In the unconfined compression test simulated in RS2 (Figure 3-20a), most of the grain boundaries

yield due to their low tensile strength and cohesion of 0.1 MPa. However, only a few grains, randomly located within the numerical specimen, yield in both tension and shear (upper image in Figure 3-20c). This is consistent with the failure mode of PFC-GBM (Figure 3-20b), which shows only a few intra-grain tensile cracks (lower image in Figure 3-20c). Note that it was assumed by Bahrani et al. (2014) that all the grain boundaries in the PFC-GBM of granulated marble are purely frictional (i.e., zero tensile strength and cohesion). Therefore, only intra-grain cracks can be seen in their simulation results. Bahrani et al. (2014) discussed that the failure of PFC-GBM of granulated marble at zero confinement mainly involves sliding of the grains along their boundaries, and for this reason, only a few intra-grain cracks occur under unconfined compression. This is well captured by the calibrated RS2-GBM.

The number of yielded grain boundaries in the RS2-GBM at low confinement (i.e., σ_3 = 3.45 MPa; Figure 3-20d) is lower than that under unconfined compression. The yielded grain boundaries are mainly subparallel to the loading direction in this model. The number of yielded grains at this confining pressure is more than that of the RS2-GBM under an unconfined condition (image on the right side of Figure 3-20d). This is also consistent with the results of PFC-GBM by Bahrani et al. (2014), who noted that a small amount of confinement prevents the grains from opening and sliding along their boundaries, resulting in an increase in the number of intra-grain cracks at this confining pressure compared to an unconfined condition (Figure 3-20e).

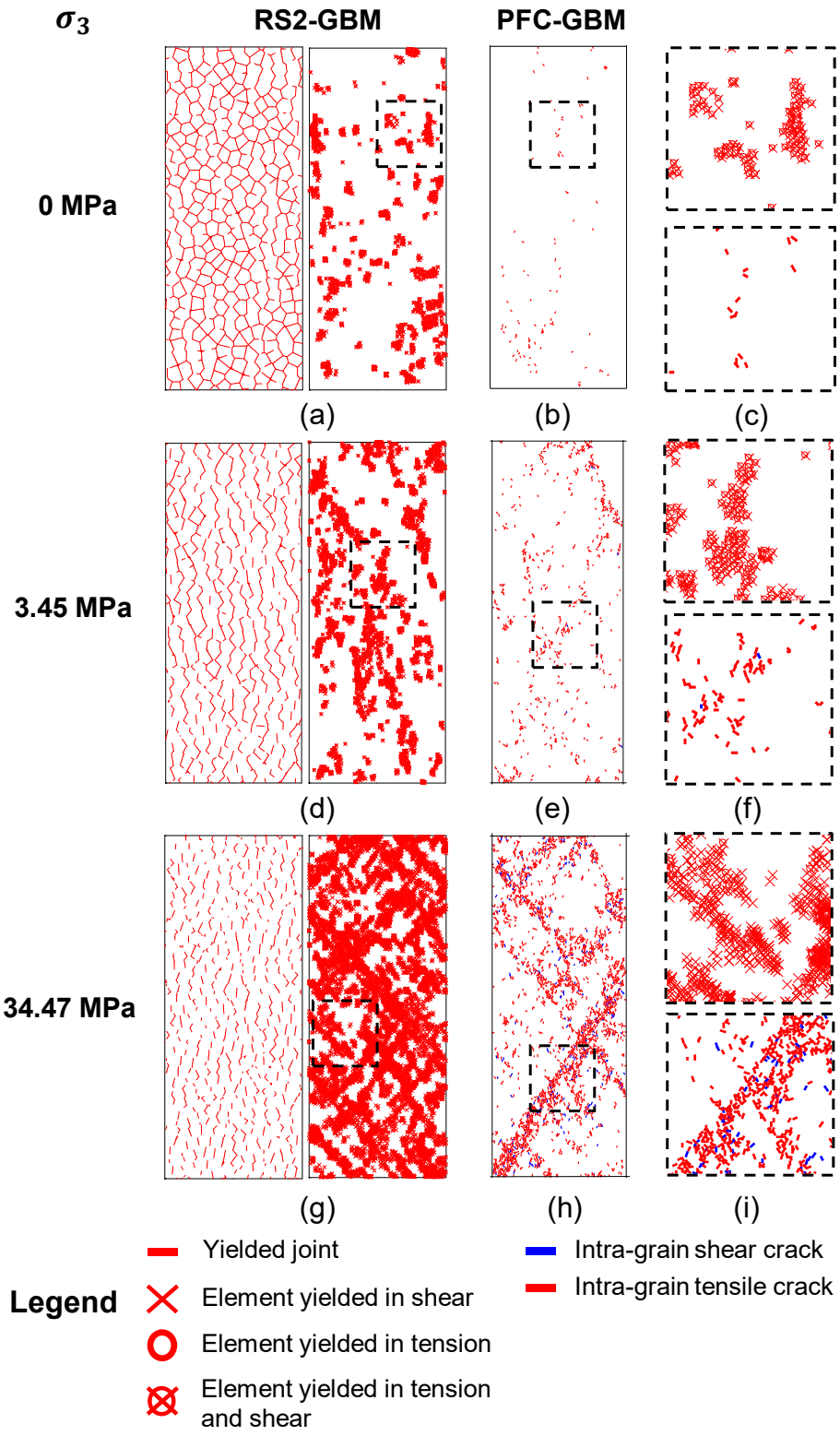

Figure 3-20: Simulated failure modes of granulated marble at various levels of confinement: a), d), and g) RS2-GBM in this study showing grain boundary (left) and grain (right) yielding; b), e), and h) PFC-GBM by Bahrani et al. (2014) showing intra-grain cracks; and c), f), and i) closer views of grain failure in RS2-GBM (upper images) and PFC-GBM (lower images).

At high confinement (i.e., σ_3 = 34.47 MPa; Figure 3-20g), fewer yielded grain boundaries, which are shorter in length, are seen in the RS2-GBM of granulated marble compared to those at zero and 3.45 MPa confining pressures. The pattern of yielded grains shown in the image on the right side of Figure 3-20g suggests a conjugate shear banding as the main mode of failure at this confining pressure. This failure mode is comparable to that of PFC-GBM (Figure 3-20h). The macroscopic shear fractures in the PFC-GBM are formed due to the interaction between intra-grain tensile and shear cracks (lower image of Figure 3-20i) (Bahrani et al., 2014), while in the RS2-GBM, the failed grains consist of several elements yielded in shear (upper image of Figure 3-20i). This is also consistent with the results of elastic analyses (Figure 3-14), which suggest that most of the nodes are under compression at high confinement (i.e., σ_3 = 34.47 MPa). When the shear stress exceeds the shear strength of a finite element inside a grain, the element yields in shear. For this reason, the mode of yielded elements at high confinement is shear only. Unfortunately, neither Rosengren and Jaeger (1968) nor Gerogiannopoulos (1976) provided the pictures of failed granulated marble specimens at these confining pressures. Therefore, the failure modes of RS2-GBMs of granulated marble were only compared to those of PFC-GBMs by Bahrani et al. (2014).

3.6. DISCUSSION

It was demonstrated in this chapter that the proposed continuum grain-based model (RS2-GBM) captures some of the important characteristics of brittle rocks under laboratory loading conditions. The simulation results were also found to be consistent with those of calibrated PFC-GBMs reported by Bahrani et al. (2014). However, this modeling approach, as other numerical methods used to simulate the micro-mechanical behavior of brittle rocks, has its own limitations. Among them are its limitations in capturing the non-linearity of the stress-strain curve due to crack closure and the observed post-peak response for granulated marble. These are discussed in more detail in this section.

3.6.1. Non-Linear Stress-Strain Curve

According to Martin and Chandler (1994) and Hoek and Martin (2014), the stress-strain curve of a brittle rock can be divided into five regions: 1) crack closure, 2) elastic region, 3) stable crack growth, 4) unstable crack growth, and 5) peak and post-peak region. The non-linearity of the stress-strain curve in the early loading stages (i.e., crack closure) is caused by the closure of pre-existing (natural or drilling-induced) micro-cracks (e.g., grain boundary cracks, intragranular cracks, and trans-granular cracks; Lim et al., 2012). In Figure 3-1, the stress-strain curves of granulated marble show a more non-linear response than those of intact marble due to the high density of grain boundary cracks caused by heating.

A comparison between the axial stress-axial strain curve of intact Wombeyan marble under an unconfined condition and those of calibrated PFC-GBM and RS2-GBM are provided in Figure 3-21a. It can be seen in this figure that neither PFC-GBM nor RS2-GBM captures the initial non-linear region of the stress-strain curve in intact marble. Unfortunately, Gerogiannopoulos (1976) did not provide the stress-strain curve of granulated Wombeyan marble under unconfined compression. However, it is expected from the results of laboratory tests by Rosengren and Jaeger (1968) that the stress-strain curve of granulated Wombeyan marble under unconfined compression is highly non-linear (see Figure 3-1d). Figure 3-21b also shows that the stress-strain curves of the calibrated PFC-GBM and RS2-GBM of granulated marble are linear. This is because micro-cracks in the granulated marble specimens caused by heating were simulated as frictional, but not open cracks. Therefore, their closures during compressive loading were not captured by the GBMs.

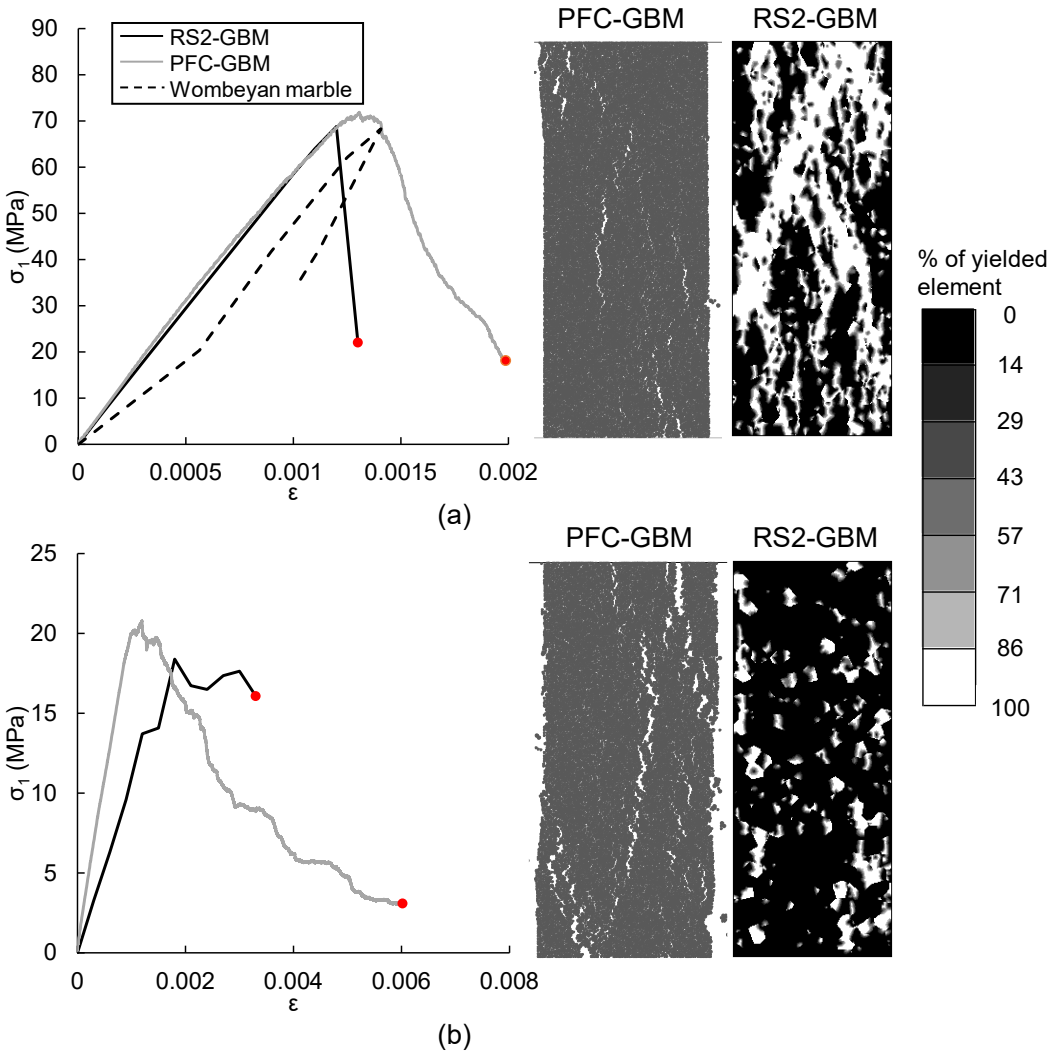

Figure 3-21: Stress-strain curves and failure modes of RS2-GBM and PFC-GBM under unconfined compression for: a) intact marble; and b) granulated marble. In Figure 3-21a, the stress-strain curves of calibrated GBMs are compared to that of intact Wombeyan marble by Gerogiannopoulos (1976). Note: simulated failure modes correspond to the loading stages shown by red circles on the stress-strain curves.

In the granulated marble, it is observed that the non-linearity of the stress-strain curves decreases (Figure 3-1c and d) and the Young's modulus increases as confinement increases (Figure 3-11). Both RS2-GBM and PFC-GBM of granulated marble overestimate the unconfined Young's modulus of granulated marble when calibrated to its confined Young's modulus. This is because grain boundary damage in the granulated marble was not simulated as open cracks. For this reason, only the Young's modulus of the GBM at high confinement (i.e., σ_3 > 17.24 MPa) was matched to that of granulated Wombeyan marble. It is worth mentioning that thermal-induced micro-cracking and associated crack

closure during compressive loading and non-linear stress-strain response have been explicitly simulated in PFC by Tian et al. (2020).

3.6.2. Post-Peak Behavior

Figure 3-1a and b show that the post-peak response of intact Wombeyan marble is brittle at zero confinement, changes to strain-softening at low confinement, becomes perfectly plastic at high confinement, and exhibits a strain hardening behavior at extremely high confinement. This is well captured by the calibrated RS2-GBM of intact marble (Figure 3-18a). The granulated Wombeyan marble responds in a strain softening manner for a wide range of confining pressure, and only shows a perfectly plastic behavior at high confinement (Figure 3-1c and d). This behavior was well captured in PFC-GBM by Bahrani et al. (2014). However, the post-peak response of the calibrated RS2-GBM of granulated marble is perfectly plastic for the full range of confinement, as shown in Figure 3-18b and Figure 3-21b. This is interpreted to be due to the amount of grain yielding and its residual strength, which control the post-peak response of the RS2-GBM.

In the simulations of intact marble, the failure of RS2-GBM at zero confinement is dominated by progressive grain boundary yielding in the pre-peak loading stages. Once the stress passes its peak value, a large number of grains yield simultaneously, resulting in a sudden drop in the stress to its residual value (Figure 3-21a). For this reason, the RS2-GBM of intact marble exhibits a brittle response under unconfined compression. In the RS2-GBM of granulated marble, the failure is dominated by yielding of the grain boundaries, which are frictional contacts with the same peak and post-peak strength and deformation properties. The perfectly plastic response of RS2-GBM of granulated marble is therefore attributed to the yielding of only a few grains which begins in the pre-peak loading stages and gradually increases in the post-peak region (see Figure 3-17b).

The difference in the kinematic assumptions and formulations of the joints in the FEM and the DEM, representing grain boundaries in the GBM, could also contribute to different post-peak responses observed in the RS2-GBM and PFC-GBM (Figure 3-21b). As discussed earlier, the grain boundaries in the RS2-GBM are simulated using joint elements,

which are four-noded quadrilateral interfaces with negligible thickness. According to Riahi et al. (2010), the interconnectivity between the solid and the joint element in the FEM remains unchanged throughout the solution process, despite the displacement that occurs. This means that the detachment of grains at their boundaries is not simulated in RS2-GBM (Figure 3-21). However, in the DEM, contact pairings can change throughout the solution process as the algorithm updates the positions of the discrete objects and determines detached as well as newly formed contacts (Riahi et al., 2010). In the PFC-GBM, the grain boundaries are represented by smooth-joint contacts that can simulate problems in which block connectivity changes extensively, resulting in complete detachment and large deformation (see failure mode of PFC-GBM in Figure 3-21). The detached grains result in the redistribution of stresses within the specimen, reducing the average stress to a residual value that is lower than that of RS2-GBM for the same amount of axial strain (e.g., compare the axial stresses at 0.003 axial strain in Figure 3-21b). While the interconnectivity between the grains in the RS2-GBM remains unchanged (i.e., grains do not detach), only the residual grain strength can contribute to the post-peak strength. Since only a few grains yield during the failure process of the RS2-GBM of granulated marble, the stress-strain curve of this model exhibits a plastic response. This means that much higher stress is required in the RS2-GBM to achieve the same amount of strain that occurred in the PFC-GBM.

3.6.3. Path Forward

As mentioned earlier, granulated marble is suggested to serve as an analogue for a highly interlocked jointed rock mass (Bahrani et al., 2014; Bahrani & Kaiser, 2013). In this material, the grains and grain boundaries are analogues for rock blocks and block boundaries (i.e., joints) in a jointed rock mass. Apart from some of the limitations of the RS2-GBM discussed above, this modeling approach is proven to be capable of capturing some of the unique characteristics of granulated marble, including the rapid increase in the peak strength with increasing confinement, resulting in a highly non-linear strength envelope (Figure 3-10). This suggests that this modeling approach can potentially be used as a tool to simulate highly interlocked jointed rock masses and estimate their strengths,

especially at high confinement. This is of significant importance for hard rock pillar design in deep mines (Bahrani et al., 2014; Kaiser et al., 2011).

Bahrani et al. (2014) suggest that a numerical model properly calibrated to the strength of granulated Wombeyan marble can potentially capture the rapid strengthening effect of jointed hard rock pillars with increasing the width-to-height ratio observed in the pillar database (Lunder & Pakalnis, 1997; Martin & Maybee, 2000). In this regard, the PFC-GBM would probably be an appropriate tool to simulate jointed pillars, not only because it captures the peak strengths and failure modes of granulated marble, but also because it results in a more representative post-peak response compared to the calibrated RS2-GBM. This is because PFC-GBM can simulate progressive inter- and intra-block fracturing processes and block detachment past the peak stress, resulting in a more realistic stress redistribution within the pillar during mining-induced stress changes. However, the main advantage of the RS2-GBM over PFC-GBM is its much shorter computation time, making it a more practical tool, not only during the model calibration stage but also for generating and running large-scale mine models. For example, in a finite element model of a mine pillar, the Voronoi tessellation approach can be used to simulate the pillar and its nearby jointed nature of the rock mass with input properties of the calibrated RS2-GBM of granulated marble. A homogeneous material with equivalent strength and deformation properties can then be used to represent the rock mass far from the pillar to capture the stress redistribution caused by excavations.

3.7. SUMMARY

In this chapter, the applicability of a continuum grain-based model developed in RS2 (called RS2-GBM) for simulating brittle rock failure was evaluated by simulating the laboratory behavior of intact and heat-treated (granulated) Wombeyan marble reported by Gerogiannopoulos (1976). A systematic calibration approach was used to match the macro-properties of RS2-GBMs to those of intact and granulated marble.

The results of simulations using elastic RS2-GBMs showed that grain-scale heterogeneity controls the variation of stresses within a specimen during compressive loading. Both grains and grain boundaries experience tensile stresses during compressive loading, even

at high confinement. The results of simulations using inelastic RS2-GBMs of intact marble indicated that grain boundary yielding mainly occurs during pre-peak loading stages, while grain yielding dominates the failure in the post-peak region. It was shown that the RS2-GBM calibrated to the peak strength of intact marble could capture the observed post-peak response and failure mode at different levels of confinement.

The RS2-GBM well captured the non-linear strength envelope of the granulated marble. Although the failure modes of RS2-GBM of granulated marble were found to be consistent with those of previously calibrated PFC-GBM, it exhibited a plastic post-peak response, independent of confinement. This is interpreted to be due to the gradual yielding of a few grains in the post-peak region and the inability of the RS2-GBM in capturing grain detachment from their frictional boundaries that occur in the post-peak loading stages of the granulated marble.

Detailed analysis of the calibrated RS2-GBMs of intact and granulated marble revealed that the proposed continuum GBM can be used as a tool for simulating brittle rock failure. The advantage of this modeling approach over discontinuum GBMs (e.g., PFC-GBM) is its shorter runtime resulting in more efficient model calibration. In the next chapter, the calibrated RS2-GBM of granulated marble, which is suggested to serve as an analogue for a highly interlocked jointed rock mass, is used to simulate jointed pillars to better understand their strengths and failure mechanisms as a function of pillar width-to-height ratio.

CHAPTER 4 SIMULATION OF HIGHLY INTERLOCKED JOINTED PILLARS USING UPSCALED CONTINUUM GRAIN-BASED MODELS

4.1. INTRODUCTION

The majority of research on pillar design, including empirical formulae (Hedley & Grant, 1972; Von Kimmelmann et al., 1984; Krauland & Soder, 1987; Potvin et al., 1990; Lunder and Pakalnis, 1997) and numerical simulations (Martin & Maybee, 2000; Mortazavi et al., 2009; Kaiser et al., 2011; Sinha & Walton, 2018; Rafiei Renani & Martin, 2018), has been mostly focused on estimating the strength of pillars in massive to moderately jointed rock masses. As such, minimal work has been conducted to better understand the influence of the degree of block interlock, which in fact, is an important parameter in determining the GSI value for a jointed rock mass, on the strength of jointed pillars. Furthermore, the continuum methods commonly used to simulate pillars consider the rock mass as a homogeneous medium. Although these methods employ complex constitutive laws to represent the post-peak rock mass response, they fail to capture the observed pillar failure mechanisms. In order to address these gaps, this chapter aims at investigating the strength and failure mechanisms of jointed pillars by explicitly simulating rock mass geometric heterogeneities using a two-dimensional (2D) continuum numerical modelling approach.

For this purpose, numerical simulations are conducted with respect to the laboratory properties of heat-treated Wombeyan marble, which has been suggested by Bahrani and Kaiser (2013) and Bahrani et al. (2014) to serve as an analogue for a highly interlocked jointed rock mass. First, the previously calibrated continuum Grain-Based Model (GBM) of heat-treated marble is upscaled to simulate rib pillars of various W/H ratios. Next, the modeled pillars are loaded monotonically until reaching failure. The pillar strength as a function of pillar W/H ratio is compared to those estimated by other continuum and discontinuum models. The simulation results of jointed pillars provide insights into the role of geometric heterogeneity on damage initiation and propagation, leading to the failure of pillars of various W/H ratios during compressive loading.

4.2. GRANULATED MARBLE, AN ANALOGUE FOR A HIGHLY INTERLOCKED JOINTED ROCK MASS

As discussed in Chapter 1, Bahrani and Kaiser (2020) investigated the applicability of the Hoek-Brown failure criterion for estimating the confined strength of granulated marble (i.e., highly interlocked jointed rock mass analogue). For this purpose, they modified the calibrated PFC-GBM of granulated marble to generate a massive rock mass model by removing the frictional joints and replacing them with cohesive bonds. They used the Hoek-Brown failure criterion with a GSI value of 100 to fit the strength of the massive rock mass model. Next, they lowered the GSI value to 67 to match the UCS of the model of granulated marble (see Figure 1-5).

A similar exercise was conducted using the results of calibrated RS2-GBM. First, the Hoek-Brown failure criterion with a GSI value of 100 was used to represent the strength of a massive rock mass (Figure 4-1). In this case, the strength of the massive rock mass was assumed to be the same as the strength of the grains representing rock blocks in the calibrated RS2-GBM of Wombeyan marble, which has a UCS of 180 MPa (i.e., c_{gp} = 45 MPa and φ_{gp} = 37°). Then, the GSI value was lowered to 63 to match the UCS of the jointed rock mass model. As shown in Figure 4-1, the confined strength of the jointed rock mass model is underestimated by the HB-GSI approach. Next, the GSI value was increased to 76 to match the confined strength of the jointed rock mass model. Figure 4-1 shows that the estimated strength envelope overestimates the UCS of the jointed rock mass model.

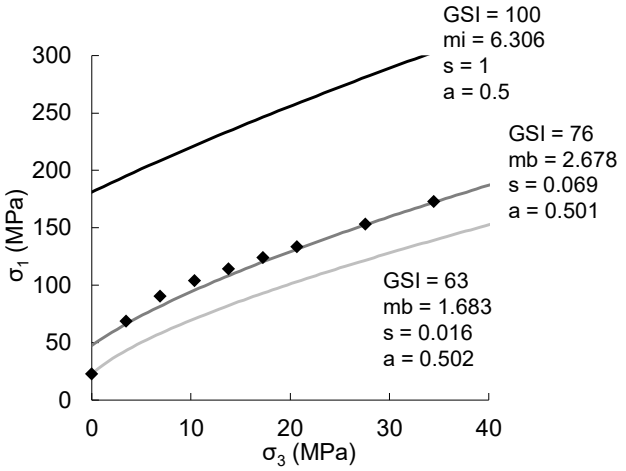

Figure 4-1: Comparison between the strengths and the Hoek-Brown failure envelopes for massive rock mass model and highly interlocked jointed rock mass model (i.e., granulated marble).

The results of this exercise indicate that the HB-GSI approach cannot capture the rapid strengthening behavior of highly interlocked jointed rock masses due to confinement. This has important implications for the design of jointed pillars. The UCS of a jointed rock mass is most relevant when estimating the strength of slender pillars (e.g., W/H = 0.5) and the strength at the walls of wide pillars (e.g., W/H = 2) due to their relatively low confinement. However, the confined strength of a jointed rock mass becomes relevant when estimating the strength of the pillar core and designing wide pillars (e.g., W/H = 2). Therefore, since the HB-GSI approach cannot capture the observed rapid strengthening behavior of highly interlocked jointed rock masses, the design of highly interlocked jointed pillars based on this approach may lead to over-sized pillars and therefore ore loss.

In Chapter 3, it was suggested that the RS2-GBM can be used as an alternative tool to simulate jointed rock masses and estimate their strength because of its much shorter computation time compared to discontinuum modeling approaches. In this chapter, the calibrated RS2-GBM of granulated marble is upscaled to simulate jointed rib pillars to gain better insights into their strength and failure mechanisms. In the following section, detailed descriptions of the adopted model upscaling approach and the development of the pillar models are provided.

4.3. SIMULATION OF HIGHLY INTERLOCKED JOINTED PILLARS

4.3.1. Upscaling Approach in RS2-GBM

According to Shin (2010), Lan et al. (2013), and Dadashzadeh (2020), the calibrated GBMs can be upscaled to investigate the response of rock masses near the pillar walls and around the underground openings. Herein, two approaches can be used to increase the size of a GBM: 1) increasing the size of the model without changing the grain size; and 2) increasing the size of both the model and the grains by keeping their size ratio constant. Several researchers have used the former approach to investigate the influence of the specimen size on the UCS of defected and non-defected rocks (e.g., Bahrani & Kaiser, 2016; Li et al., 2018; Stavrou et al., 2019). The latter approach, in which both the model and the grain sizes are increased, has been used by Dadashzadeh (2020) to simulate brittle failure around underground openings. For this purpose, Dadashzadeh (2020) proposed a two-step upscaling approach in a UDEC grain-based model with elastic Voronoi blocks (i.e., grains): 1) parameter upscaling, and 2) geometry upscaling. First, she calibrated a UDEC-GBM to the results of triaxial compression tests on a limestone. In the parameter upscaling stage, she iteratively reduced the peak friction angle of the contacts (i.e., grain boundaries) from 40° to 0° until the model UCS matched the in-situ spalling strength (i.e., crack initiation stress level). In the next step, she upscaled the model geometry (from laboratory to in situ) by maintaining the ratio between the model and grain sizes. This required an adjustment to the contact normal and shear stiffness values to ensure that the macro-strength of the upscaled GBM remains the same as the in-situ spalling strength.

Since granulated marble is considered as an analogue for a highly interlocked jointed rock mass, the RS2-GBM of granulated marble should be upscaled in a way that the strength and deformation properties of the jointed rock mass model remain the same as those of granulated marble. For this reason, the geometry upscaling approach proposed by Dadashzadeh (2020) was adopted in this chapter to increase the scale of the calibrated GBM to that of a rock mass to simulate jointed pillars. Therefore, the ratio of the model size to the grain size was kept constant, and only the joint stiffness properties were adjusted.

Figure 4-2a shows the RS2-GBMs at two scales, indicating that the geometric arrangements of the Voronoi blocks (i.e., grains) in the original and upscaled models are the same. This means that the total numbers of Voronoi blocks and joint elements are identical in the two models. Figure 4-2b shows the influence of the model scale on the UCS and Young's modulus of the GBM. Note that the UCS and Young's modulus of upscaled models are normalized to those of the original model (i.e., laboratory-scale model). In Figure 4-2b, the joint (normal and shear) stiffness properties of the upscaled GBMs are the same as those of the original model. As shown in this figure, both the UCS and Young's modulus of the GBM increase as the model scale increases.

Figure 4-2c illustrates the relationship between the joint stiffness ratio (R_J) and the model geometry scaling ratio (R_G) required to obtain the same simulation results (i.e., strength, Young's modulus, and failure mode) in different model scales. R_J is the ratio between the joint normal (or shear) stiffness in the upscaled model and that in the original model (i.e., laboratory scale). R_G is the ratio between the width (or height) of the upscaled model and that of the original model (i.e., laboratory scale). As seen in Figure 4-2c, R_J is inversely related to R_G, indicating that the joint stiffness parameters need to be reduced by a factor of 0.1 for every 10 times upscaling the model geometry. Note that the joint normal to shear stiffness ratio in the upscaled model is the same as that of the original model (i.e., k_n/k_s= 10).

The relationship developed in Figure 4-2c was used to modify the joint stiffness properties in the upscaled GBMs. The results shown in Figure 4-2d indicate that by using this relationship, the UCS and Young's modulus of the GBMs become independent of the model scale. Note that since the goal of this study was to investigate the strength and failure mechanisms of field-scale jointed pillars, the upscaling approach described above was used to simulate pillars at their actual sizes (i.e., 2 m by 5 m pillar model rather than 20 mm by 50 mm pillar model).

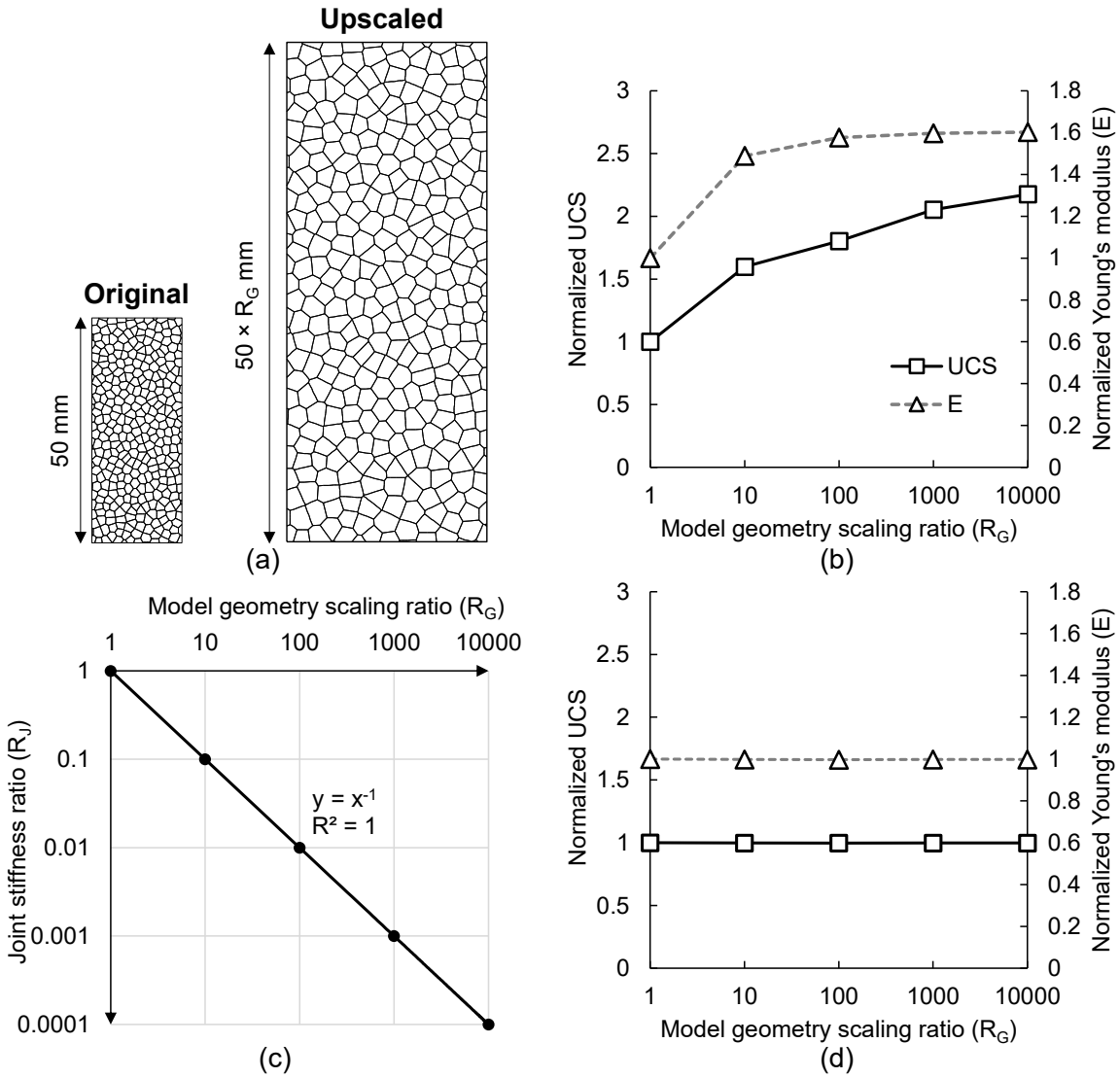

Figure 4-2: a) Schematic of original and upscaled RS2-GBMs; b) influence of model scale on UCS and Young's modulus of GBM using constant joint (normal and shear) stiffness parameters; c) relationship between joint stiffness ratio (R_J: ratio between joint normal stiffness in the upscaled model and that in the original model), and model geometry scaling ratio (R_G: ratio of the upscaled model size and the original model size); and d) influence of model scale on UCS and Young's modulus of GBM using modified joint stiffness parameters based on the relationship in c).

4.3.2. Pillar Model Specifications

Figure 4-3 shows the geometry of the pillar model constructed in RS2. This model was divided into continuum and discontinuum domains to simulate the host rock and a pillar. In the continuum domain (Figure 4-3a), the host rock was represented by an elastic homogenous material. The discontinuum domain (Figure 4-3b) was constructed using the

RS2-GBM of granulated marble calibrated in Chapter 2 and upscaled using the methodology described in the previous section. The joints in the discontinuum domain have an average length of 0.09 m, dividing the rock medium into several polygonal blocks (Figure 4-3b). A pillar height (H) of 5 m was used in all the models, and the pillar W/H ratio was varied by changing the pillar width (W). The discontinuum domains in the modeled pillars (i.e., five models with W/H ratios of 0.5, 0.75, 1, 1.25, and 1.5) were generated from a single Voronoi joint network. Therefore, the block geometries at the pillar cores were identical in all the models. Note that the entries (i.e., rooms) in the pillar models were scaled to the pillar width (W). This means that the width of the entries increases as the pillar W/H ratio increases. This was done to maintain a constant extraction ratio of 67% in all the pillar models.

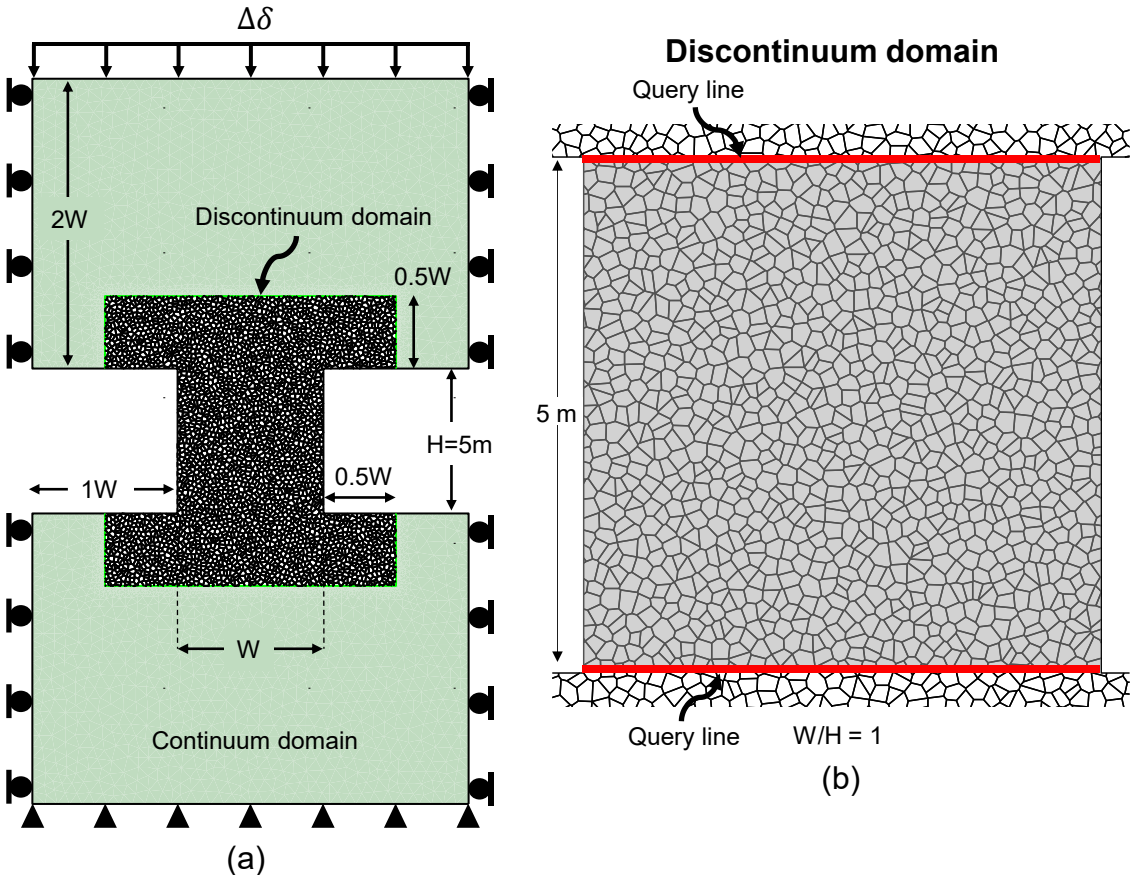

Figure 4-3: a) RS2 model geometry showing the continuum and discontinuum domains and the pillar with a W/H ratio of 1; b) closer view of the discontinuum domain showing the monitoring lines used to monitor axial displacements (red lines) and the stress measurement area (shaded in light gray) used to calculate average pillar stress.

As shown in Figure 4-3a, the continuum domain is larger than the discontinuum domain. This difference was maintained to allow for the redistribution of elastic stresses during pillar loading. The discontinuum domain was extended to above and below the pillars to allow for the propagation of block and joint yielding. The discontinuum domain was meshed with six-noded uniform triangular elements with a density of 25-27 elements per block, consistent with the GBMs developed by Li and Bahrani (2021). In the continuum domain, a six-noded graded mesh with larger elements was used to reduce the computation time. The left and right sides of the continuum domain were fixed in the horizontal direction, while the lower boundary of the model was fixed in both vertical and horizontal directions. The excavation boundaries were set to free, and a displacement boundary was applied to the top boundary of the model to load the pillar until the core yielded (see Figure 4-3a).

Figure 4-3b shows the query lines and the stress measurement area used to calculate the pillar axial strain and stress, respectively. The pillar axial stress was continuously measured by averaging axial stresses at all node locations within the pillar (shaded area in Figure 4-3b) at every loading stage. Hoek and Brown (1980) and Hudyma (1988) suggested that the average pillar stress can be calculated by averaging the stresses normal to the pillar mid-height plane. The simulation results showed that the difference between the average stress within the entire pillar area and that along the pillar mid-height plane is negligible (i.e., error < 5%). The axial strain was obtained from the difference between the average axial displacements of the upper and lower monitoring lines (red lines in Figure 4-3b) divided by the pillar height. Each monitoring line consisted of 100 equally spaced monitoring points.

The strength and elastic properties of the grains and the strength properties of the grain boundaries from the calibrated RS2-GBM of granulated marble (Li & Bahrani, 2021) were directly assigned to the rock blocks and joints in the discontinuum domain of the pillar models, respectively. According to Li and Bahrani (2021), the grains (i.e., blocks) in the RS2-GBM of granulated marble (i.e., jointed rock mass) has a UCS of 180 MPa and a Young's modulus of 80 GPa. These properties are comparable to those of hard rock pillars (e.g., Hedley & Grant, 1972; Brady, 1977; Potvin et al., 1990; Lunder & Pakalnis, 1997). The grain boundaries (i.e., joints) in the RS2-GBM of granulated marble (i.e., jointed rock

mass) were assigned nearly zero tensile strength and cohesion (i.e., 0.1 MPa), and a friction angle of 50°. It is reasonable to assume that the joints in a jointed rock mass have a tensile strength of nearly zero. The friction angle of 50° used for the grain boundaries (i.e., joints) is in fact the equivalent friction angle, consisting of a basic friction angle of 35° and a dilation angle of 15°. It should be noted that a more realistic behavior of the joints can be simulated using the non-linear Barton-Bandis criterion (Barton & Bandis, 1990) rather than the linear Mohr-Coulomb criterion that was used in this study. The joint stiffness properties (i.e., grain boundary normal stiffness and shear stiffness in RS2-GBM) were modified based on the approach described in Chapter 4.3.1 and shown in Figure 4-3c. In the calibrated RS2-GBM of granulated marble, the joint normal stiffness was 60,000 GPa/m. Since the model size was increased from 20 × 50 mm^2 to 2 × 5 m^2, the joint normal stiffness was reduced from 60,000 GPa/m to 600 GPa/m in the pillar models. The input properties for both the continuum and discontinuum domains of the RS2 pillar models are given in Table 4-1.

Table 4-1: Input properties of rock blocks and joints in the RS2 models of jointed pillars.

Domains	Input properties	Rock block	Joint
Continuum	Young's modulus	12.3 GPa	-
	Poisson's ratio	0.3	-
Discontinuum	Cohesion (peak/residual)	45/15 MPa	0.1/0.1 MPa
	Friction angle (peak/residual)	37º/37º	50º/50º
	Tensile strength (peak/residual)	14/0.1 MPa	0.1/0.1 MPa
	Young's modulus	80 GPa	-
	Poisson's ratio	0.3	-
	Normal stiffness	-	600 GPa/m
	Shear stiffness	-	60 GPa/m

4.4. SIMULATION RESULTS

4.4.1. Elastic Analyses

Elastic models (i.e., elastic properties for both rock blocks and joints) were first used to investigate the influences of rock mass geometric heterogeneity and pillar size on tensile stresses generated within the pillars and the evolution of stresses at the pillar core during pillar loading. Figure 4-4 presents the spatial distribution of tensile stresses within the pillars with the W/H ratios of 0.5, 1, and 1.5 at the pillar peak stress obtained from inelastic models. It was found that the tensile stresses are mainly concentrated around the subvertical joints at the early stages of pillar loading and then extended across the rock blocks as the pillar load increases.

As shown in Figure 4-4a, most of the area in the slender pillar (i.e., W/H = 0.5) is under tension. However, the tensile stresses are mainly concentrated near the walls of the wider pillars (i.e., W/H = 1 and 1.5). In other words, the portion of the pillar area experiencing tension is smaller in wider pillars compared to the slender pillars. Further analysis of the tensile stress distribution in Figure 4-4 reveals that the magnitudes of tensile stresses near the walls of the pillar with the W/H ratio of 1.5 are higher than those in the pillars with the W/H ratios of 1.0 and 0.5. This is because the stress contours in these models are shown at stress levels corresponding to the peak stresses of their inelastic models (i.e., σ_1 = 21 MPa, 65 MPa, and 122 MPa in pillar W/H = 0.5, 1.0, and 1.5, respectively). Since the models shown in Figure 4-4 are elastic, localized stress redistribution due to joint and finite element yielding is not captured. This resulted in higher localized tensile stresses in wider pillars.

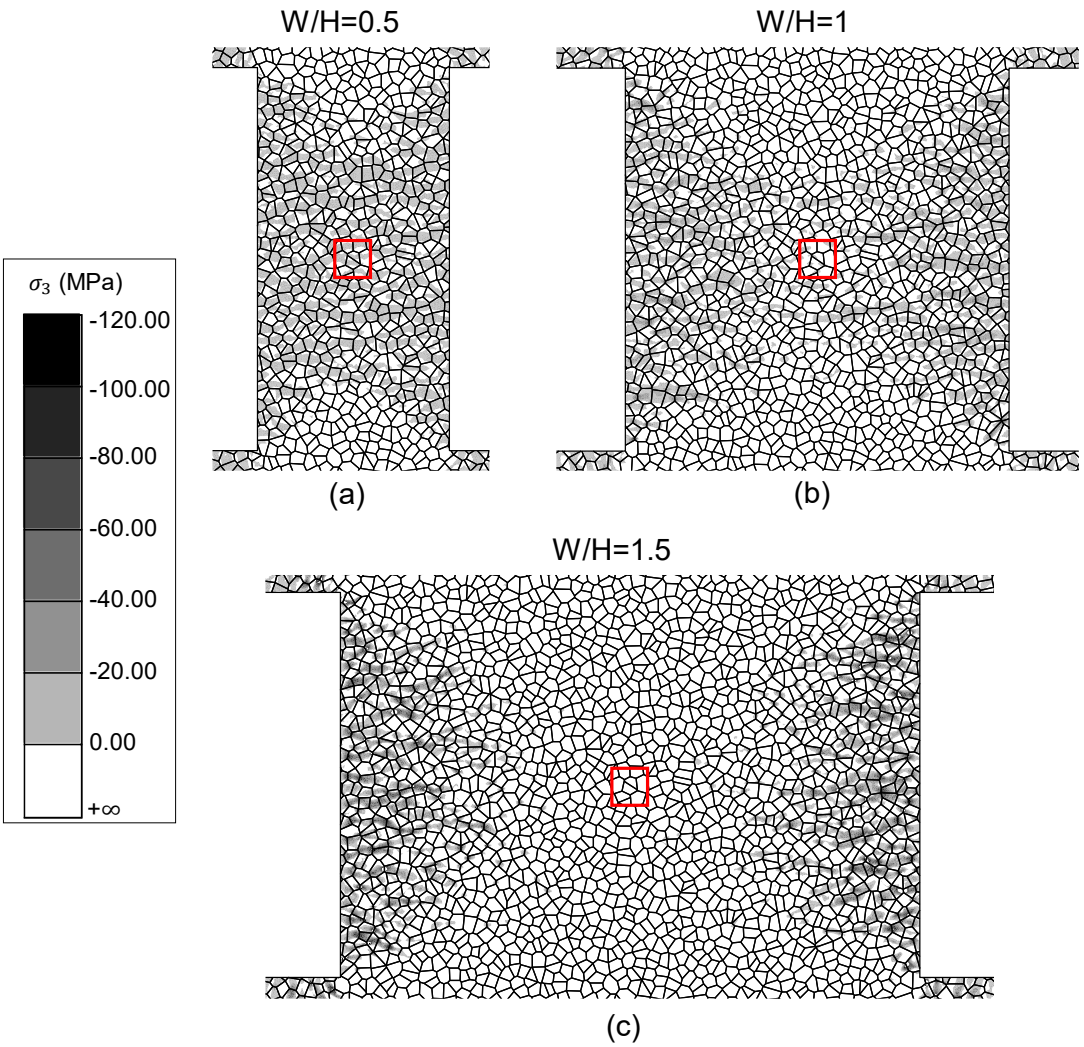

Figure 4-4: Tensile stress contours (i.e., $\sigma_3 < 0$) at the peak stress for the pillar W/H ratios of: a) 0.5; b) 1; and c) 1.5. A 0.5 × 0.5 m^2 area indicated by the red box was used to analyze the stress evolution during pillar loading in Figure 4-5.

Figure 4-5 illustrates the scatter of stresses at the core of the modeled pillars with the W/H ratios of 0.5, 1.0, and 1.5 at their peak loading stages. The core areas within which the stresses were extracted are shown with red boxes in Figure 4-4. As shown in Figure 4-5, the scatter of node stresses at the pillar core increases as the pillar W/H ratio increases from 0.5 to 1.5. The node stresses at the pillar core shift from the initial stress state (i.e., $\sigma_1 = \sigma_3 = 0$ MPa) to the right in the compression zone during pillar loading. In the slender pillar (i.e., W/H = 0.5), nearly half of the pillar core is under tension (i.e., 48.5%), whereas only 3.6% of the core experiences tension in the wide pillar (i.e., W/H = 1.5). In the pillar with the W/H ratio of 1, 17.5% of the nodes at the pillar core are under tension.

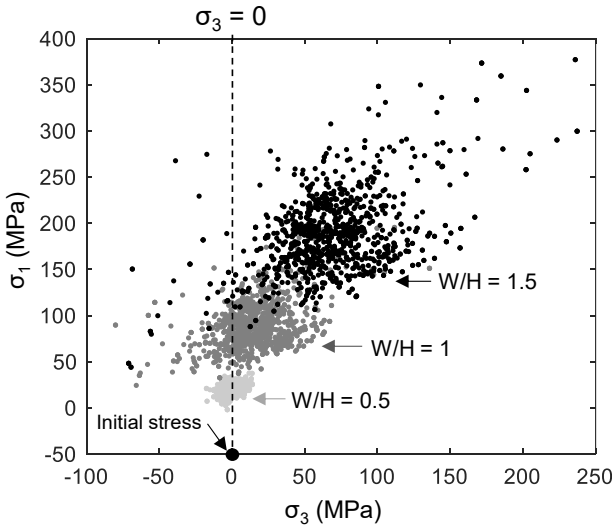

Figure 4-5: Scatter of pillar core node stresses at pillar peak loading stages. The dashed line divides the tension ($\sigma_3 < 0$) and compression ($\sigma_3 > 0$) zones. The core area within which the node stresses were extracted are indicated by red boxes in Figure 4-4.

Figure 4-6 summarizes the percentages of finite element nodes and joint element segments experiencing tension within the entire pillar area (shaded area in Figure 4-3b). Note that a joint element segment is under tension when the induced normal stress is less than zero (i.e., $\sigma_n < 0$). This figure shows how the percentage of node stresses under tension decreases from 37.9% to 17.8% as the pillar W/H ratio increases from 0.5 to 1.5. Similarly, the percentage of joint element segments under tension decreases from 17.0% to 9.5% as the pillar W/H ratio increases from 0.5 to 1.5.

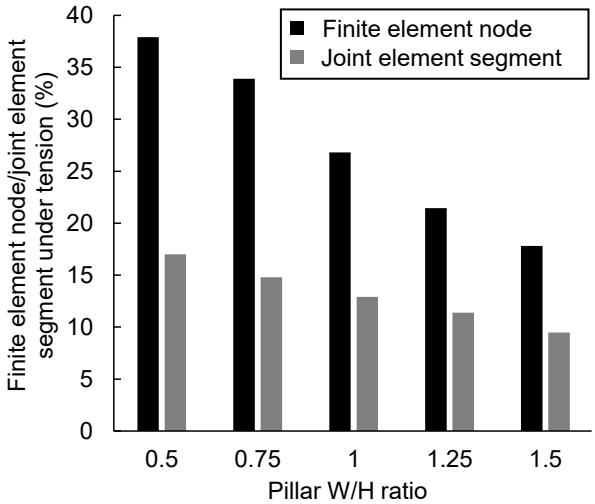

Figure 4-6: Influence of pillar W/H ratio on nodes (in %) and joint element segments (in %) under tension in elastic pillar models.

The results of elastic analyses presented in this section demonstrated the impact of pillar W/H ratio on the distribution of tensile stresses near the sidewalls and at the pillar core. It was found that even the highly confined pillar core (i.e., the core of pillar with the W/H ratio of 1.5) experiences tension due to the influence of geometric heterogeneities. This inference is consistent with the findings of Sinha and Walton (2020) and Li and Bahrani (2021), who showed that tensile stresses leading to tensile cracking are still formed within a laboratory specimen at high confining pressures.

4.4.2. Inelastic Analyses

Inelastic models (i.e., inelastic properties for both rock blocks and joints) were used to better understand the failure process and estimate the strength of pillars of various W/H ratios. Figure 4-7a illustrates the stress-strain curves for five models with W/H ratios ranging from 0.5 to 1.5. The stress-strain curves of the pillars exhibit a plastic response. These findings are not consistent with the results of previous numerical studies conducted by Mortazavi et al. (2009), Rafiei Renani and Martin (2018), and Sinha and Walton (2018). These studies inferred that the post-peak response of pillars gradually changes from brittle in slender pillars to ductile in wide pillars. This inconsistency is considered a limitation of the RS2-GBM approach, which will be discussed in more detail later in this chapter. In addition, Figure 4-7b shows the pillar peak stress normalized to the UCS of the intact rock block (i.e., 180 MPa) for different pillar W/H ratios. As illustrated in this figure, the PSC for the simulated highly interlocked jointed pillars is almost linear.

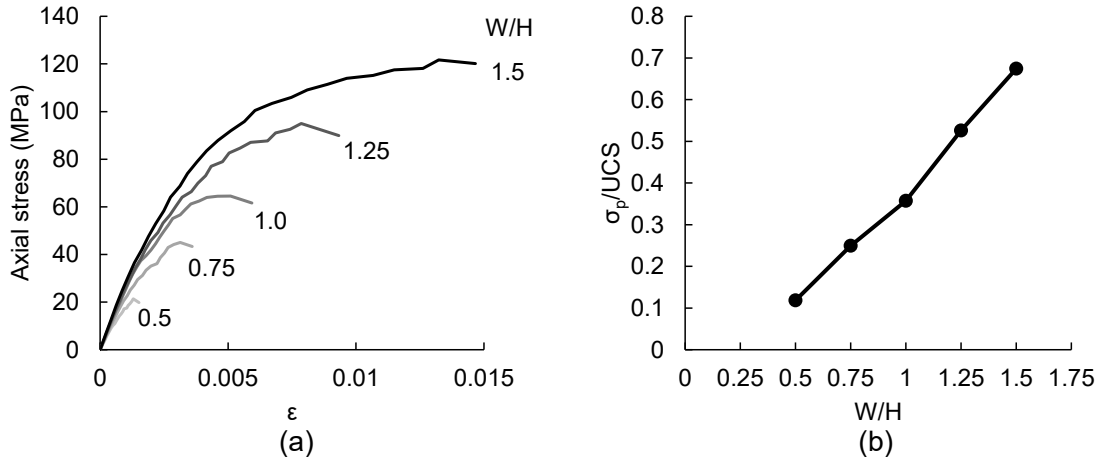

Figure 4-7: a) Stress-strain curves of modeled pillars with W/H ratios of 0.5, 0.75, 1, 1.25, and 1.5; and b) pillar stability curve obtained from RS2 pillar models.

Figure 4-8 illustrates the progressive failure of pillars with the W/H ratios of 0.5, 1, and 1.5 at 35%, 85%, and 100% of the pillar peak stress (i.e., σ_p), and the first loading stage in the post-peak region. In the pillar with a 0.5 W/H ratio, most of the joints are observed to yield at early loading stages (i.e., < 35% σ_p), while only a few yielded blocks can be seen past the peak stress. This observation is consistent with the study conducted by Elmo and Stead (2010), who indicated that the strength of slender pillars is controlled by the presence of pre-existing discontinuities. In the pillar with a W/H ratio of 1, yielded joints are oriented parallel to the loading direction and appear at early loading stages (i.e., < 35% σ_p). These yielded joints interact with each other and coalesce to generate relatively long slabs near the pillar walls. The yielded joints at the pillar core are shorter compared to those near the pillar walls. This is due to the higher induced confinement at the pillar core than that near the pillar walls. As the pillar load increases, block yielding propagates from the pillar walls towards the core until the core ultimately yields in the post-peak loading stage. This condition resembles "crushed" pillars observed in hard rock mines. A similar failure process can be seen in the modeled pillar with a W/H ratio of 1.5. However, the mode of block yielding at the core in this pillar is different from those in the pillars with the W/H ratios of 0.5 and 1.

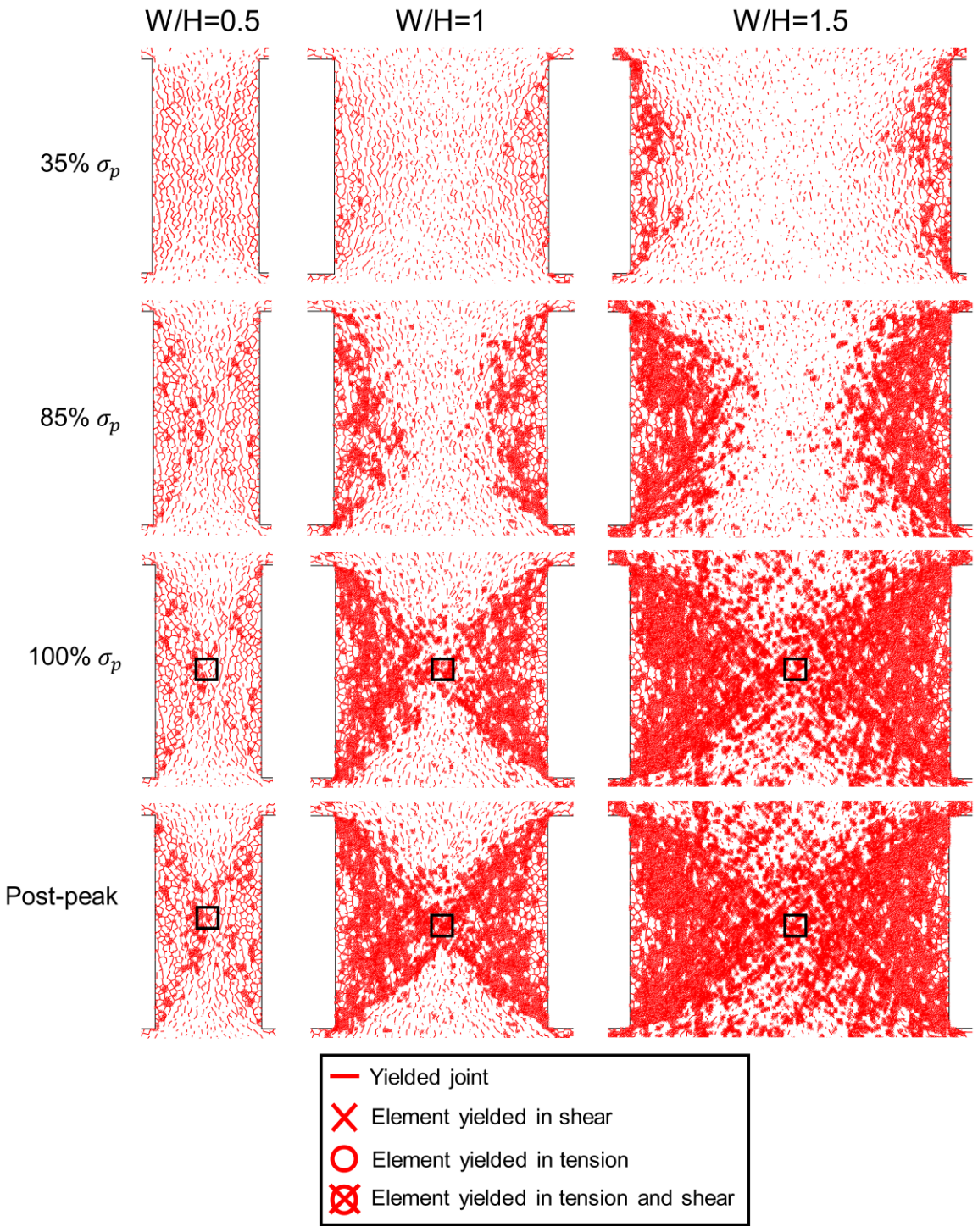

Figure 4-8: Simulated failure processes of pillars with the W/H ratios of 0.5, 1, and 1.5. Closer views of the pillar failure mode within the boxed areas are illustrated in Figure 4-9.

Closer views of the failure modes at the pillar core (boxed areas in Figure 4-8) in the peak and post-peak loading stages are illustrated in Figure 4-9. As shown in this figure, the lengths and the number of yielded joints at the pillar core decrease as the pillar W/H ratio

increases. The mode of element yielding at the core of the pillar with the W/H ratio of 0.5 is combined tension-shear. This finding is consistent with the failure mode of the GBM of granulated marble under unconfined compression, as described in Chapter 3. With the increase in the pillar W/H ratio to 1.5, the mode of element yielding at the core changes to pure shear. Only a few elements yielded in the combined tension-shear can be found at the core of the pillar with the 1.5 W/H ratio (Figure 4-9c). The failure mode at the core of this pillar is consistent with that of the GBM of granulated marble at high confinement (i.e., σ_3 = 34.47 MPa), as described by Li and Bahrani (2021).

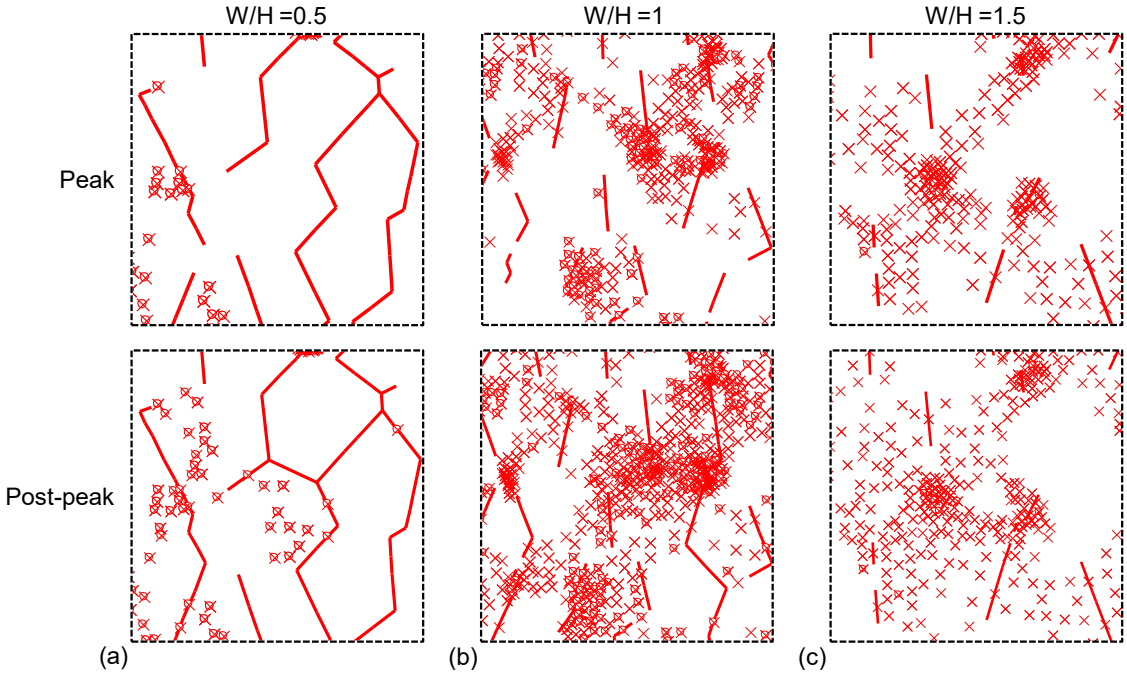

Figure 4-9: Closer views of the boxed areas in Figure 4-8 showing the failure modes in the peak and post-peak loading stages of the pillar with the W/H ratios of: a) 0.5; b) 1; and c) 1.5.

Figure 4-10 shows the average confinement within the modeled pillars (shaded area in Figure 4-3) and the distributions of minimum and maximum principal stresses along the mid-height of the pillar models at their peak stresses. As seen in Figure 4-10a, the average confinement for the pillar with the 0.5 W/H ratio is close to zero, it increases non-linearly with an increase in the pillar W/H ratio and reaches about 27 MPa in the pillar with the W/H ratio of 1.5. In Figure 4-10b, the confinement near the pillar walls is nearly zero in all three pillar sizes. As expected, the confinement at the pillar core is higher in the pillar with the W/H ratio of 1.5 than that with the W/H ratio of 1.0. The confinement is nearly zero at

the core of the slender pillar (i.e., W/H = 0.5). Note that σ_3 in Figure 4-10b, is in fact the effective confining pressure resulting from the Poisson's effect. Other factors such as the presence of joints, as well as block and joint yielding also affected the magnitudes of σ_3 within the pillar.

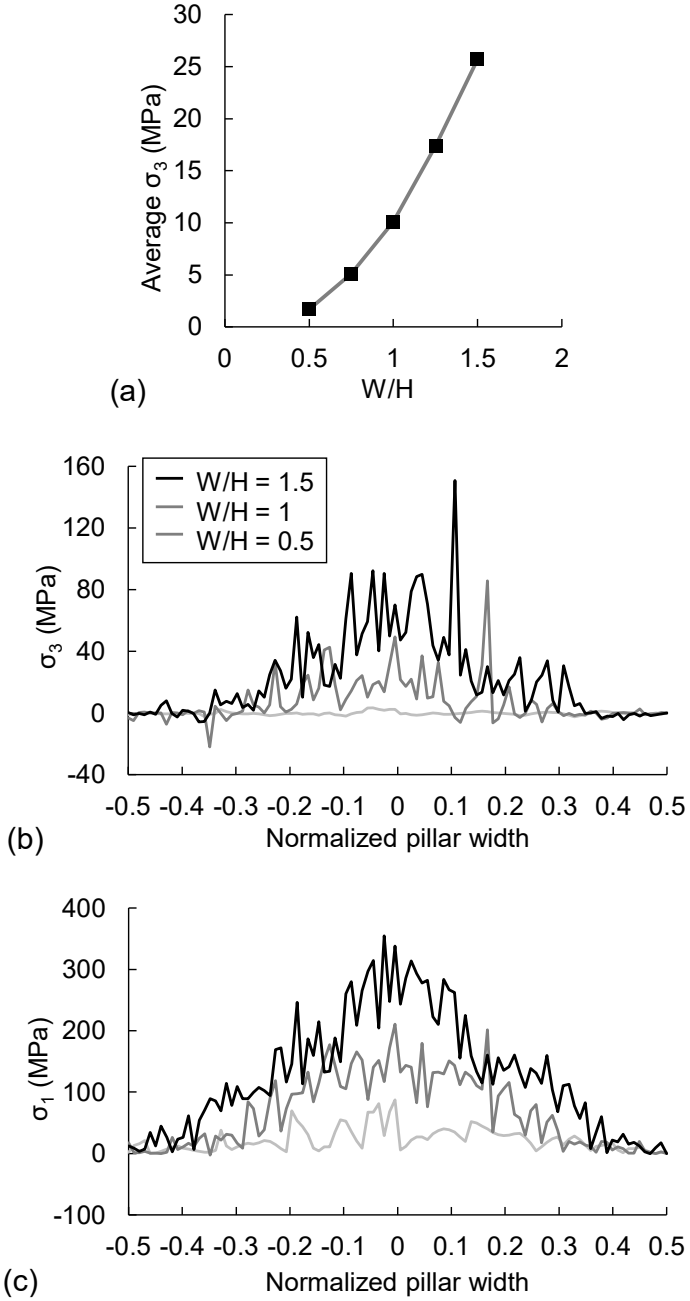

Figure 4-10: a) Average confining pressure (σ_3) within modeled pillars as a function of pillar W/H ratio; and distributions of: b) σ_3 and c) σ_1 along the mid-height of modeled pillars with the W/H ratios of 0.5, 1, and 1.5.

Figure 4-10c compares the distributions of σ_1 along the mid-height of the modeled pillars with the W/H ratios of 0.5, 1.0, and 1.5. This figure shows that σ_1 is almost zero near the pillar walls and increases towards the pillar core in all the three pillar models. This suggests that the blocks near the pillar walls have a negligible impact on the overall strength of the modeled pillars. In the slender pillar (i.e., W/H = 0.5), some areas of high-stress concentration can be identified near the pillar core. In the wider pillars (i.e., W/H = 1.0 and 1.5), σ_1 increases rapidly and more systematically towards the pillar core. Both Figure 4-10b and c illustrate that the stress magnitudes at the cores are higher in comparison to those near the walls in the wider pillars (e.g., W/H = 1.5). This is believed to affect the overall strength of the wider pillars resulting in a steep PSC, as shown in Figure 4-7.

4.4.3. Pillar Stability Curve (PSC)

In this section, the PSC of modeled pillars is compared with those of jointed pillars from existing continuum and discontinuum models. As shown in Figure 4-11, the slope of the PSC of modeled pillars from this study is steeper than those of joined pillars simulated by continuum (Martin & Maybee, 2000) and discontinuum (Elmo & Stead, 2010) models. It can be seen in this figure that the strength of the slender pillar (i.e., W/H = 0.5) in this study is close to those with the GSI value of 60 (Martin & Maybee, 2000) and the P_{21} value of 2.6 (Elmo & Stead, 2010). The failure mode of the simulated slender pillar is also consistent with those of discontinuum models by Elmo and Stead (2010), who demonstrated that the behavior of slender pillars is predominantly influenced by the presence of discontinuities. Figure 4-11 demonstrates how the strength of highly interlocked jointed pillars increases as the pillar W/H ratio increases and approaches that represented by the GSI value of 80 for the pillar W/H of 1.5.

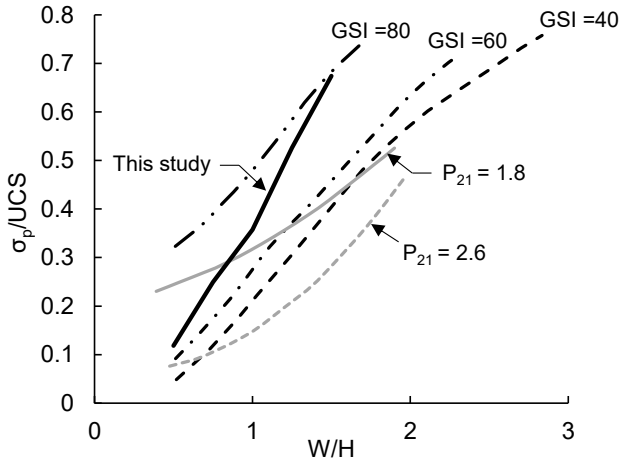

Figure 4-11: The PSC in this study compared to those obtained from continuum (Martin and Maybee, 2000) and discontinuum (Elmo and Stead, 2010) models of jointed pillar.

This rapid strengthening of highly interlocked jointed pillars resulting in a steep PSC is consistent with the strength envelope of jointed rock mass analogue (Figure 4-1), which is represented by GSI values of 63 and 76 under unconfined and confined conditions, respectively. The higher slope of the PSC in this study compared to those of jointed pillars by Elmo and Stead (2010) (i.e., PSCs for P_{21} = 1.8 and 2.6) can be attributed to the difference between the degrees of block interlock in the two jointed rock masses. In the jointed pillars simulated by Elmo and Stead (2010), the joints were relatively long, critically oriented and had a friction angle of 35°, whereas the joints in the highly interlocked jointed pillars are relatively short, randomly oriented and have an equivalent friction angle of 50°. The difference between the PSCs presented in Figure 4-11 demonstrates the impact of the degree of block interlock on the strength of jointed pillars and offers a promising avenue for further research.

4.5. DISCUSSION

4.5.1. Post-Peak Behavior

The results of numerical simulations of hard rock pillars using continuum models by Mortazavi et al. (2009), Rafiei Renani and Martin (2018), and Sinha and Walton (2018), demonstrated that the post-peak behavior of hard rock pillars transforms from brittle in slender pillars to strain-hardening in wide pillars. However, this behavior was not captured

by the modeled pillars in this study (see Figure 4-7a). As discussed by Li and Bahrani (2021), this is mainly due to the kinematic assumptions and formulations of joint elements in the FEM, representing the thermally-damaged grain boundaries in the GBM of granulated marble and frictional discontinuities in the upscaled GBMs of pillars. As discussed by Riahi et al. (2010), in the FEM, the interconnectivity between the solid (block) and the joint element remains unchanged throughout the solution process, despite the displacement that occurs. Therefore, the detachments of blocks (finite elements) at their boundaries (joint elements) and associated stress redistributions are not captured in the RS2-GBM with frictional joints (Li and Bahrani, 2021). This resulted in plastic response in the GBM of granulated marble independent of confinement, as shown in Figure 3-18b, and modeled pillars independent of the pillar W/H ratio, as shown in Figure 4-7a.

It should be noted that since the continuum GBM cannot explicitly capture the detachment of rock blocks from their frictional boundaries and associated stress redistribution, which could result in further fracturing leading to the pillar core failure at a lower applied load, it is postulated that the strength of wide pillars is overestimated. This in combination with the plastic response of the rock blocks near the core of wider pillars, could have contributed to the estimated PSC, which is steeper than those of jointed pillars simulated using the hybrid finite-discrete element method by Elmo and Stead (2010). Therefore, further research on the progressive failure and strength of highly interlocked jointed pillars using discontinuum methods is warranted.

4.5.2. Progressive Damage and Failure Mechanism

Several researchers developed different pillar stability classification systems (e.g., Esterhuizen et al., 2006; Lunder & Pakalnis, 1997; Pritchard & Hedley, 1993) to evaluate the pillar performances in hard rock mines through assessing the pillar failure modes at various stress levels. These classification systems present several commonalities in terms of the pillar failure processes, as summarized below:

- First, fracturing initiates at the corners of the pillar and propagates parallel to the pillar walls. This leads to spalling and slabbing of the pillar walls.

- Then, the fractures caused by the spalling process extend to the pillar core, resulting in an "hour-glass" shaped pillar (i.e., the width at the mid-height of the pillar is less than its original width).
- Finally, the fractures coalesce at the pillar core leading to a "crushed" pillar condition.

The progressive failure of hard rock pillars has been simulated in continuum programs by Rafiei Renani and Martin (2018) using the non-linear strain-dependent CWFS model, and by Sinha and Walton (2018) using the progressive S-shaped criterion. Figure 4-12 compares the failure process of a jointed pillar with a W/H ratio of 1 simulated using a heterogeneous continuum model (i.e., upscaled RS2-GBM in this study; Figure 4-12a) with those by Rafiei Renani and Martin (2018) (Figure 4-12) and Sinha and Walton (2018) (Figure 4-12c), in which the massive rock mass was simulated as a homogeneous material.

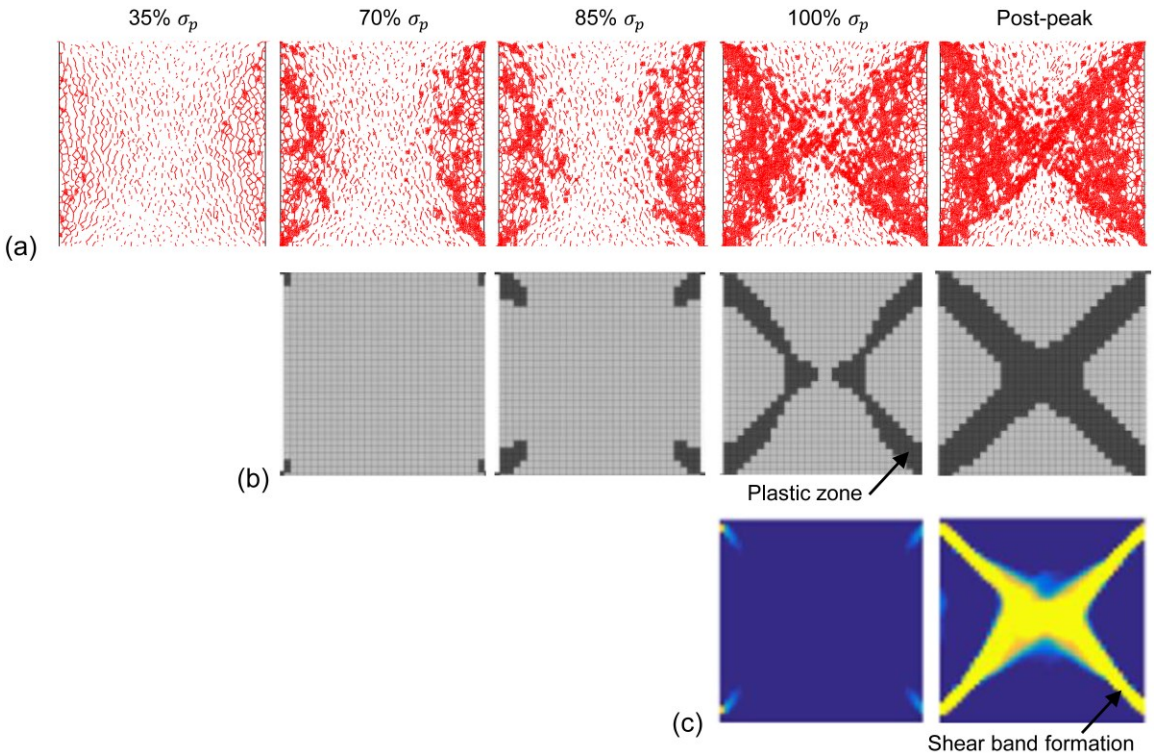

Figure 4-12: Comparison between failure process of pillars with a W/H ratio of 1 simulated using different continuum models: a) heterogeneous continuum model (i.e., upscaled RS2-GBM); b) homogeneous continuum model (i.e., FLAC3D) with non-linear CWFS by Rafiei Renani and Martin (2018); and c) homogeneous continuum model (i.e., FLAC3D) with progressive S-shaped yield criterion by Sinha and Walton (2018).

In the pillar simulated using the upscaled GBM (Figure 4-12a), the damage near the pillar walls (i.e., yielded joints) was noticed to occur at early loading stages (i.e., < 35% σ_p). The yielded joints interact with each other and coalesce to generate relatively long slabs. The simulated failure process at the pillar walls show resemblance to the progressive spalling and slabbing observed in hard rock pillars as described by Pritchard and Hedley (1993), Lunder and Pakalnis (1997), and Esterhuizen et al. (2006). As the pillar load increases, the rock block yielding initiates near the walls (i.e., at 35% σ_p in Figure 4-12a) and propagates towards the pillar core (at 35% - 100% σ_p in Figure 4-12a). This process results in an "hour-glass" shaped pillar. In the post-peak stage, the yielded rock blocks coalesce at the pillar core, a condition which is similar to a "crushed" pillar observed in the field.

Figure 4-12b and c show the failure processes of massive hard rock pillars simulated by Rafiei Renani and Martin (2018; Figure 4-12b) and Sinha and Walton (2018; Figure 4-12c). In these models, the failure initiates from the corners of the pillars at about 70% (Figure 4-12b) and 100% (Figure 4-12c) of the pillar peak stress. As the pillar load increases, yielding propagates towards the pillar core. In the post-peak loading stages, the yielded zones coalesce to create conjugate shear bands, representing a "crushed" pillar condition. However, the tensile damage near the pillar walls leading to subsequent spalling and slabbing, which is expected to occur at earlier loading stages was not captured by these models. This is due to the lack of heterogeneities and associated localized tensile stresses in these models, causing shear failure of the rock mass even in slender pillars, where the confinement is relatively low. The results of numerical simulations using the hybrid finite-discrete element method as studied by Elmo and Stead (2010) and Li et al. (2019) confirm the effect of heterogeneities on the progressive failure process of hard rock pillars, including the formation of tensile fractures leading to spalling of the pillar walls and shear failure at the pillar core.

According to Cai (2011) and Bewick et al. (2019), spalling in massive to moderately jointed rock masses occurs at about 30-50% of the intact rock UCS near underground excavations. However, spalling was found to occur at much lower stress in the pillars simulated using the upscaled RS2-GBM (Figure 4-12a). This is due to the fact that the rock mass simulated in this study is highly jointed, and therefore, spalling was observed to occur

due to the tensile yielding of the joints rather than yielding of the intact rock. For this reason, the spalling strength in this rock mass should not be compared with that of massive to moderately jointed rock masses. It is expected that the spalling strength increases as the joint persistence decreases, and eventually reaches that of massive rock masses (i.e., 30-50% of intact UCS). A comprehensive study on the influence of joint persistence on the strength of jointed hard rock masses was conducted by Bahrani and Kaiser (2020). Their investigations demonstrated that the unconfined and confined strengths of jointed rock masses increase with the decrease in the joint persistence. In the future, similar analyses should be conducted to investigate the influence of joint persistence on the spalling strength, the overall pillar strength, and the failure mechanisms of jointed pillars.

4.6. SUMMARY

This chapter investigated the strength and failure mechanisms of highly interlocked jointed pillars using an upscaled continuum GBM, previously calibrated to the properties of granulated Wombeyan marble. The granulated marble was considered representative of an analogue for a highly interlocked jointed rock mass.

The results of elastic pillar models showed that tensile stresses are generated across the entire width of the slender pillar (i.e., W/H = 0.5) and are mainly concentrated near the walls of wider pillars (i.e., W/H = 1 and 1.5). The simulation results using inelastic models indicated that the failure mode of the slender pillar is dominated by the yielding of the joints. In the wider pillars, the failure is initiated by the yielding of the joints near the pillar walls at relatively low pillar stress (i.e., < 35% σ_p), followed by the yielding of the rock blocks, which propagates towards the pillar core with the increase in the pillar load.

The Pillar Stability Curve (PSC) obtained from the results of inelastic pillar models was found to be steeper in comparison to those of jointed pillars from existing continuum and discontinuum numerical simulations. The investigations demonstrated that this modeling approach (i.e., GBM with frictional joints) is unable to capture the transition in the post-peak response from brittle behavior in slender pillars to strain-hardening in wide pillars. However, the approach captures a more realistic failure process (i.e., tensile damage

leading to spalling near the pillar walls and shear failure at the pillar core) compared to other continuum models in which the rock mass was simulated as a homogenous material.

The modeling results presented in this chapter offer a first contribution in assisting a better understanding of the strength and failure mechanisms of highly interlocked jointed pillars. It is recommended that future studies should focus on the influence of factors contributing to the degree of block interlock in a jointed rock mass, such as the joint persistent, joint roughness, block shape, and block size on the strength and failure mechanisms of pillars of various W/H ratios.

CHAPTER 5 SUMMARY, CONCLUSIONS AND RECOMMANDATIONS FOR FUTURE RESEARCH

5.1. SUMMARY

In this research, a continuum Grain-based Model (GBM) was developed using the 2D numerical program *RS2* to simulate an analogue for a highly interlocked jointed rock mass and investigate the strength and failure mechanisms of jointed rib pillars. In Chapter 1, it was discussed that the highly interlocked jointed rock mass represents an extreme case of a jointed rock mass, in terms of degree of interlock between its constituent rock blocks. Furthermore, it was discussed that the Hoek-Brown failure criterion based on the GSI system (i.e., HB-GSI) tends to underestimate the confined strength of massive to moderately jointed rock masses. Therefore, the pillar design in such rock masses based on the HB-GSI approach could lead to oversized pillars due to underestimating the rock mass strength at the pillar core, especially in wider pillars. The central objective of this research was to investigate the strength and failure mechanisms of highly interlocked jointed pillars. The following two steps were taken to achieve this objective:

Step 1: An RS2-GBM was developed and calibrated to the laboratory properties of intact and granulated Wombeyan marble reported by Gerogiannopoulos (1976):

In the RS2-GBM, the grains were simulated as a homogeneous medium consisting of several six-noded triangular finite elements, and the grain boundaries were simulated using four-noded quadrilateral joint elements. In the simulations of Wombeyan marble, several assumptions were made as briefly described below:

- The cohesive bond between the grains was destroyed during the heating process;
- Heating did not affect the friction angle of the grain boundaries;
- Heating did not affect the strength and elastic properties of the grains;
- Open cracks induced by the heating process was not simulated.

In other words, the strength and elastic properties of the grains in the models of intact and granulated marble specimens were assumed to be the same. The grain boundaries of intact marble were assumed to be cohesive, while those of granulated marble were purely

frictional. Based on these assumptions, an iterative process for calibrating the GBM to the laboratory properties of both intact and granulated Wombeyan marble was developed. The simulation results (i.e., strength envelope and failure mode) of the RS2-GBMs were compared with those of laboratory tests (i.e., Paterson, 1958; Rosengren & Jaeger, 1968; and Gerogiannopoulos, 1976) as well as the simulation results of PFC-GBM by Bahrani et al. (2014).

Step 2: An approach was developed to upscale the RS2-GBM of granulated marble to a field scale rock mass specimen and simulate jointed pillars of various W/H ratios:

The granulated marble has been suggested to serve as an analogue for a highly interlocked jointed rock mass. In this model, the grains and grain boundaries are analogues for rock blocks and joints, respectively. This means that the strength and elastic properties of the jointed rock mass should be the same as those of granulated marble. For this purpose, the joint normal (and shear) stiffness parameters were modified in the upscaled model in such a way to be the same as the strength and deformation properties of the original model (see the procedure details in Chapter 4). The upscaled model of granulated marble was then used to simulate jointed rib pillars of various W/H ratios.

The strength of modeled pillars (normalized to the UCS of intact rock) was plotted as a function of pillar W/H ratio to create a Pillar Stability Curve (PSC), which was then compared to the PSCs obtained from continuum and discontinuum numerical models of jointed pillars. The limitations and advantages of this modeling approach, in terms of the pillar peak strength, failure mode and post-peak response compared to other continuum modeling approaches were discussed.

5.2. CONCLUSIONS

The following conclusions were emerged from the simulations of intact and granulated Wombeyan marble and jointed pillars:

- Effect of grain-scale heterogeneity on stress variation and tensile stress generation

The results of simulations using elastic RS2-GBMs showed that grain-scale heterogeneities (i.e., grain geometric and grain boundary orientation heterogeneities) control the variation of stresses within a specimen during compressive loading. It is concluded that the grain-scale heterogeneity leads to the generation of tensile stresses within a specimen (i.e., within the grains and on the grain boundaries) even at high confinement. When the magnitudes of tensile stresses exceed the tensile strength of the grains and grain boundaries, tensile damage occurs. This usually happens at early stages of compressive loading before the peak stress is reached.

- RS2-GBM of intact Wombeyan marble

The simulation results using the RS2-GBM calibrated to the properties of intact Wombeyan marble indicated that the grain boundary yielding mainly occurs during pre-peak loading stages, while grain yielding dominates the failure in the post-peak region. It was shown that the RS2-GBM calibrated to the peak strength of intact marble could capture the observed post-peak response and failure modes at different levels of confinement.

- RS2-GBM of granulated Wombeyan marble

The RS2-GBM well captured the non-linear strength envelope of the granulated marble (i.e., highly interlocked jointed rock mass analogue). Although the failure modes of RS2-GBMs of granulated marble were found to be consistent with those of previously calibrated PFC-GBM, the calibrated RS2-GBMs exhibited a plastic post-peak response, independent of the level of confinement. This is interpreted to be due to the gradual yielding of a few grains in the post-peak region and the inability of the RS2-GBM in capturing grain detachment from their frictional boundaries that occurred in the post-peak loading stages of granulated marble. Apart from this limitation, it is suggested that RS2-GBM can be used as a practical tool to simulate jointed rock masses because of its much shorter computation time compared to discontinuum modeling approaches.

- Simulation of jointed rib pillars using elastic models

The results of elastic pillar models showed that tensile stresses are generated across the entire width of the slender pillar (i.e., W/H = 0.5), whereas they are mainly concentrated

near the walls of wider pillars (i.e., W/H = 1 and 1.5). The confining pressure at the pillar core increases with increasing the pillar W/H ratio. This suggests the importance of reliable estimation of confined rock mass strength when designing pillars.

- Simulations of jointed rib pillars using inelastic models

The simulation results using inelastic models indicated that the failure mode of the slender pillar (i.e., W/H = 0.5) is dominated by the yielding of the joints. In wider pillars (i.e., W/H = 1 and 1.5), the failure is initiated by the yielding of joints near the pillar walls at a relatively low pillar stress (i.e., < 35% σ_p), followed by the yielding of rock blocks, which propagates towards the pillar core as the pillar load increases. The failure process of modeled pillars is consistent with those observed in the field. It was suggested that this approach captures a more realistic failure process (i.e., tensile damage leading to spalling near the pillar walls and shear failure at the pillar core), compared to other continuum models in which the rock mass is simulated as a homogenous material.

- Pillar Stability Curve (PSC)

It was highlighted that the PSC obtained from this research should be compared to PSCs of jointed pillars. The PSC obtained from the inelastic pillar models was found to be steeper than those of jointed pillars simulated using continuum and discontinuum numerical programs (Martin & Maybee, 2000; Elmo & Stead, 2010).

5.3. RECOMMENDATIONS FOR FUTURE RESEARCH

The following provides some recommendations for future research to further advance the understanding of the failure mechanisms and strength of pillars in highly interlocked jointed rock masses:

- Discontinuum modeling of jointed pillars:

In this study, numerical simulations of jointed pillars were conducted using the continuum program *RS2*. It was discussed that the detachment of rock blocks near the pillar walls leading to spalling and slabbing at earlier loading stages was not captured. Further analyses

of jointed pillars should be undertaken using discontinuum programs to more realistically capture the failure processes of highly interlocked jointed pillars.

- 3D modeling of jointed pillar:

As discussed in Chapter 4, the PSC obtained from the modeled pillars was for jointed rib pillars. In such pillars, the length is much greater than the width (L >> W). According to Dolinar and Esterhuizen (2007), the length of the pillar has some effects on the strength of wider pillars. Therefore, future simulations of highly interlocked jointed pillars should be conducted using 3D numerical programs to better understand how the pillar length affects the pillar strength.

- Degree of interlock:

As discussed by Bahrani and Kaiser (2020), a jointed rock mass with Voronoi rock blocks, such as columnar basaltic rock masses, is an extreme case of a jointed rock mass in terms of the degree interlock between the rock blocks. A more comprehensive study on how to the degree of interlock can be quantified and how it affects the confined rock mass strength should be conducted. It is expected that jointed rock masses with lower degrees of rock block interlock will have lower confined strength. Therefore, further studies on the influence of degree of rock block interlock on the strengths and failure mechanisms of jointed pillars is recommended.

- Joint persistence:

The models of granulated marble presented in this thesis and by Bahrani and Kaiser (2020) represent an analogue for a highly interlocked jointed rock mass with 100% joint persistence. Further analyses can be conducted to investigate how joint persistence affect the strength and failure mechanisms of mine pillars.

REFERENCES

Abdelaziz, A., Zhao, Q., & Grasselli, G. (2018). Grain based modelling of rocks using the combined finite-discrete element method. *Computers and Geotechnics*, *103*(July), 73–81. https://doi.org/10.1016/j.compgeo.2018.07.003.

Baecher, G. B., Lanney, N. A., & Einstein, H. H. (1977). Statistical description of rock properties and sampling. *18th U.S. Symposium on Rock Mechanics, USRMS 1977*.

Bahrani, N., Valley, B., Kaiser, P. K., & Pierce, M. (2011). Evaluation of PFC2D Grain-Based Model for simulation of confinement-dependent rock strength degradation and failure processes. *45th US Rock Mechanics / Geomechanics Symposium*.

Bahrani, N. (2015). *Estimation of confined peak strength for highly interlocked jointed rockmasses*. Laurentian University of Sudbury.

Bahrani, N., & Hadjigeorgiou, J. (2018). Influence of Stope Excavation on Drift Convergence and Support Behavior: Insights from 3D Continuum and Discontinuum Models. *Rock Mechanics and Rock Engineering*. https://doi.org/10.1007/s00603-018-1482-5.

Bahrani, N., & Kaiser, P. K. (2013). Strength degradation of non-persistently jointed rockmass. *International Journal of Rock Mechanics and Mining Sciences*, *62*, 28–33. https://doi.org/10.1016/j.ijrmms.2013.03.013.

Bahrani, N., & Kaiser, P. K. (2016). Numerical investigation of the influence of specimen size on the unconfined strength of defected rocks. *Computers and Geotechnics*, *77*, 56–67. https://doi.org/10.1016/j.compgeo.2016.04.004.

Bahrani, N., & Kaiser, P. K. (2020). Influence of degree of interlock on confined strength of jointed hard rock masses. *Journal of Rock Mechanics and Geotechnical Engineering*. https://doi.org/https://doi.org/10.1016/j.jrmge.2020.06.004.

Bahrani, N., Kaiser, P. K., & Valley, B. (2014). Distinct element method simulation of an analogue for a highly interlocked, non-persistently jointed rockmass. *International Journal of Rock Mechanics and Mining Sciences*, *71*, 117–130. https://doi.org/10.1016/j.ijrmms.2014.07.005.

Barton, N., Lien, R., & Lunde, J. (1974). Engineering classification of rock masses for the design of tunnel support. *Rock Mechanics Felsmechanik Mécanique Des Roches*. https://doi.org/10.1007/BF01239496.

Barton, N. R., & Bandis, S. C. (1990). Review of predictive capabilities pf JRC-JCS model in engineering practice. *Rock Joints, Proc Int Symp on Rock Joints, Loen, Norway (Eds N. Barton and O. Stephenson)*, 603–610.

Belikov, B. P. (1967). Plastic constants of rock-forming minerals and their effect on the elasticity of rocks. *Physical and Mechanical Properties of Rocks. Academy of Sciences of the USSR, Israel Program for Scientific Translations, Jerusalem*, 124–140.

Bewick, R. P., Kaiser, P. K., & Amann, F. (2019). Strength of massive to moderately

jointed hard rock masses. *Journal of Rock Mechanics and Geotechnical Engineering*, *11*(3), 562–575. https://doi.org/10.1016/j.jrmge.2018.10.003.

Bewick, R. P., Valley, B., & Kaiser, P. K. (2012). Effect of grain scale geometric heterogeneity on tensile stress generation in rock loaded in compression. *46th US Rock Mechanics / Geomechanics Symposium*, *3*(January), 1787–1793.

Bieniawski, Z. T. (1973). ENGINEERING CLASSIFICATION OF JOINTED ROCK MASSES. *Civ Eng S Afr*.

Bieniawski, Z. T., & Bernede, M. J. (1979). Suggested methods for determining the uniaxial compressive strength and deformability of rock materials. Part 1. Suggested method for determination of the uniaxial compressive strength of rock materials. In *International Journal of Rock Mechanics and Mining Sciences and*. https://doi.org/10.1016/0148-9062(79)91450-5.

Brady, B. H. G. (1977). An analysis of rock behaviour in an experimental stoping block at the Mount Isa Mine, Queensland, Australia. *International Journal of Rock Mechanics and Mining Sciences*. https://doi.org/10.1016/0148-9062(77)90197-8.

Brady, B. H. G., & Brown, E. T. (2006). Rock Mechanics for underground mining: Third edition. In *Rock Mechanics for underground mining: Third edition*. https://doi.org/10.1007/978-1-4020-2116-9.

Broz, M. E., Cook, R. F., & Whitney, D. L. (2006). Microhardness, toughness, and modulus of Mohs scale minerals. *American Mineralogist*, *91*(1), 135–142.

Bunting, D. (1911). Chamber pillars in deep anthracite mines. *Trans AIME*, *42*, 236–245.

Cai, M. (2011). Rock mass characterization and rock property variability considerations for tunnel and cavern design. *Rock Mechanics and Rock Engineering*, *44*(4), 379–399. https://doi.org/10.1007/s00603-011-0138-5.

Dadashzadeh, N. (2020). *Reliability of Stress Induced Damage Predictions in Hard Rocks With Continuum and Discontinuum Numerical Modelling Approaches*.

Day, J. J., Diederichs, M. S., & Hutchinson, D. J. (2019). Composite Geological Strength Index Approach with Application to Hydrothermal Vein Networks and Other Intrablock Structures in Complex Rockmasses. *Geotechnical and Geological Engineering*, *37*(6), 5285–5314. https://doi.org/10.1007/s10706-019-00980-4.

Dershowitz, S. (1985). Rock Joint Systems. *Ph.D. Thesis, Massachusetts Institute of Technology, Cambridge, MA*.

Dershowitz, W. S., & Einstein, H. H. (1988). Characterizing rock joint geometry with joint system models. *Rock Mechanics and Rock Engineering*. https://doi.org/10.1007/BF01019674.

Di, S. J., Xu, W. Y., Ning, Y., Wang, W., & Wu, G. Y. (2011). Macro-mechanical properties of columnar jointed basaltic rock masses. *Journal of Central South University of Technology (English Edition)*. https://doi.org/10.1007/s11771-011-0955-4.

Diederichs, M. S. (2000). *Instability of hard rockmasses: The role of tensile damage and*

relaxation [University of Waterloo]. https://doi.org/10.16953/deusbed.74839.

Dolinar, D. R., & Esterhuizen, G. S. (2007). Evaluation of the effect of length on the strength of slender pillars in limestone mines using numerical modeling. *Proceedings of the 26th International Conference on Ground Control in Mining*, 304–313.

Elmo, D., & Stead, D. (2010). An integrated numerical modelling-discrete fracture network approach applied to the characterisation of rock mass strength of naturally fractured pillars. *Rock Mechanics and Rock Engineering*. https://doi.org/10.1007/s00603-009-0027-3.

Esterhuizen, G S, Dolinar, D. R., & Ellenberger, J. L. (2011). Pillar strength in underground stone mines in the United States. *International Journal of Rock Mechanics and Mining Sciences*, *48*(1), 42–50. https://doi.org/https://doi.org/10.1016/j.ijrmms.2010.06.003.

Esterhuizen, Gabriel S, Iannacchione, A. T., Ellenberger, J. L., & Dolinar, D. R. (2006). Pillar Stability Issues Based on a Survey of Pillar Performance in Underground Limestone Mines. *Proceedings of the 25th International Conference on Ground Control in Mining. Morgantown, WV: West Virginia University*, 354–361.

Gao, F., Stead, D., & Elmo, D. (2016). Numerical simulation of microstructure of brittle rock using a grain-breakable distinct element grain-based model. *Computers and Geotechnics*, *78*, 203–217. https://doi.org/10.1016/j.compgeo.2016.05.019.

Gerogiannopoulos, N. G. (1976). *A critical state approach to rock mechanics*. University of London.

Gerogiannopoulos, N. G., & Brown, E. T. (1978). The critical state concept applied to rock. *International Journal of Rock Mechanics and Mining Sciences*. https://doi.org/10.1016/0148-9062(78)90716-7.

Ghabaussi, J., Wilson, E. L., & Isenberg, J. (1973). FINITE ELEMENT FOR ROCK JOINTS AND INTERFACES. *ASCE J Soil Mech Found Div*.

Ghazvinian, E., Diederichs, M. S., & Quey, R. (2014). 3D random Voronoi grain-based models for simulation of brittle rock damage and fabric-guided micro-fracturing. *Journal of Rock Mechanics and Geotechnical Engineering*, *6*(6), 506–521. https://doi.org/10.1016/j.jrmge.2014.09.001.

Goodman, R. E., Taylor, R. L., & Brekke, T. L. (1968). A model for the mechanics of jointed rock. *Journal of Soil Mechanics & Foundations Div*.

Hajiabdolmajid, V., Martin, C. D., & Kaiser, P. K. (2000). Modelling brittle failure of rock. *4th North American Rock Mechanics Symposium, NARMS 2000*, *39*, 991–998.

Hedley, D. G. F., & Grant, F. (1972). Stope-and-pillar design for Elliot Lake Uranium Mines. *Canadian Mining and Metallurgical Bulletin*, *65*, 37–44.

Hoek, E. (1983). Strength of jointed rock masses. *Geotechnique*. https://doi.org/10.1680/geot.1983.33.3.187.

Hoek, E., & Brown, E. T. (1997). Practical estimates of rock mass strength. *International Journal of Rock Mechanics and Mining Sciences*, *34*(8), 1165–1186. https://doi.org/10.1016/S1365-1609(97)80069-X.

Hoek, E., & Brown, E. T. (2019). The Hoek–Brown failure criterion and GSI – 2018 edition. *Journal of Rock Mechanics and Geotechnical Engineering*, *11*(3), 445–463. https://doi.org/10.1016/j.jrmge.2018.08.001.

Hoek, E., Grabinsky, M. W., & Diederichs, M. S. (1991). Numerical modelling for underground excavation design. *Transactions - Institution of Mining & Metallurgy, Section A*, *100*(Jan-Apr).

Hoek, E., & Martin, C. D. (2014). Fracture initiation and propagation in intact rock - A review. *Journal of Rock Mechanics and Geotechnical Engineering*, *6*(4), 287–300. https://doi.org/10.1016/j.jrmge.2014.06.001.

Hoek, E. (1994). *Strength of rock and rock masse*.

Hoek, E, & Brown, E. T. (1980). *Hoek E, Brown ET. Underground excavations in rock. 1980.* London: Instn Min. Metall.

Hoek, E, Kaiser, P. K., & Bawden, W. F. (1995). Support of Underground Excavations in Hard Rock AA BALKEMA. *ROTTERDAM/BROOKFIELD*.

Hoek, Evert, Carranza, C., & Corkum, B. (2002). Hoek-brown failure criterion – 2002 edition. *Narms-Tac*, 267–273. https://doi.org/10.1016/0148-9062(74)91782-3.

Hudyma, M. R. (1988). *Development of empirical rib pillar design criterion for open stope mining*. Doctoral dissertation, University of British Columbia.

Hustrulid, W. A. (1976). A review of coal pillar strength formulas. *Rock Mechanics*, *8*(2), 115–145.

Itasca Consulting Group, I. (2008). *PFC — Particle Flow Code, Ver. 4.0*.

Jing, L., & Hudson, J. A. (2002). Numerical methods in rock mechanics. *International Journal of Rock Mechanics and Mining Sciences*, *39*(4), 409–427. https://doi.org/10.1016/S1365-1609(02)00065-5.

Kaiser, P. K., Kim, B., Bewick, R. P., & Valley, B. (2011). Rock mass strength at depth and implications for pillar design. *Transactions of the Institutions of Mining and Metallurgy, Section A: Mining Technology*, *120*(3), 170–179. https://doi.org/10.1179/037178411X12942393517336.

Kaiser, P. K., Maloney, S. M., & Yong, S. (2016). Role of large scale heterogeneities on in-situ stress and induced stress fields. *50th US Rock Mechanics / Geomechanics Symposium 2016*.

Kaiser, P. K., & Tang, C. A. (1998). Numerical simulation of damage accumulation and seismic energy release during brittle rock failure - Part II: Rib pillar collapse. *International Journal of Rock Mechanics and Mining Sciences*, *35*(2), 123–134. https://doi.org/10.1016/S0148-9062(97)00010-7.

Kazerani, T., & Zhao, J. (2010). Micromechanical parameters in bonded particle method for modelling of brittle material failure. *International Journal for Numerical and Analytical Methods in Geomechanics*, *34*(18), 1877–1895. https://doi.org/10.1002/nag.884.

Krauland, N., & Soder, P. E. (1987). Determining pillar strength-from pillar failure

observation. *Engineering and Mining Journal*, *188(8)*, 34–40.

Lan, H., Martin, C. D., & Andersson, J. C. (2013). Evolution of in situ rock mass damage induced by mechanical-thermal loading. *Rock Mechanics and Rock Engineering*, *46*(1), 153–168. https://doi.org/10.1007/s00603-012-0248-8.

Lan, H., Martin, C. D., & Hu, B. (2010). Effect of heterogeneity of brittle rock on micromechanical extensile behavior during compression loading. *Journal of Geophysical Research*, *115*(B1). https://doi.org/10.1029/2009jb006496.

Laubscher, D. H., & Jakubec, J. (2001). The MRMR rock mass classification for jointed rock masses. *Underground Mining Methods: Engineering Fundamentals and International Case Studies, WA Hustrulid and RL Bullock (Eds) Society of Mining Metallurgy and Exploration, SMME*, 475–481.

Li, K., Cheng, Y., & Fan, X. (2018). Roles of model size and particle size distribution on macro-mechanical properties of Lac du Bonnet granite using flat-joint model. *Computers and Geotechnics*, *103*, 43–60. https://doi.org/https://doi.org/10.1016/j.compgeo.2018.07.007.

Li, X., Kim, E., & Walton, G. (2019). A study of rock pillar behaviors in laboratory and in-situ scales using combined finite-discrete element method models. *International Journal of Rock Mechanics and Mining Sciences*, *118*(November 2018), 21–32. https://doi.org/10.1016/j.ijrmms.2019.03.030.

Li, Y., & Bahrani, N. (2020). A numerical study on the failure process and strength of heterogeneous rocks and highly interlocked jointed pillars. *54th US Rock Mechanics/Geomechanics Symposium*.

Li, Y., & Bahrani, N. (2021). A continuum grain-based model for intact and granulated Wombeyan marble. *Computers and Geotechnics*, *129*, 103872. https://doi.org/10.1016/j.compgeo.2020.103872.

Lim, S. S., Martin, C. D., & Åkesson, U. (2012). In-situ stress and microcracking in granite cores with depth. *Engineering Geology*. https://doi.org/10.1016/j.enggeo.2012.07.006.

Lisjak, A., & Grasselli, G. (2014). A review of discrete modeling techniques for fracturing processes in discontinuous rock masses. *Journal of Rock Mechanics and Geotechnical Engineering*, *6*(4), 301–314. https://doi.org/10.1016/j.jrmge.2013.12.007.

Liu, G., Cai, M., & Huang, M. (2018). Mechanical properties of brittle rock governed by micro-geometric heterogeneity. *Computers and Geotechnics*, *104*(September 2017), 358–372. https://doi.org/10.1016/j.compgeo.2017.11.013.

Lunder, P. J., & Pakalnis, R. C. (1997). Determination of the strength of hard-rock mine pillars. *CIM Bulletin*, *90*(1013), 51–55.

Martin, C. D., & Chandler, N. A. (1994). The progressive fracture of Lac du Bonnet granite. *International Journal of Rock Mechanics and Mining Sciences And*. https://doi.org/10.1016/0148-9062(94)90005-1.

Martin, C. D., Kaiser, P. K., & McCreath, D. R. (1999). Hoek-Brown parameters for predicting the depth of brittle failure around tunnels. *Canadian Geotechnical Journal*, *36*(1), 136–151. https://doi.org/10.1139/t98-072.

Martin, C. D., & Maybee, W. G. (2000). *The strength of hard-rock pillars*. *37*, 1239–1246.

Mas Ivars, D., Pierce, M. E., Darcel, C., Reyes-Montes, J., Potyondy, D. O., Paul Young, R., & Cundall, P. A. (2011). The synthetic rock mass approach for jointed rock mass modelling. *International Journal of Rock Mechanics and Mining Sciences*. https://doi.org/10.1016/j.ijrmms.2010.11.014.

Maybee, W. G. (2000). Pillar Design in Hard Brittle Rocks. *Science*.

Mortazavi, A., Hassani, F. P., & Shabani, M. (2009). A numerical investigation of rock pillar failure mechanism in underground openings. *Computers and Geotechnics*, *36*(5), 691–697. https://doi.org/10.1016/j.compgeo.2008.11.004.

Pariseau, W. G. (1982). SHEAR STABILITY OF MINE PILLARS IN DIPPING SEAMS. *Proceedings - Symposium on Rock Mechanics*.

Paterson, M. S. (1958). Experimental deformation and faulting in wombeyan marble. *Bulletin of the Geological Society of America*. https://doi.org/10.1130/0016-7606(1958)69[465:EDAFIW]2.0.CO;2.

Peng, J., Rong, G., Cai, M., & Zhou, C. B. (2015). A model for characterizing crack closure effect of rocks. *Engineering Geology*, *189*, 48–57. https://doi.org/10.1016/j.enggeo.2015.02.004.

Potvin, Y., Hudyma, M., & Miller, H. D. S. (1990). Rib pillar design in open stope mining. *International Journal of Rock Mechanics and Mining Sciences & Geomechanics Abstracts*, *27*(1), 57. https://doi.org/10.1016/0148-9062(90)90467-g.

Potyondy, D. O. (2010). A grain-based model for rock: Approaching the true microstructure. *Bergmekanikk i Norden 2010 - Rock Mechanics in the Nordic Countries*.

Potyondy, D. O., & Cundall, P. A. (2004). A bonded-particle model for rock. *International Journal of Rock Mechanics and Mining Sciences*. https://doi.org/10.1016/j.ijrmms.2004.09.011.

Pritchard, C., & Hedley, D. (1993). Progressive pillar failure and rockbursting at Denison Mine. *Proceedings of 3rd International Symposium on Rockbursts and Seismicity in Mines, Kingston. Rotterdam: AA Balkema*, 111J6.

Rafiei Renani, H., & Martin, C. D. (2018). Modeling the progressive failure of hard rock pillars. *Tunnelling and Underground Space Technology*, *74*(January), 71–81. https://doi.org/10.1016/j.tust.2018.01.006.

Riahi, A., Hammah, E. R., & Curran, J. H. (2010). Limits of applicability of the finite element explicit joint model in the analysis of jointed rock problems. *44th US Rock Mechanics Symposium - 5th US/Canada Rock Mechanics Symposium*.

Roberts, D., Tolfree, D., & McIntire, H. (2007). Using confinement as a means to estimate pillar strength in a room and pillar mine. *Proceedings of the 1st Canada-US Rock Mechanics Symposium - Rock Mechanics Meeting Society's Challenges and Demands*. https://doi.org/10.1201/noe0415444019-c180.

Rocscience. (2019). *RS2 v. 10.08*.

Rosengren, K. J., & Jaeger, J. C. (1968). The mechanical properties of an interlocked low-porosity aggregate. *Geotechnique*, *18*(3), 317–326. https://doi.org/10.1680/geot.1968.18.3.317.

Salamon, M. D. G., & Munro, A. H. (1967). A study of the strength of coal pillars. *J S Afr Inst Min Metall*, *68(2)*, 55–67.

Shin, S. W. (2010). *Excavation Disturbed Zone in Lac Du Bonnet Granite*. UMI Dissertation Services. https://books.google.ca/books?id=4aoGjwEACAAJ.

Sinha, S., & Walton, G. (2018). A progressive S-shaped yield criterion and its application to rock pillar behavior. *International Journal of Rock Mechanics and Mining Sciences*, *105*(August 2017), 98–109. https://doi.org/10.1016/j.ijrmms.2018.03.014.

Sinha, S., & Walton, G. (2020). A study on Bonded Block Model (BBM) complexity for simulation of laboratory-scale stress-strain behavior in granitic rocks. *Computers and Geotechnics*, *118*(November 2019). https://doi.org/10.1016/j.compgeo.2019.103363.

Sjöberg, J. (1992). Failure modes and pillar behaviour in the Zinkgruvan mine. *33rd U.S. Symposium on Rock Mechanics, USRMS 1992*, 491–500. https://doi.org/10.1016/0148-9062(93)93204-b.

Sjöberg, J., & Tillman, K. (1990). Stability of pillars in the Zinkgruvan Mine - A case study. *31st U.S. Symposium on Rock Mechanics, USRMS 1990*. https://doi.org/10.1016/0148-9062(92)91534-c.

Stavrou, A., Vazaios, I., Murphy, W., & Vlachopoulos, N. (2019). Refined Approaches for Estimating the Strength of Rock Blocks. *Geotechnical and Geological Engineering*, *37*(6), 5409–5439. https://doi.org/10.1007/s10706-019-00989-9.

Szwilski, A. . (1982). Sizing of chain pillars around longwall panels. *Proc. 1st Int. Conf. on Stability in Underground Mining, Brawner (Ed.), Soc. Min. Engrs, AIME, New York*, 535–558.

Tatone, B. S. A., & Grasselli, G. (2015). A calibration procedure for two-dimensional laboratory-scale hybrid finite-discrete element simulations. *International Journal of Rock Mechanics and Mining Sciences*, *75*, 56–72. https://doi.org/10.1016/j.ijrmms.2015.01.011.

Tian, W. L., Yang, S. Q., Huang, Y. H., & Hu, B. (2020). Mechanical Behavior of Granite with Different Grain Sizes After High-Temperature Treatment by Particle Flow Simulation. *Rock Mechanics and Rock Engineering*. https://doi.org/10.1007/s00603-019-02005-1.

Valley, B., Suorineni, F. T., & Kaiser, P. K. (2010). Numerical analyses of the effect of heterogeneities on rock failure process. *44th US Rock Mechanics Symposium - 5th US/Canada Rock Mechanics Symposium*, *January 2014*. https://doi.org/10.13140/2.1.1622.7522.

Valley, B., Kim, B. H., Suorineni, F. T., Bahrani, N., Bewick, R. P., & Kaiser, P. K. (2011). Influence of confinement dependent failure processes on rock mass strength at depth. *Harmonising Rock Engineering and the Environment - Proceedings of the 12th ISRM International Congress on Rock Mechanics*, *September*, 855–860.

https://doi.org/10.1201/b11646-157.

Von Kimmelmann, M. R., Hyde, B., & Madgwick, R. J. (1984). *Use of Computer Applications At Bcl Limited in Planning Pillar Extraction and the Design of Mining Layouts.* 53–63.

Wang, X., & Cai, M. (2018). Modeling of brittle rock failure considering inter- and intra-grain contact failures. *Computers and Geotechnics*, *101*(November 2017), 224–244. https://doi.org/10.1016/j.compgeo.2018.04.016.

APPENDIX A - PILLAR STABILITY DATABASE

Table A-1: Pillar stability database collected from the Selbi - Phikwe mines of BCL Ltd. in South Africa presented by Von Kimmelmann et al. (1984). Long pillar case histories shaded in grey.

Condition	W/H	UCS (MPa)	Average pillar stress (MPa)	σ_p/UCS
	1	94	25	0.27
	1.5	94	29	0.31
	1.25	94	40	0.43
	0.9	94	28	0.30
	1	94	45	0.48
	1.48	94	48	0.51
	1.3	94	50	0.53
Stable	1.2	94	47	0.50
	0.86	94	26	0.28
	0.86	94	30	0.32
	1.25	94	35	0.37
	1.00	94	35	0.37
	0.80	94	35	0.37
	0.70	94	37	0.39
	1.30	94	60	0.64
	0.43	94	35	0.37
	0.40	94	50	0.53
	0.39	94	28	0.30
	0.50	94	34	0.36
	0.62	94	34	0.36
	0.64	94	35	0.37
Unstable	0.87	94	40	0.43
	0.75	94	47	0.50
	0.83	94	48	0.51
	0.70	94	48	0.51
	0.89	94	53	0.56
	0.39	94	54	0.57
	0.46	94	55	0.59
	0.61	94	56	0.60
	0.45	94	48	0.51
	0.30	94	48	0.51
	0.30	94	48	0.51
	0.30	94	48	0.51
	0.38	94	50	0.53
	0.63	94	53	0.56
	0.70	94	55	0.59
	0.50	94	55	0.59
Failed	0.47	94	55	0.59
	0.61	94	55	0.59
	0.80	94	58	0.62
	0.75	94	58	0.62
	0.50	94	58	0.62
	0.25	94	58	0.62
	0.50	94	59	0.63
	1.00	94	59	0.63
	0.50	94	59	0.63
	0.50	94	59	0.63

	0.50	94	59	0.63
	1.13	94	60	0.64
	0.30	94	60	0.64
	0.61	94	63	0.67
	0.61	94	54	0.57
	0.46	94	55	0.59
	0.66	94	55	0.59
	0.64	94	56	0.60
	0.70	94	63	0.67
	0.75	94	63	0.67

Table A-2: Pillar stability database collected from the uranium mines in the Elliot Lake district of Ontario, Canada presented by Hedley and Grant (1972).

Condition	W	H	W/H	Average pillar stress (psi)	UCS (psi)	σ_p/UCS
	10	10	1.00	5000	30458	0.16
	10	10	1.00	6400	30458	0.21
	20	18	1.11	3800	30458	0.12
	10	10	1.00	7600	30458	0.25
	10	10	1.00	7500	30458	0.25
	20	18	1.11	4000	30458	0.13
	10	10	1.00	8500	30458	0.28
	10	10	1.00	9400	30458	0.31
	20	20	1.00	4600	30458	0.15
	20	18	1.11	4800	30458	0.16
	18	18	1.00	5400	30458	0.18
Stable	20	14	1.43	7600	30458	0.25
	40	20	2.00	5800	30458	0.19
	22	20	1.10	5000	30458	0.16
	20	14	1.43	7600	30458	0.25
	20	14	1.43	8000	30458	0.26
	19	18	1.06	6400	30458	0.21
	20	20	1.00	7203	30458	0.24
	20	8	2.50	7600	30458	0.25
	20	8	2.50	7900	30458	0.26
	20	8	2.50	8600	30458	0.28
	15	9	1.67	10500	30458	0.34
	20	9	2.22	12600	30458	0.41
Unstable	10	10	1.00	11400	30458	0.37
	10	9	1.11	13400	30458	0.44
	10	9	1.11	15200	30458	0.50
Failed	10	9	1.11	15700	30458	0.52
	15	10	1.50	18500	30458	0.61

Table A-3: Sill pillar stability database collected from Zinkgruvan mine in Canada presented by Sjöberg (1992).

Condition	W/H	UCS (MPa)	Average pillar stress (MPa)	σ_p/UCS
Unstable	0.63	240	68	0.28
	1	240	84	0.35
	1.03	240	74	0.31
	1.22	240	67	0.28
Failed	0.78	240	95	0.40
	1.25	240	83	0.35
	1.25	240	100	0.42
	1.42	240	82	0.34
	1.75	240	92	0.38

Table A-4: Squat pillar stability database collected from Black Angle mine in Greenland presented by Krauland and Soder (1987).

Condition	W/H	UCS	Average pillar stress (MPa)	σ_p/UCS
Unstable	0.88	100	39.3	0.39
	0.88	100	47.5	0.48
	0.83	100	31	0.31
	0.74	100	29	0.29
	0.74	100	31	0.31
	0.66	100	47.5	0.48
	0.62	100	31	0.31
	0.59	100	29	0.29
	0.55	100	29	0.29
	0.53	100	31	0.31
	0.51	100	37	0.37
	0.47	100	41.4	0.41
	0.45	100	25	0.25

Table A-5: Rib pillar stability database collected from Mount Isa mines in Australia presented by Brady (1977).

Condition	W/H	UCS	Average pillar stress (MPa)	σ_p/UCS
Stable	2.33	170	39.3	0.23
	2.33	170	55.6	0.33
Failed	1	170	88.7	0.52

Table A-6: Rib pillar stability database collected from open stope mines in Canadian Shield presented by Potvin et al. (1990).

Condition	W	H	W/H	UCS (MPa)	Average pillar stress (MPa)	σ_p/UCS
Stable	24	52	0.46	265	38	0.14
	21	39	0.54	176	26	0.15
	27	40	0.68	176	28	0.16
	30	44	0.68	265	40	0.15
	30	40	0.75	176	33	0.19
	30	40	0.75	176	29	0.16
	45	53	0.85	200	51	0.26
	21	24	0.88	176	29	0.16
	21	21	1.00	100	31	0.31
	21	21	1.00	100	26	0.26
	32	28	1.14	90	30	0.33
	15	12	1.25	176	37	0.21
	15	12	1.25	176	33	0.19
	24	18	1.33	72	36	0.50
	33	23	1.43	316	75	0.24
	12	8	1.50	215	28	0.13
	33	20	1.65	121	55	0.45
	17	10	1.70	310	46	0.15
	15	7	2.14	215	29	0.13
	24	11	2.18	148	66	0.45
	33	15	2.20	316	76	0.24
	20	8	2.50	310	46	0.15
	17	6	2.83	72	31	0.43
	35	12	2.92	148	63	0.43
	21	5	4.20	72	39	0.54
	18	4	4.50	72	48	0.67
Unstable	24	52	0.46	265	72	0.27
	15	27	0.56	176	28	0.16
	27	46	0.59	265	59	0.22
	24	38	0.63	160	70	0.44
	30	44	0.68	265	82	0.31
	15	18	0.83	100	31	0.31
	25	28	0.89	90	32	0.36
	25	27	0.93	70	29	0.41
	15	15	1.00	176	43	0.24
Failed	15	49	0.31	200	64	0.32
	9	20	0.45	100	38	0.38
	11	23	0.48	316	99	0.31
	15	30	0.50	100	38	0.38
	14	28	0.50	90	49	0.54
	11	20	0.55	121	69	0.57
	15	27	0.56	176	31	0.18
	11	18	0.61	316	102	0.32
	27	40	0.68	176	38	0.22
	19	28	0.68	90	41	0.46
	30	40	0.75	176	57	0.32
	15	18	0.83	100	40	0.40

Table A-7: Pillar stability database collected from H-W mine in Canada presented by Lunder and Pakalnis (1997). Rib pillar case histories shaded in grey.

Condition	W/H	UCS (MPa)	Average pillar stress (MPa)	σ_p/UCS
Stable	1.48	172	49.6	0.29
	1.8	172	56.7	0.33
Unstable	1.95	172	99.9	0.58
	1.2	172	77.9	0.45
	1.15	172	70.8	0.41
	0.88	172	70.8	0.41
	1.74	172	85	0.49
	1.9	172	91.8	0.53
	1.28	172	63.8	0.37
	3.03	172	91.8	0.53
	1.48	172	63.8	0.37
	3	172	42.5	0.25
	1.95	172	77.9	0.45
Failed	1.02	172	93.5	0.54
	1.02	172	93.5	0.54
	1.4	172	93.5	0.54
	1.58	172	93.5	0.54
	1.08	172	93.5	0.54
	0.94	172	93.5	0.54
	0.87	172	93.5	0.54
	1.29	172	93.5	0.54
	1	172	93.5	0.54
	1.48	172	105.4	0.61
	1.38	172	93.5	0.54
	1.43	172	105.4	0.61
	1.3	172	98.6	0.57
	1.33	172	91.8	0.53
	0.96	172	88.4	0.51
	1.78	172	98.6	0.57
	1.08	172	93.5	0.54
	0.62	172	93.5	0.54